Université de Strasbourg

# UNIVERSITÉ DE STRASBOURG

msii ÉCOLE DOCTORALE


***ÉCOLE DOCTORALE nº 269*** **: Mathématiques, Sciences de l'Information et de l'Ingénieur (MSII)**

**Laboratoire des Sciences de l'Ingénieur, de de l'Information et de l'Imagerie (ICUBE UMR 7357)**


**THÈSE** présentée par :


**Husneni MUKHTAR**


soutenue le : 29 Juin 2018

pour obtenir le grade de : **Docteur de l'université de Strasbourg**

Discipline / Spécialité : Electronique, microélectronique, photonique

# Development of compensated immersion 3D optical profiler based on interferometry

THÈSE dirigée par :

**Dr. MONTGOMERY Paul** Directeur de recherche, CNRS, ICube (Strasbourg)

RAPPORTEURS :

**Dr. GORECKI Christophe** Directeur de recherche, CNRS, FEMTO-ST (Besançon)

**Pr. SERIO Bruno** Professeur des Universités, Université Paris Ouest, LEME (Paris)

---

AUTRES MEMBRES DU JURY :

**Pr. BARILLON Rémi** Professeur des Universités, Université de Strasbourg, IPHC (Strasbourg)

# Acknowledgements

Undertaking this PhD has been a truly life-changing experience for me and it would not have been possible to do without the support and guidance that I received from many people and the institutions.

First of all, I gratefully acknowledge my PhD supervisor, Paul Montgomery, senior CNRS researcher. Thank you for his professional guidance, advice, enormous encouragement, and continuous support of my research progress in this tough subject. Then I would like to thank Freddy Anstotz, my co-encadrant for his patient guidance, the discussion time and help in the instrumentation aspects. I have been extremely lucky to have them who cared so much about my work and responded to my questions and queries so well.

I would like to extend my gratitude to the permanent staff in the IPP group: Pierre Pfeiffer for helping me do some measurements with other microscopes, as well as Patrice Twardowski, Joël Fontaine and Sylvain Lecler.

I also would like to thank the IPHC team: Rémi Barillon for his support, Catherine Galindo for providing the colloid samples and discussions and Christophe Hoffman for helping me to improve the software performance of the motor controller. Thanks are also extended to Anne Rubin (ICS) for the idea of using PDMS.

Then I want to show my appreciation for the help from the engineers and technicians of ICube and the C3-Fab platform: Sébastien Shmitt for discussing the mechanical parts, Florent Dietrich for making the polymer molds and other mechanical parts used in the modification phase, Stephan Roques for making the Al step Si sample and guiding me in making the PDMS slabs, Nicolas Zimmerman for helping me in the chemical experiments and Nicolas Collin.

I extend my thanks to all the PhDs and post-docs in our research group, especially for Stephane Perrin, Audrey Leong-Hoi, Rémy Claveau, Gianto Gianto, and Eric Halter for your kind helps and great discussion. It has really been an enjoyable and unforgettable working and learning experience with all of them.

I would like to thank the LPDP (Indonesia Endowment Fund for Education), not only for providing the funding which allowed me to undertake this PhD, but also for giving me the opportunity to attend conference. Thanks are extended to Telkom university for permit and support me to continue my education in PhD.

I express my gratitude for my late father who always encourage and motivate me in the education and life. Thanks also all families and friends for their pray and moral support, particularly for my sister Sheizi Prista Sari for all her spirit and beliefs.

Finally, I thank Kusnahadi Susanto for his great daily support and make things easier in any perspective.

# TABLE OF CONTENTS

Acknowledgements ........ 1

TABLE OF CONTENTS ........ ii

TABLE OF TABLES ........ v

TABLE OF FIGURES ........ vii

TABLE OF ANNEXES ........ xvi

TABLE OF ABBREVIATIONS AND ACRONYMS ........ xvii

RÉSUMÉ ........ xviii

INTRODUCTION ........ 1

CHAPTER 1 ........ 4

3D SURFACE PROFILING ........ 4

1.1 Existing measurement systems ........ 5

1.1.1 Contact profilometers ........ 6

1.1.2 Optical profilers ........ 14

1.1.3 Comparison of characteristic parameters of profilers ........ 20

1.2 Interference microscopy ........ 22

1.2.1 Phase Shifting Microscopy ........ 24

1.2.2 CSI method ........ 26

1.2.2.1 General principle of CSI ........ 27

1.2.2.2 Signal processing in CSI ........ 27

1.3 Resolution ........ 29

1.3.1 Lateral Resolution ........ 29

1.3.2 Axial Resolution ........ 32

1.4 Conclusion ........ 33

1.4 Résumé de chapitre 1 ........ 35

CHAPTER 2 ........ 38

OPTIMIZATION OF A LINNIK MICROSCOPE ........ 38

2.1 Linnik Setup ........ 39

2.2 Linnik designs ........ 40

2.3 Compact system vs breadboard ........ 45

2.4 Conclusion ........ 46

2.5 Résumé du chapitre 2 ........ 46

CHAPTER 3 ........ 49

WATER IMMERSION LINNIK HEAD AND COMPENSATION ........................................ 49
3.1 Introduction ........................................................................................ 50
3.2 Initial Fogale microscope ........................................................................ 52
3.2.1 Instrumentation description ..................................................................... 52
3.2.2 Description of control and analysis software ............................................. 54
3.2.3 Discussion .............................................................................................. 55
3.3 Modification of Fogale microscope ............................................................ 55
3.3.1 Initial Fogale to Mirau setup .................................................................... 55
3.3.1.1 Instrumentation modification ................................................................. 56
3.3.1.2 Description of "FringeSurf 3D 3.1" control and analysis software and of "MountainsMap" surface roughness analysis software ................................................................. 56
3.3.1.3 First measurements using the Mirau Fogale .............................................. 57
3.3.2 Mirau to Linnik in air ............................................................................... 60
3.3.2.1 Instrumentation modification ................................................................. 60
3.3.2.2 Problems to solve to achieve the first measurements ................................. 61
Problem of OPD to find fringes ..................................................................... 62
Difficulties associated with the white LED light source ..................................... 62
3.3.2.3 Description of Linnik head and the new integrated control software ............ 69
3.3.3 Immersion linnik head and water compensation ........................................... 70
3.3.3.1 Instrumentation modification ................................................................. 70
3.3.3.2 Compensation in mirror arm .................................................................. 70
3.3.3.3 First measurement with immersion Linnik setup ....................................... 74
3.3.3.3.1 Measurements with no reference arm compensation ............................... 75
3.3.3.3.2 Measurements with reference arm compensation ................................... 81
3.3.4 Linnik using motor in mirror arm ............................................................... 84
3.3.4.1 Introduction ......................................................................................... 85
3.3.4.2 Description of motor control software ...................................................... 85
3.3.4.3 Measurement tests of the motorised stage ............................................... 87
3.4 Comparison of measurements using water-immersion Linnik Fogale and other microscopes ........................................................................................ 87
3.5 Discussion of measurement results ............................................................ 94
3.5.1 Hardware misalignment ............................................................................ 94
3.5.2 Resolution limit and loss in resolution ....................................................... 103
3.6 Conclusion .......................................................................................... 104
3.7 Résumé du chapitre 3 ............................................................................. 105
CHAPTER 4 ............................................................................................... 107
SURPASSING THE DIFFRACTION LIMIT USING MICROSPHERE ASSISTED 3D IMMERSION MICROSCOPY ............................................................................ 107
4.1 Introduction ........................................................................................ 108
4.2 Microsphere: definition, utility ................................................................. 110

**4.3 Measurements using microspheres** ........................................................ **110**
**4.5 Discussion** ........................................................................................ **119**
**4.6 Conclusion** ....................................................................................... **120**
**4.6 Résumé du chapitre 4** .......................................................................... **120**

**CONCLUSION AND PERSPECTIVES** ........................................................... **122**

**BIBLIOGRAPHY** ........................................................................................ **124**
**LIST OF PUBLICATIONS AND COMMUNICATIONS** ........................................ **133**

**ANNEXES** ................................................................................................. **136**

# TABLE OF TABLES

Table 1. The classification of methods for measuring surface texture based on ISO 25178-6 2010 [8]. ........ 5

Table 2. Comparison the main characteristic parameters of stylus profiler, SPM, confocal microscope and white light interferometer [9]. ........ 21

Table 3. Classification of 3D optical sensors [8]. ........ 22

Table 4. Comparison of using different techniques in interferometer. ........ 24

Table 5. The lateral resolution criteria based on the illumination type. ........ 31

Table 6. Comparison of compact system and breadboard ........ 45

Table 7. Comparison of white light LED and conventional halogen source. ........ 64

Table 8. Specification of the comparative microscopes ........ 87

Table 9. Comparison of measurements of etched silicon area-1 using each microscope ........ 89

Table 10. Comparison of measurements of etched silicon area-2 and area-3 using each microscope ........ 90

Table 11. Comparison of measurements of etched silicon (oval pattern) using each microscope. ........ 91

Table 12. Comparison of measurements of etched silicon (oval pattern) using each microscope. ........ 93

Table 13. Comparison of measurements of etched silicon (oval pattern) using each microscope. ........ 93

Table 14. Mean of the lateral shift between successive images for each case and objective magnification. ........ 99

Table 15. Character of red LED with variance of LED voltage and exposure times in effect for the effective wavelength. ........ 68

Table 16. Character of white light LED with variance of LED voltage and exposure times in effect for the effective wavelength. ........ 68

Table 17. Comparison of measurement results of etched-silicon, hole area-2 using Zygo, Fogale, AFM and microspheres. ........ 112

Table 18. Comparison measurement result of etched-silicon the hole area-3 using Zygo, Fogale, AFM and microspheres. ........ 113

Table 19. Comparison of measurement results of etched silicon sample using the Zygo, Fogale, AFM and microsphere. ........ 115

Table 20. Comparison of measurement result of grating sample using Zygo, Fogale, AFM and microsphere. ........ 116

Table 21. Measurement results of standard grating SiMETRICS using BTGMS in range 30-45 µm. ........ 119

Table 22. Measurement results of standard grating SiMETRICS using BTGMS microsphere in range 75-90 µm. ........ 119

# TABLE OF FIGURES

Figure 1. Schematic of stylus profiler with LVDT as the motion detector. Part a is a fixed stylus with LVDT assembly and b is a sample. ........................................... 6

Figure 2. Illustration of stylus profiler scanning over the surface of trenches with various aspect ratios. The convolution of a 25 μm radius stylus tip with a surface profile [9]. ....................................................................................................... 7

Figure 3. (a) The schematic view of STM; Two typical modes of STM: (b) constant-current mode, and (c) constant-height mode [19]. ............................................... 9

Figure 4. The force F in the contact mode and the force gradient F’ in the con-contact mode is measured during scanning. The deflection sensor detects the deflection of the cantilever [21]. ......................................................................................... 10

Figure 5. Schematic of signal detection in AFM Tapping Mode. The probe is kept at a constant level above the sample, which results in a constant amplitude signal. Changes in the amplitude of the signal indicate that the distance between cantilever and object has changed [9]. ........................................................................ 11

Figure 6. Schematic of variations of detection systems [21]. ..................................... 11

Figure 7. An experimental scheme of a scanning force microscopy liquid cell of RNA polymerase [36]. A volume of 30 µl distilled water and some variations of other buffer types filled the chamber via the hosting and syringe. It took several minutes to 2 hours to reach the mechanical and thermal stability before performing imaging. ................................................................................................................ 12

Figure 8. Illustration of high speed atomic force microscopy head integrated with OBD system [29]. ........................................................................................................ 13

Figure 9. Illustration of two designs of immersion AFM in open (a) and closed (b) liquid cells [41]........................................................................................................ 14

Figure 10. Simplified schematic of a confocal scanning optical microscope showing the sample (a) in the focal plane of the objective and (b) out of focus. (c) The schematic of chromatic confocal microscopy [1][9]. .......................................... 16

Figure 11. White light interferograms for a spherical object as obtained for a few positions of the objective during an axial scan [9]. .............................................. 17

Figure 12. The objective setups of (a) Michelson and (b) Mirau: MO (microscope objective), RM (reference mirror), BS (beam splitter). ....................................... 17

Figure 13. (a) IMI system (b) Layout of SIMI system with two-camera arrangement. . 18

Figure 14. Principle of digital holographic microscopy [50]. ...................................... 20

Figure 15. Superposition illustrations. (a) constructive interference, (b) destructive interference, (c) constructive interference from a coherent light source ................ 23

Figure 16. Phase determination, from 4 discrete steps of 120° [58]. ............................ 25

Figure 17.The technique of the change of phase [58]................................................. 26

Figure 18. An interferogram on a surface using CSI.................................................. 27

Figure 19. Z-scan technique........................................................................... 28

Figure 20. A circular aperture of Airy pattern in central Airy disk.............................. 32

Figure 21. Illustration of a full width at height maximum and the relation with the standard deviation, σ. ............................................................................ 33

Figure 22. Linnik configuration in air. ........................................................ 39

Figure 23. Configuration of a Linnik water-immersion objective. ............................... 40

Figure 24. Experimental setup of a Linnik for FF-OCT imaging in living tissue [84]. . 41

Figure 25. Schematic of (a) the ultrahigh-resolution full-field OCT setup [7] and (b) the experimental setup of FF-OCM [86]. MO, microscope objective; BS, beam-splitter cube; DM, dichroic mirror; PZT, piezoelectric actuator. ..................................... 42

Figure 26. General scheme of a high precision Linnik interferometer. working distance (WD), the axial objective lens distance (OLD) [85]. ........................................... 43

Figure 27. Schematic of Linnik setup. ND, neutral density filter; GP, glass plate; DAQ, data acquisition board in computer [89]. ............................................................ 44

Figure 28. The system of Leitz-Linnik microscope developed at ICube [92]. ............. 45

Figure 29. Illustration of combining CSI technique and ATR-FTIR. ........................... 51

Figure 30. Details of the initial Fogale Nanotech microscope in 2014 showing (a) the microscope mounted on old optical benches on the vibration isolated table and (b) the previous Linnik immersion head [94] with (1) LED light source, (2) beam splitter, (3) reference mirror assembly consisting of an adapted Mirau mechanism, (4) orientation adjustment and (5) the immersion objectives................................ 52

Figure 31. Details of the previous immersion head for the *in situ* characterization of the growth of HA layers in SBF solution, showing (a) the schematic layout, (b) the immersion head immersed in SBF solution and (c)the inside of the Teflon bath with the immersion objective, the water and the observation window [94].................. 53

Figure 32. Interface software "FringeSurf 3D 2.1" for measuring the surface roughness (2013)............................................................................................... 54

Figure 33. The first step of the modifications from (a) the initial Fogale Linnik microcope design on the old steel optical bench column (1) to (b) the Mirau

objective setup on the new aluminium optical bench column (1) and the head (2). The tip/tilt mechanism is indicated at (3). ........ 56

Figure 34. The control and analysis software “FringeSurf 3D 3.1” for measuring surface roughness with the Mirau Fogale microscope (2014). ........ 57

Figure 35. The first fringes were found for testing the Mirau Fogale using the red LED. The contrast and spacing are changed by using the adjustment screws in the Mirau mechanism........ 58

Figure 36. The altitude and 3D images of DOE using the ×10 Mirau Fogale head with the red LED, $\lambda_{eff}$ = 640 nm, dynamic range 15 μm, and step height 0.078 μm [4415]........ 58

Figure 37. Line profile of the measured area of DoE using the ×10 Mirau Fogale head with the red LED, $\lambda_{eff}$ = 640 nm, dynamic range 15 μm, and step height 0.078 μm [4415]........ 59

Figure 38. The altitude and 3D images of C-S-H colloid using the ×10 Mirau objective and the Fogale head with the red LED [4433]. ........ 59

Figure 39. Line profile of the measured area of C-S-H colloid on the line using ×10 Mirau Fogale head with the red LED [4433]. ........ 59

Figure 40. Illustration of the modification of the Linnik head. The tip/tilt and centering mechanism (1) is moved from the object to the reference arm and the beam stopper (2) and 8 mm-thick ring (3) are moved from the reference arm to the object arm. An adaptor tube (4) is used to mount the Mirau mirror mechanism on the reference arm. An adapted back plate (5) and an adapted cube holder (6) are installed on the rear side of the Linnik head mounted on the microscope. ........ 60

Figure 41. The objective tip/tilt and centering mechanism. The screws marked by red circles are used to change the angle of the objective in order to change the fringe orientation separation........ 61

Figure 42. Adjustment control in reference arm. ........ 61

Figure 43. First fringes found by ×20 (immersion objectives) Linnik Fogale in air with red LED (left) and white LED (right) illumination. ........ 62

Figure 44. The asymmetrical envelope of an interferogram using the original white LED LXHL-MW1D. ........ 63

Figure 45. The measured spectrum of the original phosphor-based white LED LXHL-MW1D of the initial Fogale microscope. ........ 63

Figure 46. The measured spectrum of the new white LED (LUXEON Rebel lime color) chosen for its more balanced spectral range. ........ 64

Figure 47. Three dominant ways to produce white light based on LEDs [102]. ........... 65

Figure 48. Several ways to generate white light based on LEDs implemented with di-, tri-, and tetra chromatic white sources [103]. ...................................................... 65

Figure 49. Spectral power distributions of several types of LEDs. .............................. 66

Figure 50. Comparison of the spectrum of ideal sunlight with two LED-based white-light sources. ......................................................................................................... 66

Figure 51. Spectral power distributions of early phosphor-based white LEDs (left), and white LEDs using more developed phosphors (right, in 2003) with increased output between 600 and 650 nanometers......................................................................... 67

Figure 52. Interface software "CSI-2015" for measure the surface roughness on the Linnik Fogale microscope......................................................................................... 69

Figure 53. Experimental arrangement of water-immersion Linnik head. BS, beam splitter (broadband, nonpolarizing); MO, microscope objective (water immersion); RM, reference mirror (80% reflectivity); PZT, piezo translation. ......................... 70

Figure 54. The schematic of how a correction collar works [106]............................... 71

Figure 55. Samples of water retaining SPA polymers in the bubble shape. ................. 72

Figure 56. Use of SPA beads in the mirror arm (a) and in the object arm (b). ............. 72

Figure 57. Design (right) and mold plate (left) for making PDMS slabs in various heights to suit the working distance of the objective............................................. 73

Figure 58. (a) An second improved mold design of PDMS made of Teflon with a glass plate forming the base of the mold, (b) PDMS contacts with reference mirror...... 73

Figure 59. Some PDMS slabs. ...................................................................................... 74

Figure 60. Difference focus positions of an aluminium layer on silicon sample placed under the sample objective with the thickness of PDMS slabs of (a) 3.4 mm, (b) 3.5 mm and 3.6mm; using ×20 immersion objective with a working distance of 3.6 mm. The best focus is (b)........................................................................................ 74

Figure 61. Comparison of fringe images of Al step on Si using red LED, ×20 immersion Linnik objectives in (a) air (0.05 step height, 26 dynamic range, $\lambda eff = 640$ nm, 4579); and (b) water (0.05 step height, 25 dynamic range, $\lambda eff = 640$ nm, [4580])........................................................................................................... 75

Figure 62. Comparison of raw fringe signal on Al step on Si using red LED, ×20 immersion Linnik objectives in air (top) (0.05 µm step height, 26 µm dynamic range, $\lambda eff = 640$ nm, 4579); and water (bottom) (0.05 µm step height, 25 µm dynamic range, $\lambda eff = 640$ nm, [4580])........................................................... 76

Figure 63. Comparison of fringe signals and fringe envelopes on Al step on Si using red LED, ×20 immersion Linnik objectives in (a) air (0.05 μm step height, 26 μm dynamic range, $\lambda eff = 640$ nm, rectify, 4579); and (b) water (0.05 μm step height, 25μm dynamic range, $\lambda eff = 640$ nm, FSA interpolation, [4580]). ........ 76

Figure 64. Comparison of fringe images of Al step on Si using red LED, ×40 immersion Linnik objectives in (a) air (0.05 μm step height, 21μm dynamic range, $\lambda eff = 640$ nm, 4584); and (b) in water (0.05 μm step height, 18 μm dynamic range, $\lambda eff = 640$ nm, [4585]). ........ 77

Figure 65. Comparison of raw fringe signals on Al step on Si using red LED, ×40 immersion Linnik objectives in air (top) (0.05 μm step height, 21 μm dynamic range, $\lambda eff = 640$ nm, 4584); and water (bottom) (0.05 μm step height, 18 μm dynamic range, $\lambda eff = 640$ nm, [4585]) ........ 77

Figure 66. Comparison of fringes signals and fringe envelopes on Al step on Si using red LED, ×40 immersion Linnik objectives in (a) air (0.05 μm step height, 21 μm dynamic range, $\lambda eff = 640$ nm, FSA interpolation, 4584); and (b) water (0.05 μm step height, 18 dynamic range, $\lambda eff = 640$ nm, FSA interpolation, [4585]). 78

Figure 67. Comparison of 3D images of Al step on Si using red LED, ×20 immersion Linnik objectives in (a) air (0.05 μm step height, 26 dynamic range, $\lambda eff = 640$ nm, rectify, 4579); and (b) water (0.05 μm step height, 25 dynamic range, $\lambda eff = 640$ nm, FSA technique [4580]). ........ 79

Figure 68. Comparison of 3D images of Al step on Si using red LED, ×40 immersion Linnik objectives in air (top) (0.05 step height, 21 dynamic range, $\lambda eff = 640$ nm, 4584); and water (bottom) (0.05 step height, 18 dynamic range, $\lambda eff = 640$ nm, [4585]) ........ 79

Figure 69. Comparison of the line profiles of the measured height of the Al step on Si using red LED, ×20 immersion Linnik head in air (shown in (a) and (c)) and in water (shown in (b) and (d)). The measurements of the step height (ΔZ) of the sample are 2.49 μm (0.05 step height, 25 dynamic range, $\lambda eff = 640$ nm, FSA interpolation, [4580]). ........ 80

Figure 70. Comparison of line profiles of the measured height of the Al step on Si using the 40x immersion Linnik head in air (shown in (a) and (c)) and in water (shown in (b) and (d)). The measurements of the step height (ΔZ) of the sample are 2.49 μm ) (0.05 step height, 18 dynamic range, $\lambda eff = 640$ nm, [4585]). ........ 80

Figure 71. Focus of the reference objective on reference mirror. An elastic polymer of (a) SPA and of (b) PDMS is placed between the reference mirror and the objective ........ 81

Figure 72. Etched squares in silicon, 8 µm wide and 2.5 um deep measured with the ×40 water immersion Linnik system (NA=0.8, $\lambda_{eff}$=450 nm) with SPA placed in the reference arm showing (a) height image, (b) line profile from (a), (c) fringe image and (d) 3D image. ........ 82

Figure 73. Etched squares in silicon, 8 µm wide and 2.5 um deep measured with the ×40 water immersion Linnik system (NA=0.8, $\lambda_{eff}$=450 nm) with 3.25 mm thickness of PDMS placed in the reference arm showing (a) height image, (b) line profile from (a), (c) fringe image and (d) 3D image. ........ 82

Figure 74. Fringe image of Al step on Si using white light, ×20 immersion Linnik objectives in water (0.05 µm step height, 12 dynamic range, $\lambda eff = 640$ nm, [4634-5]). ........ 83

Figure 75. (a) The raw fringe signal and (b) the fringe envelope on the Al step on Si using white light, ×20 immersion Linnik objectives in water (0.05 µm step height, 12 dynamic range, $\lambda eff = 640$ nm, [4634-5]). ........ 83

Figure 76. Line profile of the measured height of the Al step on Si using ×20 immersion Linnik objectives with white light in water (0.05 µm step height, 12 dynamic range, $\lambda eff = 640$ nm, [4634-5]). The step height of Aluminum on Silicon (ΔZ) and the measured lateral resolution (ΔX) are 2.50 µm and 0.2 µm respectively. ........ 84

Figure 77. Motorized control installed on block of the reference arm for adjusting the path length or reference arm. Images viewed in three sides are marked by red arrows (motor) and blue arrows (adapted plate). ........ 85

Figure 78. Graphic user interface for controlling the stepper motor (created by Husneni Mukhtar & Christophe Hoffman, IPHC). ........ 86

Figure 79. Flow-work of the interface for controlling the motorized stage in the reference arm. ........ 86

Figure 80. Results of measuring an etched silicon grating sample in water using the ×20 immersion Linnik Fogale microscope with the white light LED after motorized positioning of the OPD, showing the altitude image, a line profile and the 3D results [4701-4] ........ 87

Figure 81. Etched Silicon hole area-1, is measured by: (first row) the Zygo microscope in air (×50 Mirau, NA=0.55); (second row) the Fogale Linnik water immersion system (×40, NA=0.8, 0.056 µm step height, 5.5µm dynamic range, $\lambda_{eff}$=450 nm, [4721]); and (third row) the Fogale Linnik water immersion system (×20, NA=0.5, 0.056 µm step height, 10 µm dynamic range, $\lambda_{eff}$=450 nm, [4637]). ........ 88

Figure 82. Etched Silicon hole area-2 and area-3, measured by (first row) the Zygo microscope in air (×50 Mirau, NA=0.55,); (second row) Fogale Linnik water

immersion system (×40, NA=0.8, 0,056 μm step height, 4.5μm dynamic range, $\lambda_{eff}$=450 nm, [4721]); and (third row) AFM non-contact mode............................ 89

Figure 83. (a) The raw fringe signal and (b) the fringe envelope on the etched silicon sample no.16 h-3 using the Fogale immersion Linnik with the ×20 immersion objective and the white LED (0.05 μm step height, 9 dynamic range, $\lambda eff =$ 450 nm, [4667a])........................................................................................ 90

Figure 84. Etched Silicon, oval pattern, is measured by (first row) the Zygo microscope in air (×50 Mirau, NA=0.55); (second row) the Fogale immersion Linnik system in water (×40, NA=0.8, 0.056 μm step height, 6.3 μm dynamic range, $\lambda_{eff}$=450 nm, [4721]); (third row) AFM non-contact mode; and (fourth row) the Fogale Linnik immersion system in water (×20, NA=0.5, 0,056 μm step height, 14 μm dynamic range, $\lambda_{eff}$=450 nm, [4675a])................................................................... 91

Figure 85. Etched Silicon grating pattern, is measured by (first row) the Zygo microscope in air (×50 Mirau, NA=0.55); (second row) the Fogale Linnik immersion system in water (×40, NA=0.8, 0.056 μm step height, 5 μm dynamic range, $\lambda_{eff}$=450 nm, [4721]); (third row) the Fogale Linnik immersion system in water (×20, NA=0.5, 0.056 μm step height, 10 μm dynamic range, $\lambda_{eff}$=450 nm, [4674]); and (fourth row) AFM non-contact mode. ............................................. 92

Figure 86. 2 μm high Al step on Si is measured by (first row) the Zygo microscope in air (×50 Mirau, NA=0.55); and (second row) the Fogale Linnik immersion system (×20, NA = 0.5, 0.05 μm step height, 13 dynamic range, $\lambda eff = 450$ nm, rectify, [4644])........................................................................................................ 93

Figure 87. Illustration of the problem of lateral image displacement during axial scanning over a dynamic range of 5 μm using the x20 immersion Linnik: (a) measured area of displacement test; (b) Line profile of the measured area on a stack of scanned images, with a zoom of a specific area............................................... 95

Figure 88. Flowchart of proposed technique to measure the displacement of misalignment and to correct the image position.................................................. 95

Figure 89. Interface software "Image displacement analysis for CSI scanning" for checking and correcting the position of scanned images along the x- and y-axis caused by misalignment (created by H Mukhtar)................................................ 96

Figure 90. Description of three cases to test and observe the effect of misalignment. .. 96

Figure 91. The lateral displacement in x in pixels between successive images over 100 steps using the cross-correlation function. The dynamic range is 5 μm, dZ = 0.056 μm, $\lambda_{eff}$= 450 nm, for the x20 immersion objective............................................ 97

Figure 92. The shift along the x-axis between two images for each measurement using the cross-correlation function after 10× pixel resampling by a cubic kernel interpolation. Dynamic range= 5 μm, dZ= 0.056 μm, λeff= 450 nm, ×20 immersion objective. .... 98

Figure 93. The shift between successive images for each scanning step for the case of the x-axis. Dynamic range = 5 μm, dZ= 0.056 μm, λeff= 450 nm for (a) ×20 immersion objective and (b) ×40 immersion objective. Dynamic range = 10 μm, dZ= 0.056 μm, λeff= 450 nm for (c) ×20 immersion objective and (d) ×40 immersion objective.... 98

Figure 94. The lateral image shift for a short dynamic range (2.5 μm) of each objective and case. .... 99

Figure 95. The continuity trend of the lateral image shift during axial scanning for larger values of dynamic range (2.5 μm, 5 μm, and 10 μm): (a),(c) using ×20 immersion objective for case 1 and case 2; (b),(d) using the ×40 immersion objective for case 1 and case 2. .... 100

Figure 96. The shift response for different step heights (dZ) over the same dynamic range, using the ×20 immersion objective. .... 100

Figure 97. The lateral image shift between two images for each scanning step and cases along the y-axis. The dynamic range= 5 μm, dZ= 0.056 μm, λeff= 450 nm for (a) ×20 immersion objective and (b) ×40 immersion objective; The dynamic range =10 μm, dZ= 0.056 μm, λeff= 450 nm for (c) ×20 immersion objective and (d) ×40 immersion objective.... 101

Figure 98. Successive profiles of the grating for (a) before correction of the image shift measured in the same area using the ×20 immersion objective and (b) after correction of the image shift, 10 μm dynamic range and 0.056 μm step height... 102

Figure 99. The RS-N type resolution standard consists of a set of 9 gratings with different pitch values varying from 0.3, 0.4, 0.6, 0.8, 1.2, 2.0, 3.0, 4.0 and 6.0 μm. .... 103

Figure 100. Measurements of the RS-N type resolution standard using the ×40 immersion Linnik objective in water with the PSM technique ($\lambda eff = 505\, nm$). The grating sizes visible were (a) 0.8 μm; (b) 1.2 μm; (c) 2 μm; (d) 3 μm; (e) 4 μm; (f) 6 μm [4674b]. .... 104

Figure 101. Schema of the nano-3D interferometric microscope of Leitz Linnik in air [125].... 109

Figure 102. A microsphere-assisted interference microscopy. .... 110

Figure 103. Position of BTGMS on the sample using ×20 immersion Linnik Fogale microscope. The diameter of the microsphere is 67 µm, [4673b]........................ 111

Figure 104. Etched Silicon hole area-2 measured by ×20 immersion Linnik Fogale microscope, (first row) using a 67 µm BTGMS microsphere on it (0.05 step height, 10 dynamic range, $\lambda eff = 450$ nm, [4673b]); (second row) using a 64 µm-$BaTiO_3$ microsphere on it (0.05 step height, 12 dynamic range, $\lambda eff = 450$ nm, [4667-c2]).......................................................................................................... 112

Figure 105. Position of 67 um $BaTiO_3$ on the hole area-3 of etched Silicon, using ×20 immersion Linnik Fogale microscope. ............................................................. 113

Figure 106. Etched Silicon hole area-3 measured by ×20 immersion Linnik Fogale microscope, (first row) using a 67 µm BTGMS microsphere on it (0.05 step height, 14 dynamic range, $\lambda eff = 450$ nm, [4678]); (second row) using a 61.7 µm-$BaTiO_3$ microsphere on it (0.05 step height, 10.5 dynamic range, $\lambda eff = 450$ nm, [4681])........................................................................................................... 113

Figure 107. Position of a 70 µm BTGMS on sample in water using Fogale microscope. .......................................................................................................... 114

Figure 108. Etched Silicon on oval pattern measured by ×20 immersion Linnik Fogale microscope using a 7 µm BTGMS microsphere on it (0.05 step height, 15.5 dynamic range, $\lambda eff = 450$ nm, [4675b])....................................................... 114

Figure 109. Position of a 71 µm BTGMS on the sample in water using the Fogale microscope. .......................................................................................... 115

Figure 110. Etched Silicon on grating pattern measured by ×20 immersion Linnik Fogale microscope using a 71 µm BTGMS microsphere on it (0.05 step height, 18 dynamic range, $\lambda eff = 450$ nm, [4674b])....................................................... 115

Figure 111. Standard grating SiMETRICS measured by ×40 immersion Linnik Fogale microscope, red LED, 0.056 µm step height, $\lambda eff = 530$ nm in water: pitch 1.2 µm (11 dynamic range, using 43 µm BTGMS); pitch 0.8 µm (5 dynamic range, using 44 µm BTGMS); pitch 0.4 µm (6.5 dynamic range, using 45 µm BTGMS); pitch 0.3 µm (6.5 dynamic range, using 43 µm BTGMS), [4714]....................... 117

Figure 112. Standard grating SiMETRICS measured by ×40 immersion Linnik Fogale microscope, red LED, 0.090 step height, $\lambda eff = 505$ nm in water: pitch 3 µm (11 dynamic range, using 80 µm BTGMS); pitch 2 µm (10 dynamic range, using 80 µm BTGMS); pitch 1.2 µm (10 dynamic range, using 82 µm BTGMS); pitch 0.8 µm (10 dynamic range, using 77 µm BTGMS); pitch 0.6 µm (10 dynamic range, using 77 µm BTGMS); pitch 0.4 µm (10 dynamic range, using 75 µm BTGMS), [4716]........................................................................................................... 118

# TABLE OF ANNEXES

Annex 1. Data sheet of the light source of initial Fogale, Lumileds LXHL-MW1D white LED, 5500K, round ........ 137

Annex 2. Data sheet of cube beam splitter of Fogale microscope ........ 139

Annex 3. Specification of immersion objectives from Leica. ........ 140

Annex 4. Design of the adapted tube for objective in reference arm. ........ 141

Annex 5. Data sheet of white light LED (lime LED color) ........ 142

Annex 6. The procedure of Abbe-refractometer ........ 143

Annex 7. Data sheet of motorized MFA-PP ........ 144

# TABLE OF ABBREVIATIONS AND ACRONYMS


AFM : Atomic Force Microscope ........ 8, 12
ATR-FTIR : Attenuated Total Reflectance Fourier Transform Infrared spectroscopy ........ 2, 50
BTGMS : Barium Titanate Glass microspheres ........ 109, 116
CCI : Coherence Correlation Interferometry ........ 21
CPM : Coherence Probe Microscopy ........ 2, 21
C-S-H : calcium silicate hydrate ........ 3, 57, 59
CSI : Coherence Scanning Interferometry ........ 2, 25
CSM : Coherence Scanning Microscopy ........ 21
DHM : digital holographic microscopy ........ 19
DOE : diffractive optical element ........ 57
FF-OCT : full-field optical coherence tomography ........ 2, 28, 41
FFT : Fast Fourier Transform ........ 27
FOV : field of view ........ 19
FSA : Five Step Adaptive ........ 28, 54
FWHM : full width at half maximum ........ 29, 32
LED : light emitting diode ........ 41, 57, 62
LVDT : linear variable differential transformer ........ 6
MEMS : microelectromechanical system ........ 5, 26
MOEMS : micro-opto-electro-mechanical system ........ 5, 26
NA : numerical aperture ........ 29, 30, 32
OBD : optical beam deflection ........ 13
OLD : Objective Lens Distance ........ 42
OPD : optical path difference ........ 23, 24, 27, 61
PBS : polarizing beam splitter ........ 41
PDMS : polydimethylsiloxane ........ 71, 72, 81
PFSM : peak fringe scanning microscopy ........ 27
PSF : point spread function ........ 28, 29, 31
PSI : phase shifting interferometry ........ 18
SBF : simulated body fluid ........ 2
SIMI : Simultaneously Immersion Mirau Interferometry ........ 18
SPA : sodium polyacrylate ........ 71, 80
SPM : Scanning Probe Microscopy ........ 7, 11
STM : Scanning Tunneling Microscopy ........ 8, 9, 12
SWLI : Scanning White Light Interferometry ........ 22
VSI : Vertical Scanning Interferometry ........ 22
WD : Working Distance ........ 42
WLI : white light interferometry ........ 7
WLSI : White Light Scanning Interferometry ........ 2, 16, 21, 34

# RÉSUMÉ

La profilométrie optique en microscopie interférométrie est une technique d'imagerie optique 3D bien établie permettant la caractérisation de surfaces d'une manière non-invasive, rapide et avec une résolution axiale nanométrique. Cette technique de mesure est parfaitement adaptée à la mesure de rugosité de surface pour des structures ou circuits microélectroniques, des éléments optiques diffractifs, des systèmes micro-électromécaniques (MEMS) ou des dispositifs de micro-fluidiques. L'Interférométrie en lumière blanche CSI (Coherence Scanning Interferometry, également connue comme White Light Scanning Interferometry, WLSI) est une technique basée sur la détection du pic ou de l'enveloppe de franges d'interférence. La technique utilise un échantillonnage des franges selon l'axe optique par l'acquisition d'une pile d'images XYZ. Le traitement d'image est ensuite utilisé pour identifier les enveloppes des franges, le long de l'axe Z pour chaque pixel afin de mesurer la position d'une surface unique ou de structures enterrées dans une couche. La mesure de la forme de la surface en CSI, nécessite un traitement basé souvent sur la détection d'un pic directement sur les franges ou sur l'enveloppe des franges après extraction de celle-ci à l'aide d'algorithmes de traitements implémentés voir développés dans notre équipe. Les avantages de la CSI sont la sensibilité axiale nanométrique, le champ de vision large (de quelques centaines de µm à plusieurs mm) et la vitesse de mesure (quelques secondes à quelques minutes selon les algorithmes ou leur plateforme d'implémentation).

Classiquement les microscopes interférométriques se limitent aux mesures des échantillons dans l'air. A l'instar de la microscopie 2D dans le domaine biologique, différents groupes de recherche cherchent à développer la microscopie interférométrique en milieu liquide. Le travail dans un milieu liquide permet, outre l'amélioration de la résolution latérale en microscopie optique, d'ouvrir le domaine d'application à l'étude d'échantillons nécessitant l'immersion dans de l'eau ou dans du sérum physiologique. Une demande croissante de mesures nanoscopiques en milieu liquide, comme l'étude de la croissance de couches d'hydroxyapatite sur des implants (dents, prothèses, …) ou plus particulièrement l'étude de couches de colloïdes pour l'étude de réactions chimiques.

Ce travail de thèse se fait dans le cadre du développement instrumental d'un microscope interférométrique de type Linnik en immersion à haute résolution axiale et fort grossissement. L'étude bibliographique a permis d'établir un état de l'art dans le domaine de la microscopie interférométrique en immersion. Elle a également permis de mettre en évidence les verrous scientifiques et technologiques à lever afin de réaliser un système opérationnel en immersion. Dans ces travaux sont présentés l'adaptation d'un interféromètre industriel construit par la société FOGALE pour la mesure en immersion et appliqué à la mesure de couches d'agrégats de colloïdes étudiées par le groupe de radiochimie de l'IPHC.

Le microscope FOGALE est architecturé autour d'une tête interférométrique de type Linnik classique. Un des verrous technologiques à résoudre lors du travail en immersion dans un interféromètre Linnik est la compensation du chemin optique dans le bras miroir lorsque le bras objet se trouve en immersion. La difficulté vient principalement de l'implémentation horizontale du bras miroir, ce qui rend difficile l'immersion du miroir dans le liquide.

Une première solution étudiée dans ce cas était l'utilisation et l'insertion de lamelles de verre entre l'objectif et le miroir. La difficulté d'insérer des verres adéquats en épaisseur et en indice ne permettait pas d'adapter les chemins optiques de façon optimale afin d'obtenir des franges de qualité dans le plan focal. Le contraste des franges ne permettait pas de réaliser des mesures de qualité avec une telle compensation. Il est également apparu un problème de réglage extrêmement délicat de l'interféromètre dû principalement à des problèmes de choix de construction limitant les réglages fins et l'alignement précis des éléments optiques mais également au choix du nombre de degrés de liberté (rotations et translations) de certains éléments du système.

Dans une seconde phase et afin de pouvoir réaliser des tests et des mesures sur les premiers échantillons, nous avons adapté un objectif interférométrique compact de type Mirau pour les mesures dans l'air. Les principaux inconvénients d'une telle solution sont le grossissement et la résolution limitée que l'on peut obtenir avec de tels types d'objectifs et la difficulté de les faire fonctionner en immersion. Le travail de thèse s'est donc concentré principalement sur la levée des différents verrous pour développer une structure d'interféromètre Linnik utilisable et réglable dans des conditions d'expérimentation acceptable par l'utilisateur final.

Une première étude a donc consisté à trouver et à modifier les systèmes de réglage mécanique afin de garantir l'ensemble des degrés de liberté afin de permettre un réglage optimal du Linnik. Le réglage du bras miroir a été motorisé afin de faciliter la recherche des franges dans le plan focal de l'objectif. Le contrôle de cet actionneur est développé sous LabView. Il permet la recherche aisée des franges d'interférence. Ce système pourra évoluer dans le futur par l'implémentation d'un algorithme de recherche automatique des franges en intégrant un système de reconnaissance et de détection des franges grâce à la caméra associée à un traitement développé sous LabView.

Une seconde partie est consacrée à l'étude des solutions de compensation du chemin optique entre le miroir de référence et son objectif. Une étude des différentes solutions possibles de compensation a été réalisée. Deux solutions prometteuses ont été testées et mis en œuvre qui évite utilisation d'eau liquide ou un repliement vertical du bras de référence. La première solution est basée sur l'utilisation de billes de polyacrylate de sodium (SPA). Cette solution utilise les propriétés des polymères de polyacrylate de sodium à absorber de très grande quantité d'eau et leur confère ainsi un indice de réfraction très proche de l'eau. Les caractéristiques optiques sont donc très proches. Les

résultats de mesure sont présentés et ont permis de montrer la viabilité de cette solution. La mise en œuvre des billes de SPA est relativement simple et peu chère. L'inconvénient est la durée d'utilisation qui est limitée à une journée voir quelques heures et causée par l'évaporation de l'eau du polymère.

La seconde solution consiste à utiliser des pastilles de PDMS moulé sur mesure pour notre application. Pour cela un moule fut conçu et fabriqué en téflon. Une caractéristique indispensable de ces pastilles est, outre les caractéristiques optiques (qualité, indice, …), l'élasticité ou la souplesse indispensable pour éviter une déformation du miroir de référence lors de l'assemblage sur l'objectif de référence. Un ensemble de mélange et un procédé d'élaboration a dû être développé pour atteindre des performances acceptables. Si les résultats sont prometteurs, il reste cependant encore à optimiser la qualité optique de ces éléments afin d'augmenter la qualité des franges d'interférences. Ces techniques de compensation ont été appliquées à notre banc de mesure et pour deux grossissements de jeux d'objectifs à immersion en X20 et X40.

Une campagne de caractérisation du microscope a été menée et les résultats sont présentés dans la thèse sur des échantillons de référence et en immersion. Ces mesures sont comparées à des mesures sur des appareils de référence comme des mesures en AFM ou sur le système de mesure interférométrique commercial Zygo disponible sur notre plateforme de caractérisation. Enfin les premières mesures sur des échantillons en immersion de couches de colloïde sont présentées et ont permis de valider le microscope interférométrique en immersion.

Le cadre du projet de thèse se situe dans une collaboration avec le Professeur Rémy Barillon et le groupe de radiochimie du Département Recherches Subatomiques (DRS) de l'IPHC (Institut Hubert Curien). Le but est de développer un système de CSI en immersion pour le combiner avec la spectroscopie FTIR dans l'analyse de couches de colloïdes en immersion pour étudier les polluants dans le sol.

# INTRODUCTION

Coherence Scanning Interferometry (CSI) is a non-contacting 3D optical profilometry technique that is increasingly used for measuring the roughness and shape of microscopic material and component surfaces [1], such as microelectronic structures, miniature optical elements, micro-electro-mechanical systems and micro-fluidic devices. The technique is also known as White Light Scanning Interferometry (WLSI) or Coherence Probe Microscopy (CPM). The particular advantages of CSI are nanometric axial sensitivity (1 nm), a wide field of view (hundreds of µm to several mm) and high speed of measurement (several seconds to several minutes).

Classically, measurements are limited to dry surfaces in air that are static. In more recent research projects, several new modes of measurement have also been developed: the strobed technique for periodically moving surfaces [2], the 4D microscopy real time mode for measuring aperiodically moving or changing surfaces at a rate of up to 25 3D images per second [3], the tomographic mode, or full-field optical coherence tomography (FF-OCT) for measuring transparent complex layers [4] and the local spectroscopy mode for measuring local optical properties [5].

In the present project, we are interested in being able to study samples in liquids, such as in the case of chemical reactions or biological samples. In order to be able to measure such samples, several challenges need to be overcome such as making a system that works correctly in liquids and developing techniques to compensate for the dispersion mismatch and optical aberrations between both interference arms when imaging samples in a liquid medium or inside tissue or living cells, etc.

The objectives of this PhD research project are to extend the measurement modes [6] of the CSI technique to be able to cope with samples in a liquid medium at high speed using a fringe scanning system by developing an immersion interferometer head based on the Linnik interferometer using immersion objectives.

One area of interest for the application of the new technique will be in the in-situ characterization of the chemical exchange in thick layers of colloids for environmental applications in combination with Attenuated Total Reflectance Fourier Transform Infrared spectroscopy (ATR-FTIR, in collaboration with the team of Rémi Barillon, IPHC, Strasbourg). Another area of application is in the study of the growth of layers of synthetic biomaterials such as hydroxyapatite (the mineral part of bones and teeth) in simulated body fluid (SBF), an important material used in human implants [3] [8]. The technique could also be used in the analysis of the properties of the surface and sub-surface region of the skin in order to help in identifying different skin disorders [7].

The manuscript consists of four main chapters and is organized in the following way. In the first chapter, we give a summary of several existing surface profiling techniques by presenting the principle work, the utilities and a comparison between them. This demonstrates the usefulness of interference microscopy for many types of measurements, with its high axial and lateral resolutions and other advantages. After

having recalled the interest of interference microscopy compared with other optical profilers, we then present the state of the art of the two methods widely used and the lateral and axial resolutions.

The second chapter presents the different Linnik setups that exist, including their measurement performance in air and liquid. In this way, it is demonstrated that the immersion Linnik system has a high potential for improving the lateral resolution of surface roughness measurement and being able to measure samples in a liquid medium. The different challenges for designing the Linnik interferometer are presented, showing the need for path length compensation in the reference arm.

The third chapter is devoted to the overall work that has been performed to adapt a commercial (Fogale Nanotech) Linnik microscope to be able to work in the immersion mode. We begin by introducing the conditions of the initial system. This is then continued by illustrating in sequence the modification steps of this initial system to achieve the water immersion Linnik. Each modification step presents the description of the instrument, the measurement tests carried out and discussion. The presentations cover the work carried out on studying the different solutions for path length compensation using self-supporting polymers. The system is tested with measurements on calcium silicate hydrate or C-S-H colloids on Ge substrate and some patterns of etched Silicon. The result comparison is also carried out with other microscopes. A specific section of the discussion is presented to discuss the specific problems encountered during the work.

In the fourth and final chapter, the new immersion system is tested with the recently discovered microsphere assisted microscopy technique that allows a considerable improvement in the lateral resolution, or the effect of "super-resolution". Test samples of etched Si samples measured with barium titanate microspheres (64 µm to 71 µm in diameter) combined with CSI technique in water show an improvement in additional magnification up to 3.01 times. Then test samples of standard grating from SiMETRICS measured with barium titanate microspheres (43 µm to 82 µm in diameter) combined with Phase Shifting Microscopy (PSM) technique in water show an improvement in lateral resolution from 800 nm with the immersion objective alone to 300 nm with the microsphere. This demonstrates the high potential of the immersion Linnik for very high resolution optical measurements of surface roughness and structures.

A general conclusion summarizes the main conclusions of the research project.

# CHAPTER 1
# 3D SURFACE PROFILING

## 1.1 Existing measurement systems

The measurement of microscopic surface roughness and 3D surface structures is an important field of materials development and industrial metrology and inspection. Measurement techniques are required for characterizing new materials, microelectromechanical system and micro-opto-electro-mechanical system (MEMS and MOEMS) as well as traditional materials such as metallic surfaces, paper and plastics. In ISO 25178 part 6 (2010), three classes of methods of instruments for measuring surface texture are defined as shown in Table 1. These consist of the 2D graph or profile of the surface topography method, represented mathematically as a height function, z(x); the topographical surface image of the surface measurement method, represented mathematically as a height function, z(x,y); and the representative surface area of the surface measurement method of which the numerical results produced depend on the area-integrated properties of the surface texture. This last method will not be discussed in this thesis. The various techniques for contact profilometers and optical profilometers to measure the surface topography are now described in this section.

Table 1. The classification of methods for measuring surface texture based on ISO 25178-6 2010 [8].

| Profiler method | Linear profiling (senses Z(X) | Areal topography Senses Z(X,Y) or Z(X) as function of Y | Areal-Integrating |
|---|---|---|---|
| Angle Resolved Scatter | | | ✓ |
| Angle Resolved SEM | | ✓ | |
| Circular Interferometric Profiling | ✓ | ✓ | |
| Coherence Scanning Interferometry | | ✓ | |
| Confocal Chromatic Microscopy | | ✓ | |
| Confocal Microscopy | | ✓ | |
| Contact Stylus Scanning | ✓ | ✓ | |
| Digital Holography Microscopy | | ✓ | |
| Focus Variation Microscopy | | ✓ | |
| Optical Differential profiling | ✓ | ✓ | |
| Parallel Plate Capacitance | | | ✓ |
| Phase Shifting Interferometry | ✓ | ✓ | |
| Pnematic | | | ✓ |
| Point Autofocus Profiling | | ✓ | |
| Scanning Tunneling Microscopy | | ✓ | |
| SEM Sterescopy | | ✓ | |
| Structured Light Projection | | ✓ | |
| Total Integrated Scatter | | | ✓ |

### 1.1.1 Contact profilometers

Two main contact profilometers are the stylus profiler and near field scanning probe microscope, that use a tactile probe to measure the surface profile. Their measurement performance differs in terms of the lateral and vertical resolution and range, and the different application aims.

**Stylus profiler**

Stylus profilers are the oldest techniques used to measure surface roughness by moving the object surface under the stylus tip or by moving the small-tipped probe across the surface and sensing the height variations of the stylus tip to determine the surface height profile [9].

This technique has become the traditional method in research and industry for several decades. Invented by Schmalz in 1929 [10], the profiler had a vertical resolution of approximately 25 nm and was able to successfully obtain a surface profile with a magnification of greater than 1000× by recording the motion of the sharp probe mounted at the end of a cantilever. This probe was monitored using an optical lever arm. In 1971 Russel Young introduced the topografiner [11], a non-contact mode of stylus profiler. The estimated resolution was 3 nm perpendicular to the surface and 400 nm in the plane of the surface. This topografiner used the electron field emission current between the distance of a sharp metal probe and the surface for feedback control. Later in 1981 J. Bennett et al. [12] used a sharp stylus to obtain height resolution of the order of 1–2 Å and a lateral resolution of a few tenths of a micrometer on smooth surfaces. In 1987, G.A. Al-Jumaily et al. developed a computational model to track the motion of a spherical stylus [13].

Another variation of the stylus profiler, shown in Figure 1, consisting of a profiler with an assembly of a linear variable differential transformer (LVDT) and fixed stylus, can be used to detect the vertical position and convert the signal to height data [9]. This motion detector scans the surface by moving across the sample with a certain sampling interval.

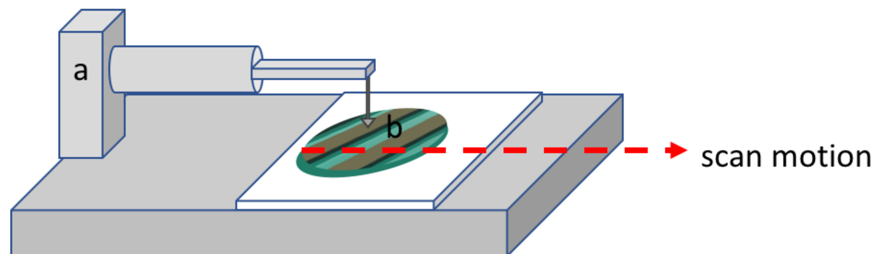


Figure 1. Schematic of stylus profiler with LVDT as the motion detector. Part a is a fixed stylus with LVDT assembly and b is a sample.

Choosing the configuration of a stylus tip for surface measurement is extremely important in terms of the penetration to the bottom of steep trenches and in preventing the rounding-off of high surface peaks. As illustrated in Figure 2, the size of a stylus tip affects the measurement of various trench ratios. The shortest period of measurable wavelength (d) of the sinusoid using a spherical tip, based on Eq.1 [12] [9], depends on the stylus radius (r) and on the amplitude of the sinusoid (a).

$$d = 2\pi\sqrt{a\,r} \qquad \text{(Eq.1)}$$

The radius of the stylus tip, besides the surface shape and the sampling interval between data points, is one of the important parameters in determining the lateral resolution. The load of the stylus is also considered to keep the stylus on the surface and so as not to damage or deform the sample when the stylus moves across it. The smaller and sharper is the tip radius, the more easily it can follow the shape of the surface but other factors such as the local force on the surface and the surface elasticity should be considered for obtaining an accurate result.

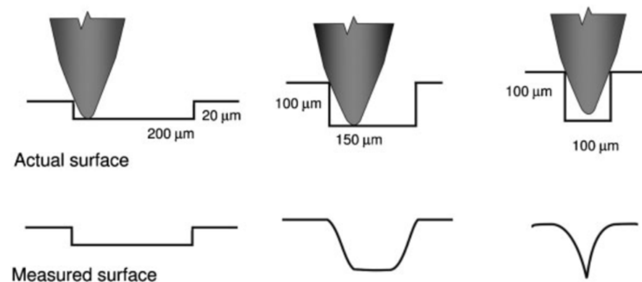


Figure 2. Illustration of stylus profiler scanning over the surface of trenches with various aspect ratios. The convolution of a 25 µm radius stylus tip with a surface profile [9].

S. Jaturunruangsri [14] in his research compared the results of a stylus profiler with those of white light interferometry (WLI) for the characterization of materials (ceramic, quartz and tungsten) and in terms of the surface parameters (the average height and the maximum peak to valley height). The results showed that the two techniques have a similar high accuracy when measuring a small step height of 0.33 µm, but the stylus profiler gave better result of the step height for those greater than 1 µm.

While the stylus profiler has become a standard in industry, with many ISO standards having been developed, the technique has several disadvantages such as a relatively low scanning speed which can lead to a thermal increase in the sample and a lack of lateral resolution due to the tip geometry.  The stylus is also less applicable for certain surfaces due to possible damage due to the contact force exerted by the tip [15][16].

***Near field scanning probe microscopy***

Following the stylus profiler, in the 1980's, a radically new technology involving near field microsopy was developed. The first mode was Scanning Probe Microscopy (SPM)

that works by moving a fine tip in close proximity to the sample surface, to within several nm to a few angstroms depending on the technique. The gap between the probe and the sample determines the lateral resolution [17]. These instruments have much higher axial and lateral resolutions than the stylus probe and hence are capable of obtaining nanometric and even atomic scale resolution [9].

***Scanning Tunneling Microscopy***. The first scanning probe microscope, or the precursor to the AFM, was a Scanning Tunneling Microscopy (STM) developed in the early 1980s at IBM Research-Zurich by Gerd Binnig and Heinrich Rohrer who won the Nobel Prize in 1986 and first published in 1983 [18]. This novel type of microscope was developed based on quantum tunneling and results in an unprecedented resolution in real space on an atomic scale. Many challenging technical problems were encountered to achieve a working system, such as the suppression of external vibration and the vibration-free approach of sample and tip and vibration from piezo actuators. However, they succeeded in demonstrating that STM is able to clearly resolve individual atoms on a surface, less than 7 Å apart.

STM works based on the concept of quantum tunneling as shown in Figure 3. (a) The schematic view of STM; Two typical modes of STM: (b) constant-current mode, and (c) constant-height mode [19].

Quantum tunneling refers to the quantum mechanical phenomenon where a particle tunnels through a barrier that it classically could not surmount. A conducting scanning tip or probe is placed very near to the surface, which then detects the tunneling current and the force between atoms of the probe and the sample [17].

There are two typical modes in STM shown in Figure 3 (b) and (c) respectively. The first one is the constant-current mode, in which the position of a probe tip depends on a constant charge density of the sample surface. A voltage response is fed back to piezo to adjust the height between the probe tip and surface during the scanning [19]. These voltage changes are also used to determine the surface topography. The second consist of the constant-height mode, the voltage and the height between probe tip and surface being kept constant during the scanning process [19]. In consequence, the current change will be related to charge density. Thus, based on the principal work of the two modes, the constant-height mode is relatively faster than the constant-current mode, since more time is required to adjust the height change of the piezo in the constant-current mode.

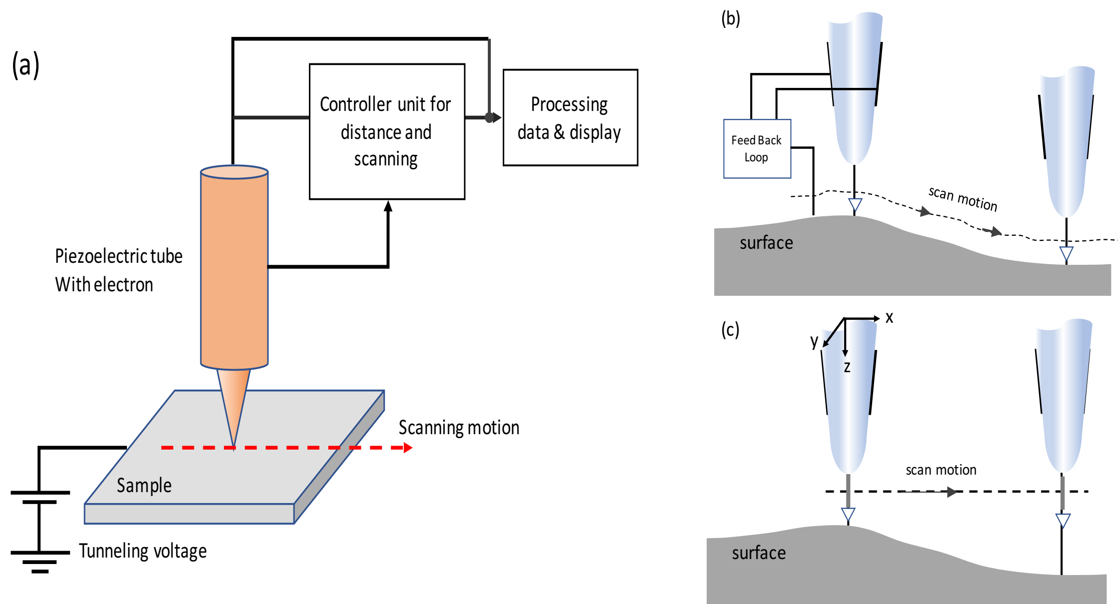


Figure 3. (a) The schematic view of STM; Two typical modes of STM: (b) constant-current mode, and (c) constant-height mode [19].

STM has been used for the 3D surface profiling of roughness, defects and other characteristics with a 0.1 nm lateral resolution and 10 pm depth resolution [19]. It is of particular interest for use in the analysis of clean surfaces with atomic resolution [17] and it can also be used in the different conditions of vacuum, air, water, liquid, and gasses with the operating temperature ranging from 0 up to a few hundred Kelvin.

Even though STM is ideal for an atomic scale resolution, there are some limitations and drawbacks, such as the requirement for high vibration control, a sharp tip, a clean and stable surface [20], a high sensitivity to contaminants, the need for skill and precision of the operator, well conducting samples, and an expensive instrument [21].

***Atomic Force Microscope***. In 1986 Binnig then invented the Atomic Force Microscope (AFM), the most popular SPM, and also known as Scanning Force Microscopy (SFM). The first experimental implementation was made by Binnig, Quate and Gerber in 1986 **[22]**, with the first commercial AFM being introduced in 1989. AFM is a microscopy technique that can provide 3D images of surfaces generally at the nanometer scale. It is not only used for measuring surface topography but also for characterizing many surface properties by applying various motions and signals that drive the probe.

AFM was developed to extend the STM technique in order to be able to use it for non-conductive materials [23][24], as well as biological samples such as cells, bacteria, viruses and proteins, etc. Basically, AFM combines the principle of STM with stylus profiling [21] by detecting the deflection of a cantilever when scanning the sample. This change in deflection is then processed to obtain the surface roughness, surface morphology and force distribution information.

There are three primary imaging modes in AFM:

1) The contact mode with a probe-surface separation of < 0.5 nm.

2) The tapping mode or intermittent contact with a probe-surface separation of 0.5-2 nm.

3) The non-contact mode with a probe-surface separation of 2-10 nm.

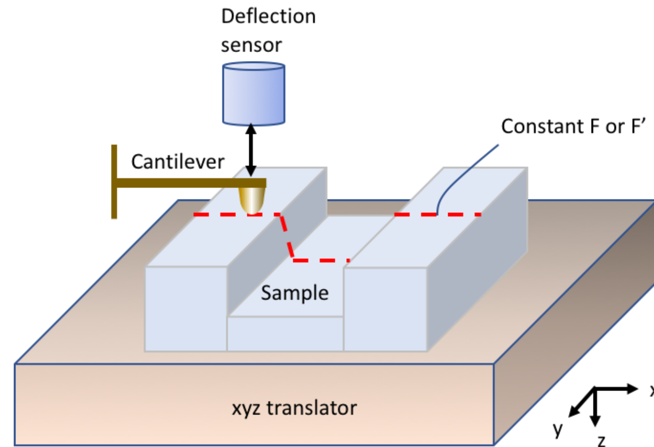


Figure 4. The force F in the contact mode and the force gradient F' in the con-contact mode is measured during scanning. The deflection sensor detects the deflection of the cantilever [21].

In the contact-mode, the cantilever deflection generated by the interaction force between the tip and the sample is monitored by a sensor. A constant force is maintained and adjusted using a feedback circuit. The force is represented and calculated using Hooke's law as following:

$$F = -kx \qquad \text{(Eq.2)}$$

where F is the force, k is the spring constant, and x is the cantilever deflection. A vertical resolution of less than 0.1 nm and a lateral resolution of better than 0.3 nm have been obtained using this mode in several reports [25][26]. Whilst in the non-contact mode, the force gradient is obtained by vibrating the cantilever and measuring the shift in the resonant frequency of the cantilever. Figure 4 shows these two contact modes.

Figure 5 shows the most common AFM approach, the Tapping Mode [27][28]. This mode overcomes some of the limitations of both the contact and noncontact modes by eliminating lateral shear forces that can damage soft samples and reduce image resolution.

Choosing a cantilever with an appropriate tip is a requirement to obtain high vertical and lateral resolution. A good sharp tip has an extremely low spring constant at small forces equal to 0.1 N/m or lower and a high resonant frequency (10-100 kHz) to minimize the vibration sensitivity.

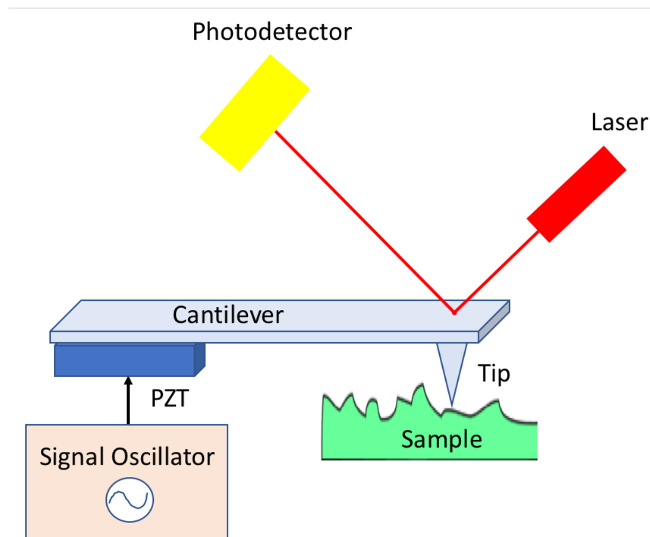


Figure 5. Schematic of signal detection in AFM Tapping Mode. The probe is kept at a constant level above the sample, which results in a constant amplitude signal. Changes in the amplitude of the signal indicate that the distance between cantilever and object has changed [9].

The sensor is an important component used for sensing the force on the tip due to its interaction with the sample by detecting the deflection of the cantilever during the scanning process. There are four methods commonly used for this detection system as illustrated in Figure 6. Binnig et al. [22] used the electron tunneling method in their first version of AFM. The cantilever deflection is monitored by force sensing of the second tip placed near the cantilever. On the contrary, other deflection sensors are placed at a range of several micrometers to tens of millimeters from the cantilever. The optical beam deflection method has the largest working distance and is insensitive to distance change because it is more sensitive, reliable and easily implemented and is hence commonly used in commercial SPMs [21].

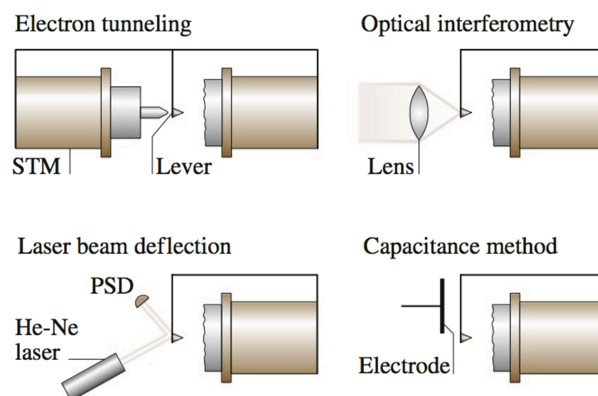


Figure 6. Schematic of variations of detection systems [21].

Developments are such that very high spatial resolution and force sensitivity have been attained in AFM so that sub-atomic structures can be visualized [29][30], single electron spins resolved [31] and the atom type on a solid surface distinguished [32]. AFM is now widely used for materials characterization and for measuring surface structures. But, like STM, AFM also has its disadvantages such as slow scanning speed, expensive tips [9], easy tip damage and a need for high skill level to obtain good results. There is also the problem of the tip (radius and shape) convolution with that of the surface structure in the measured profile. The scanning devices are not free from noise and are affected by linear or nonlinear distortions [21].

***Atomic Force Microscope in Liquid***

While most AFM systems work in air, imaging with liquid-based AFM is rapidly growing, covering about 40 % of current AFM research and being an important tool for the study of biological materials [33] and observation of biological specimens by using it as a buffer to closely mimic the original conditions [34].

The research using AFM in liquids began about the same time as that in air. For example, AFM on surfaces covered with liquids attained lateral and vertical resolutions of 0.15 nm and 5 pm in 1987 [35] and the monitoring of a complex biomolecular process in a liquid chamber was performed in 1994 (Figure 7) [36]. In the same year, a tapping mode AFM with a standard silicon nitride cantilever in air that can be used in liquid was also published [37], using a sufficiently high energy oscillating cantilever to overcome the adhesion of the water layer. Moreover, this mode is better than the contact mode for use in liquids, using less force and with a less destructive influence of the lateral forces. In 2005 T.Fukuma et al. [38] demonstrated the predominance of true atomic resolution of Frequency Modulation AFM (FM-AFM) in liquid and obtained a vertical resolution of 2-6 pm and lateral resolution of 300 pm.

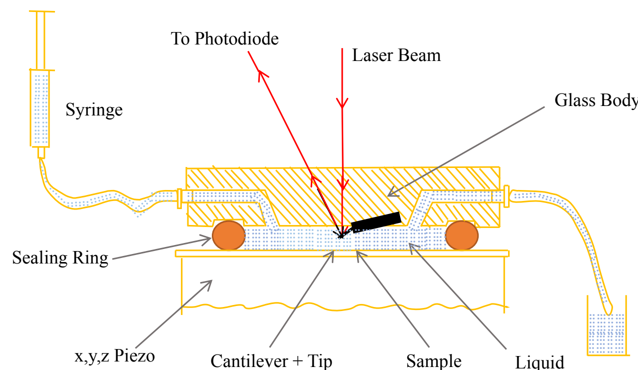


Figure 7. An experimental scheme of a scanning force microscopy liquid cell of RNA polymerase [36]. A volume of 30 µl distilled water and some variations of other buffer types filled the chamber via the hosting and syringe. It took several minutes to 2 hours to reach the mechanical and thermal stability before performing imaging.

AFM in liquids is nowadays growing even further and is widely used for studying the dynamic behaviour of biomolecules in the field of biology, biomolecular and medical studies by improving the scan rate and reducing the interaction force between the sample and probe tip [39]. A high speed atomic force microscopy system developed in 2001 by T.Ando et al. [40] [39], illustrated in Figure 8, could capture a 100x100 pixel image of moving protein molecules on video at 80 ms/frame. The system is integrated with an optical beam deflection (OBD) method to detect cantilever deflection [29]. OBD is one of methods in AFM to detect the cantilever deflection. Other methods to detect the cantilever deflection are capacitance or laser interferometry and the STM tip. The cantilever deflection is represented by:

$$\Delta\varphi = \frac{3\Delta z}{2L} \qquad \text{(Eq.3)}$$

where Δφ and Δz are the changes of displacement and angle of the free end of the cantilever, respectively, and L is the cantilever length.

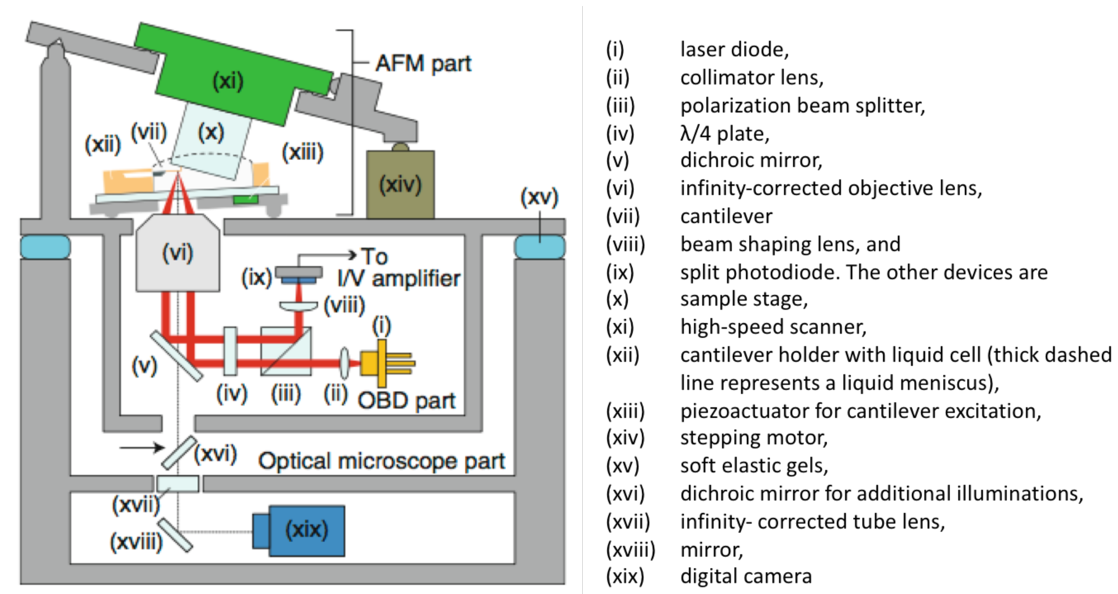


Figure 8. Illustration of high speed atomic force microscopy head integrated with OBD system [29].

The liquid setup for AFM can generally be categorized into two types: the open cell or closed cell, as shown in Figure 9. In the open cell, known as the microcell, the sample is held in a small vessel with an amount of liquid [41] and the probe is submerged in the liquid during scanning. In the closed cell, also known as an environmental cell, the sample and probe are held in a small enclosed area. The cell is formed by a glass plate at the top, and a rubber diaphragm at the bottom. The top and bottom of the cell are sealed, and the liquid is introduced into the cell. The open and closed cells are illustrated in 10 (a) and (b) in respectively.

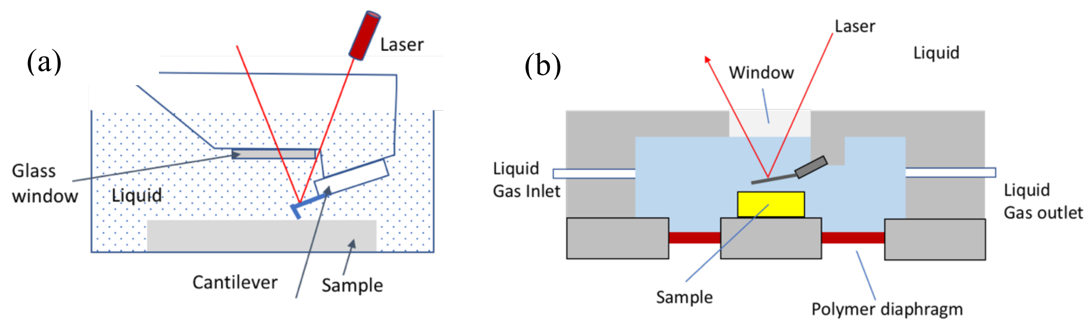


Figure 9. Illustration of two designs of immersion AFM in open (a) and closed (b) liquid cells [41].

It is typically much simpler to use an open cell for scanning in liquid than in an environmental cell since there is not the problem of the formation of air bubbles that can easily form on the surface of a glass window as in the closed cell. The advantage of using the closed cell is that the liquid can flow through the cell during scanning or for use in an inert gaseous environment [41]. On the other hand, it takes several days to acquire images with a closed cell, compared with the open cell, which takes only a few hours.

In conclusion, while AFM has the advantages of nanometric resolution, the images take in general several minutes to several hours to acquire. Moreover, an ideal probe tip has a high aspect ratio compared with the surface sample features in order to give the best resolution, which requires slower scanning. In the next subsection, we will now discuss the second type of profiler, the optical profiler, which on the contrary allow high speed surface profiling.

## 1.1.2 Optical profilers

Several types of optical profilers exist. Rather than using a mechanical probe, either a point optical probe can be scanned laterally over an area for measuring surface height or an imaging probe can be scanned over the depth to map the surface topography over a large area. Optical probes have the advantage of not being in contact with the sample surface. Some of these techniques are now described.

***Optical Ranging Sensors***. An optical ranging sensor consists of a light emitting part, a light receiving part, and a processing system. This technique, can be usefully applied in automation applications such as assembly, inspection and military applications [42]. A point optical ranging sensor typically measures absolute distances or lengths at a single point using a detector, optoelectronics and specific signal processing techniques [9]. Based on the capabilities of different sensors of the range accuracy, depth of field, and image acquisition time, several types of sensors are used to obtain range images, i.e.

radar, triangulation, moiré, holographic interferometry, lens focusing, diffraction [42], and time of flight [43].

The distance resolution of each sensor depends on the sensor specification and the working range [43]. For the triangulation sensor, as the distance increases toward the maximum sensing distance, the resolution progressively decreases.

Each sensor has different advantages and disadvantages. The triangulation sensor has a lower cost together with a fast measurement of tens or hundreds of kHz, but has certain limitations such as not working well on transparent objects and liquids [43][44].

***Optical microscopy***. Conventional optical microscopy or stereomicroscopy can be used for measuring surface topography based purely on image processing of the collected images as the object is scanned through focus so as to find the best focus at each point [1]. The advantages of this technique are a non-contact mode to test the surface and higher vertical range of measurement. The disadvantages are that they are limited to surfaces containing surface features and cannot be used on smooth surfaces, as well as being limited in axial resolution.

The two most common optical profilers are the confocal microscope and the white light interferometer. These generate measurements by sensing optimal focus and fringe visibility respectively, at the different points in an image.

***Confocal microscopy.*** The basic principle of the confocal microscope, illustrated in Figure 10 (a), is to illuminate only one spot on the sample at a time through a pinhole. The light reflected from the sample is imaged by the objective back to the pinhole. A complete image is then formed by scanning the spot over the sample. If the sample moves out of focus, as shown in Figure 10(b), the image will disappear because the reflected light is defocused at the pinhole and hence does not pass through it to a detector located on the other side [1].

A schematic illustration of another type of confocal microscopy which does not require vertical scanning is chromatic confocal microscopy, as shown in Figure 10(c) [1]. This technique uses an objective having axial chromatic aberration that has a different focusing position according to the height of the surface as a function of the wavelength. The wavelength value is detected by a spectrometer so that the spectrum measurement replaces the need for any mechanical scanning process. While the depth measurement process is fast [1][9], the disadvantages of the technique are the need for lateral scanning of the point measurement to build up an image and the optical sensitivity to inhomogeneous materials.

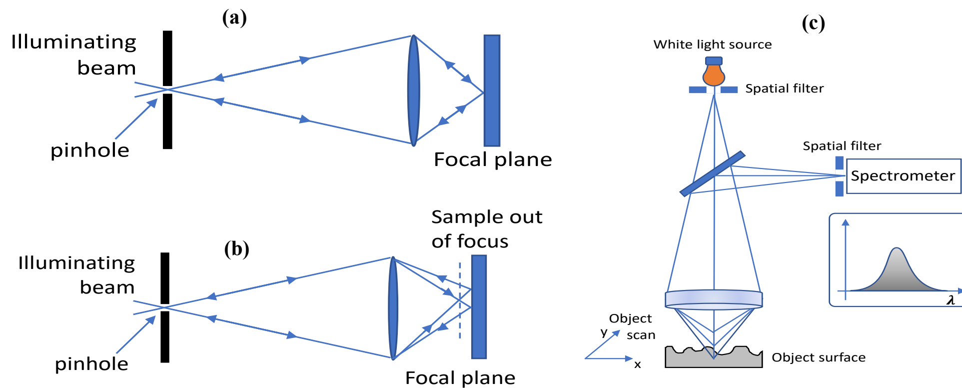


Figure 10. Simplified schematic of a confocal scanning optical microscope showing the sample (a) in the focal plane of the objective and (b) out of focus. (c) The schematic of chromatic confocal microscopy [1][9].

The resolution in chromatic confocal microscopy can be improved by illuminating the field point by point with an Airy diffraction spot and by using a small confocal exit pinhole [45].

***White Light Interferometer***. White light scanning interferometry (WLSI) optical profilers use a white light source that has a broadband visible spectrum with wavelengths from about 380 nm up to 750 nm (violet to red) and work like an optical focus sensor in which the maximum fringe visibility determines the position of the surface. The use of broadband illumination overcomes some of the limitations that are found in single and even multiple wavelength methods. The technique is therefore now known as CSI.

Several types of interference objectives that exist are the Michelson, Mirau and Linnik. The Mirau and Linnik configurations are both variations of the Michelson [1]. In general, the difference between them depends on the number of objectives used, the mechanical design and the way the beam is split into reference and object beams. The Linnik configuration is discussed in section 2.1 [46].

*Michelson setup*

In the Michelson setup, shown in Figure 12 (a), a single objective is used behind a beam splitter that splits the incident light into two beams by amplitude division. These two light beams, reflected by the sample and reference mirror, propagate along almost the same optical distance, and are recombined by the same beam splitter before passing again through the objective. The resulting interference patterns are generated by superimposition of these two light beams and can be visualized with occular or imaged on the camera. Thus, the height difference between the sample and reference mirror will contribute to the intensity map of these interference patterns. Because of the large beam

splitter in front of the objective, the Michelson setup is often used with low magnification objectives of between ×1 to ×10 magnification.

*Mirau setup*

The most commonly used interference objective is the Mirau setup, as shown in Figure 12 (b). This setup also uses a single objective, but with a semi-reflective window to divide the illuminating beam into two parts (reference beam and object beam). The reference mirror is positioned near to the entrance of the objective. The two beams are then recombined to form the interference fringe pattern on the camera target.

The advantages of the Mirau setup are the more compact design, the ease of adjustment, the robustness to mechanical influences and the reduced expense because of the fewer components used than in the Linnik design. However, in this setup, aberrations can occur in wide aperture systems due to the reference mirror placed between the objective and beam splitter. For this reason, this objective is often used in midrange magnifications from ×10 to ×40 magnification.

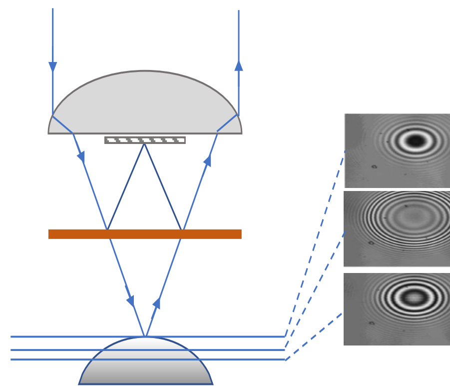

Figure 11. White light interferograms for a spherical object as obtained for a few positions of the objective during an axial scan [9].

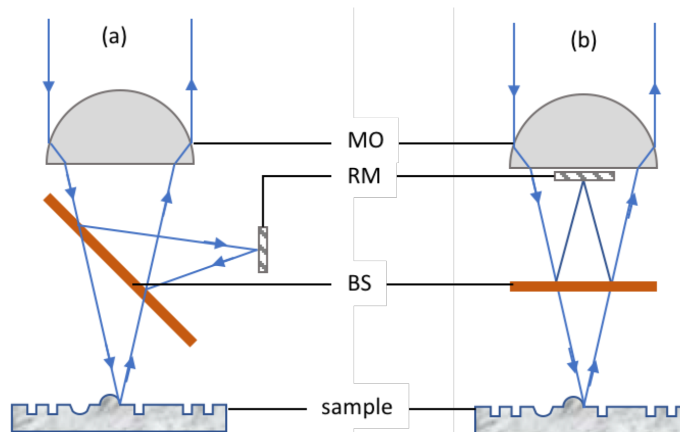


Figure 12. The objective setups of (a) Michelson and (b) Mirau: MO (microscope objective), RM (reference mirror), BS (beam splitter).

In order to obtain fringes at the best focus of the sample objective, the position of the reference mirror needs to be set at the best focus of the reference objective. In a Mirau objective, the two path lengths need to be first matched. Figure 11 shows a few interferograms as registered by the camera as the sample is progressively scanned through the focus of a Mirau objective. Fringes from individual interferograms show which part of the sample is in focus for a given position of the scan. The Mirau design is inherently more stable due to the use of a single objective [47] and is free from dispersion errors due to its symmetry and the same thickness of the plane-parallel plates [48].

*Immersion Mirau*

O.V. Lyulko et al. [49] developed an immersion Mirau system , known as SIMI, or Simultaneously Immersion Mirau Interferometry (shown in Figure 13) based on the principle of phase shifting interferometry (PSI) to simultaneously acquire all interferograms at the same time in order to eliminate the effects of vibration. To ensure identical optical paths in the object and reference arms, liquid is placed in the space between the reference mirror and the beam splitter. This system produces a sufficient image quality for performing experiments on live and fixed cells.

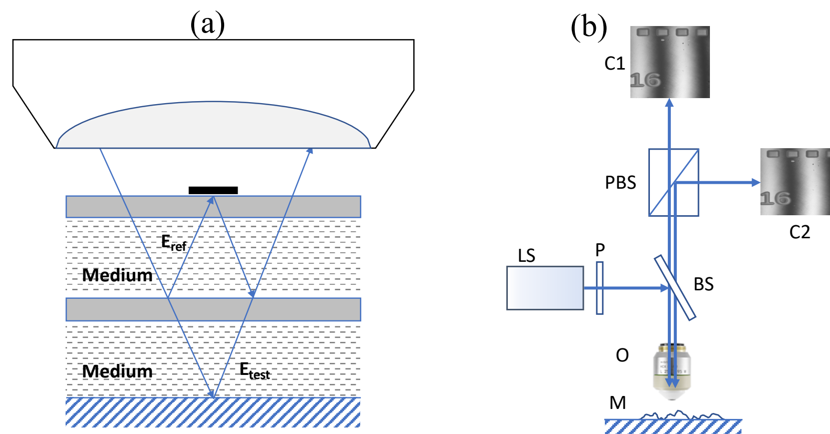


Figure 13. (a) IMI system (b) Layout of SIMI system with two-camera arrangement.

Linnik configuration (shown in Figure 22) will be explained in section 2.1 while the comparison of those configurations is presented in Table 2.

Table 2. Comparison of Michelson, Mirau, and Linnik configurations.

| | **Michelson** | **Mirau** | **Linnik** |
|---|---|---|---|
| **Magnification** | Low (1.5×, 2.5×, 5×) | Medium (10×, 20×, 50×) | High (up to 100×, 200×) |
| **Required objective** | 1 | 1 | 2 |
| **Adjustment** | easy | easy | difficult |
| **Working distance** | only long WD objective | limited | objective-dependent |

**Spectral Interferometry**. A variation of CSI is the spectral version [9]. This technique is based on the observation of interference fringes for a very large number of wavelengths using a spectrometer. Spectral interference can be obtained by using a source with a tunable wavelength (system of wavelength scanning interferometers) or by placing a dispersive element at the exit of the interferometer (system of spectrally resolved CSI). This method bypasses the need for mechanical axial scanning by detecting the fringe frequency which carries information about the object's position instead of detecting the best focus at each point on the camera.

**Digital holographic microscopy.** Holography is also based on the interference of light to create interference patterns. A hologram is created by dividing the illuminating laser light into two beams. One beam illuminates the sample (sample beam) and the other beam (reference beam) illuminates the recording medium or a camera target in the case of digital holographic microscopy (DHM). By either reflection or transmission, combining the light from the sample with that of the reference beam will result in an interference pattern, or a hologram. In DHM, the image creation process is performed using by a computer.

The principle of digital holographic microscopy is shown in Figure 14. A phase modulator can be added either in the path of the illumination beam or in that of the reference beam. The field diffracted in O' is superimposed coherently to the reference beam. The resulting interference pattern is recorded without lens L3 while adding it allows an image to be recorded in direct space [50].

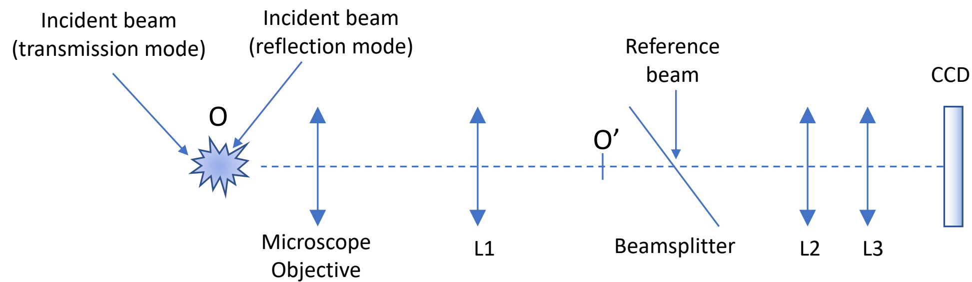

Figure 14. Principle of digital holographic microscopy [50].

While DHM has been used for characterizing biological specimens, it is being used increasingly in the metrology of materials.

### 1.1.3 Comparison of characteristic parameters of profilers

The advantage of imaging interferometric systems over most other optical and stylus profilers is their ability to scan the entire field rather than proceed by point scanning. Because the whole area is imaged at the same time, lateral scanning becomes unnecessary, which greatly speeds up the measurement process. Table 3 shows the comparison of the two groups of profilers.

The advantages (indicated by +) and disadvantages (indicated by -) of each technique compared with the others are as follows:

Optical profilers:

+ Larger field of view (FOV) than stylus profilers.

+ Higher lateral resolution than stylus profilers.

+ Higher speed measurement than stylus profilers and confocal microscopy due to axial scanning using full field imaging in CSI.

+ Non-contacting and non-invasive, making it possible to measure through transparent layers compared with stylus techniques.

- Sensitivity to optical errors.

Stylus profilers or AFM/STM:

+ Higher axial and lateral resolution than optical profilers.

+ Multiple modes available for detection of different parameters.

- Slow measurement speed for 3D profiling of surface due to point scanning [51]; not able to measure full-field dynamic motion.

- The possibility of stylus tip damage of delicate surfaces during the scanning process due to physical contact.

Table 3. Comparison the main characteristic parameters of stylus profiler, SPM, confocal microscope and white light interferometer [9].

| Parameters | AFM/STM | Stylus | WLI | Confocal |
|---|---|---|---|---|
| X,Y resolution | ++ | - | + | + |
| | (2-10 nm/0.1 nm) | (2-10 µm) stylus radius dependent | (0.5 µm; NA objective dependent) | (0.5 µm; NA objective and lateral sampling dependent) |
| Z resolution | ++ | + | + | - |
| | (0.1 nm/ 0.01 nm) | (0.25 nm) | (0.3 nm) | (1-20 nm; magnification dependent) |
| FOV (field of view) | - | ++ | + | + |
| | (up to 50×50 µm) | (up to 120×120 mm) | (100×100 µm to 10×10 mm, can be extended by stitching) | (100×100 µm to 10×10 mm, can be extended by increased lateral sampling obj) |
| Scanning | point by point | point by point | Full FOV | point by point |
| Measurable height range | -- | - | ++ | + |
| | (up to 3 µm) | (1 mm) | (8 mm or limited by working distance of obj) | (limited by working distance of objective) |
| Measurement time | -- | -- | ++ | + |
| | (hours to days) | (hours to days) | (seconds to minutes) | (several minutes) |
| Full field dynamic motion | x | x | v | x |
| Measure through the glass | x | x | v | v |
| Contact technique | optional | v | x | x |

Furthermore, the advantages or disadvantages of each profiling technique can be considered in terms of the physical limitations in the capabilities of providing 3D information according to the dominant noise sources and the relation of the physical measurement of the uncertainty scale with the aperture or working distance, as shown in Table 4 [8].

In general, in type I, sensors based on triangulation, i.e. confocal microscopy, chromatic confocal microscopy and SIM, measure the lateral shift of local details and the scaling factor depends on the dominant noise source [8].

In type 2 sensors, the result of the measurement uncertainty of CSI on a rough surface does not scale with the distance of the aperture of the observation, so benefitting from the possibility of measuring within deep holes or at a large distance without increasing the measurement uncertainty [8][52]. The inconvenience is the scanning time required to measure over several hundred micrometres or mm depth [53].

Table 4. Classification of 3D optical sensors [8].

| Type and principle | Dominant noise | Scaling behaviour |
|---|---|---|
| **Ia**<br>triangulation at rough surface | speckle noise | $\delta z \sim \lambda/(\sin u\, sin\theta)$<br>no z-averaging over the resolution cell |
| **Ib**<br>(triangulation at smooth surfaces and that with fluorescence) | photon noise | $\delta z \sim \lambda/sin^2 u$ |
| **II**<br>CSI at rough surface | surface roughness | $\delta z$ is independent from aperture, no z averaging |
| **III**<br>classical interferometry | photon noise | $\delta z \sim \sin u$ , due to z avreaging over the resolution cell |
| **IV**<br>deflectometry | photon noise | $\delta x \cdot \delta \alpha \sim \frac{\lambda}{Q}$<br>$\delta x = \lambda/\sin u$ |

# 1.2 Interference microscopy

The developments in interference methods applied to microscopy have rapidly grown since the first systems using Phase Stepping Interferometry (PSI) proposed in the 1980's and those based on coherence analysis in the 1990's [9][8][52][54]. The second method is known by several different terms:

WLSI: White Light Scanning Interferometry [55].

CCI: Coherence Correlation Interferometry.

CPM: Coherence Probe Microscopy.

CSM: Coherence Scanning Microscopy.

SWLI: Scanning White Light Interferometry.

VSI: Vertical Scanning Interferometry.

CSI: Coherence Scanning Interferometry.

Interferometry consists of the superposition of two waves with the same frequency, split into two parts and typically coming from a coherent light source (monochromatic). In white light interferometry, the interference takes place between the superposition between waves with the same frequency over the broad spectrum of the white light source. The waves travel in different paths and are combined to create interference. Each part of the wave with the same phase will add constructively, whilst those out of phase by 180° will destructively cancel each other, resulting in dark fringes. The illustrations are presented in Figure 15.

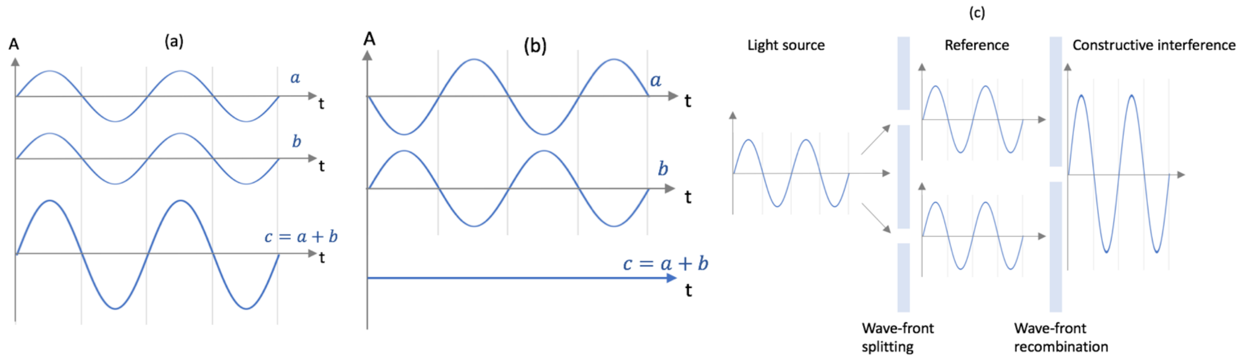


Figure 15. Superposition illustrations. (a) constructive interference, (b) destructive interference, (c) constructive interference from a coherent light source

Superposition has been described mathematically in many sources [56][52][57]. The optical wavefronts in superposition are plane waves. The amplitude of a plane wave at a position (x,y,z) and time (t) may be expressed as

$$E(x, y, z, t) = a\,cos(\omega t - kz) \qquad \text{(Eq. 4)}$$

or in a complex exponential as $E(x, y, z, t) = Re\{Ae^{\omega t}\}$

$$E(x, y, z, t) = Re\{a\,e^{-i\varphi + \omega t}\} \qquad \text{(Eq. 5)}$$

where a is the amplitude of the wave, $A = ae^{-i\varphi}$ is the complex amplitude, and $\varphi = 2\pi z/\lambda$. This complex amplitude at any point in the image plane is the sum of the complex amplitudes of the two interfering wavefronts ($A = A_1 + A_2$). Hence the intensity at any point is

$$I = |A|^2$$

$$I = |A_1|^2 + |A_2|^2 + A_1 A_2^* + A_1^* A_2$$

$$I = I_1 + I_2 + 2\sqrt{I_1 I_2}\,cos\Delta\varphi \qquad \text{(Eq. 6)}$$

$I_1$ and $I_2$ are the individual intensities of the two waves, and $\Delta\varphi = \varphi_1 - \varphi_2$ is the phase difference. The phase difference can be related to the optical path difference (OPD), assuming the two wavefronts use a common source,

$$OPD = \left(\frac{\lambda}{2\pi}\right)\Delta\varphi \qquad \text{(Eq. 7)}$$

The spectral range and size of the light source used in interferometry define the temporal and spatial coherence and the nature of the interference fringes. For example, with a point monochromatic light source, the spatial coherence is high, resulting in a long coherence length and a large number of fringes. With a white light source emitting

polychromatic light, because of the broad range of frequencies, the temporal coherence is low, resulting in a short coherence length a small packet of white light fringes.

There are two main techniques used in this work: Phase Shifting Microscopy (PSM) and CPM or CSI that will be described in this section. Each technique has its own main advantages, as presented in Table 5 in general terms. The advantages of CSI are that it is rapid, non-destructive and applicable to many different types of surfaces over a high dynamic range [58][59]. PSM enables the measurement of the height of nanometric surface irregularities [55], but only over a small measurement range ($<\lambda/2$). A very high axial resolution can be achieved in PSM provided proper adjustment of the instrument and a quiet environment. Otherwise errors can result in the measurement [60]. Therefore, the choice of the best algorithm of phase modulation plays an important role in the PSM performance.

Table 5. Comparison of using different techniques in interferometer.

| **Description** | **Techniques** | |
|---|---|---|
| | **PSM** | **CSI** |
| Light source | monochromatic | polychromatic |
| Measuring range | small | large |
| Accuracy of height range | less than 300 nm or better less than 200 nm | deeper height range |

## 1.2.1 Phase Shifting Microscopy

Introduction

PSM is a mathematical interpolation method of interference fringes based on the introduction of known phase shifts between the two arms of the interferometer, in order to determine the phase [59][61][62]. These phase shifts result in several interferograms that are recorded for different values of the optical path difference (OPD). Different ways of introducing the phase shift exist: by vertical translation of the sample, by translation of the interferometer or by the translation of the reference mirror to obtain different values of OPD that are typically equidistant fractions of the fringe spacing [63].

While the axial resolution of PSM is nanometric, the axial dynamic range is limited to several hundred nanometres due to the periodicity of the interference fringes. It is therefore well adapted for measuring surface roughness of very smooth surfaces and small defects. The lateral resolution is limited by diffraction to $\lambda/2$ (typically around 0.4 µm). Due to the limited axial range of PSM, CSI was developed in the 1990s to enable the measurement of much deeper surface roughness.

### Operating principle of PSM

In PSM, the sample is illuminated by a monochromatic or quasi monochromatic light source through an illumination system such as with Köhler illumination. Then three or more images are taken by the camera for different values of the OPD corresponding to sub-multiples of the wavelength. The phase of the wavefront reflected from the sample is calculated at each pixel in the image. The result of the calculations is then displayed as a synthetic image with grayscale encoding of the altitude, which represents the surface mapping.

The interference pattern or the intensity at a coordinate point (x, y) in an interference pattern may be expressed by the following Eq.8 [58]:

$$I_i(x,y) = I_o(x,y)[1 + \gamma_0 \cos(\varphi(x,y) + \alpha_i)] \qquad \text{(Eq.8)}$$

in which $\alpha_i$ is the phase shift introduced, $Io(x,y)$ is the square of the incident amplitude, $\gamma_0$ is the visibility factor of fringes and $\varphi(x,y)$ is the signal phase to calculate. An acquisition of at least three interferograms with controlled phase shifts is required to determine the three unknowns; $I_o(x, y)$, $\gamma_0$ and $\varphi(x,y)$. Higher numbers of interferograms can be used to improve the measurement precision.

There are two basic modes for introducing phase shifts, the discrete mode and continuous mode. The difference between these two modes is illustrated using the algorithm of 4 steps of 120° [58].

#### a. Discrete mode

If the phase difference is obtained from discrete phase steps, the technique is known as phase stepping microscopy. The graph in Figure 16 shows the variation of intensity of the interference fringes as a function of the phase shift in the discrete mode. After each step, the interferogram is recorded and four images are taken. The result of the calculations is displayed as a synthesised grayscale image of the phase:

$$\varphi = \tan\left[\frac{I_4 - I_2}{I_1 - I_3}\right] \qquad \text{(Eq.9)}$$

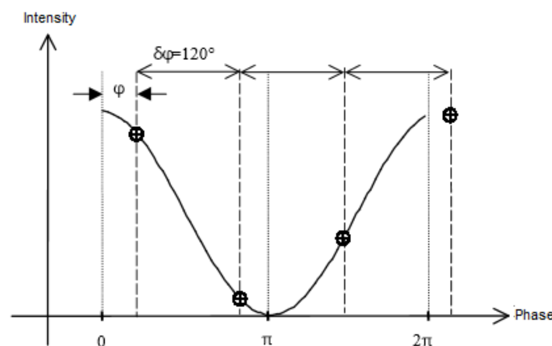


Figure 16. Phase determination, from 4 discrete steps of 120° [58].

b. Continuous mode

The technique of phase change in the continuous mode (Phase Shifting Microscopy), also called the technique of phase integration, is characterized by a linear variation of phase (Figure 17). The change of phase is performed during the period T and the acquisition of an image is made during a time τ which depends on the number of images taken.

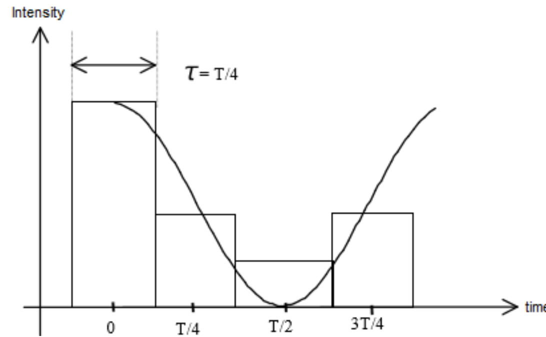


Figure 17.The technique of the change of phase [58].

Assuming that the period T of the signal is continuous, the initial phase difference between the two beams can be determined (as in the discrete mode) by recording several interferograms over the period T (one interferogram for each integration time τ). If we consider the example of Figure 17, four images are recorded respectively during the integration time $\tau_1 = 0\,, \tau_2 = \frac{T}{4}\,, \tau_3 = \frac{T}{2}\,, \tau_4 = \frac{3T}{4}$.

## 1.2.2 CSI method

As mentioned previously, CSI is a non-destructive optical profiling technique based on light white light interferometry that is well suited for measuring the 3D structures of sample depths over a few µm to tens of µm. CSI uses the interference fringes of white light in a simple way. Instead of calculating the phase using image processing (like in PSM), its strong point is the use of the fringe envelope as a virtual probe. The advantage of this technique compared to PSM is the depth of the larger vertical field and the ability to measure height differences over many µm. A wide range of measurement, high accuracy, and short time of measurement are some of the advantages of this technique [55] so that it is widely employed in many applications e.g. analysis of structures of polymers in material sciences and engineering, measurement of surface topography and machine parts in mechanical engineering, measurement of silicon wafers in microelectronics, analysis of MEMS and MOEMS and the measurement of optical and micro-optical components and elements, etc.

### 1.2.2.1 General principle of CSI

The camera measures the intensity of the light as the distance between the interferometric objective and the sample that changes along the z axis, so scanning the fringes over the depth of the sample surface. The goal is to find the maximum fringe contrast which corresponds to the peak of the fringe envelope. The intensity of the light is measured by each pixel sensor and the fringe envelope is then obtained and used to calculate the position of the surface. Figure 18 shows how the interference is built up at each pixel in the camera array.

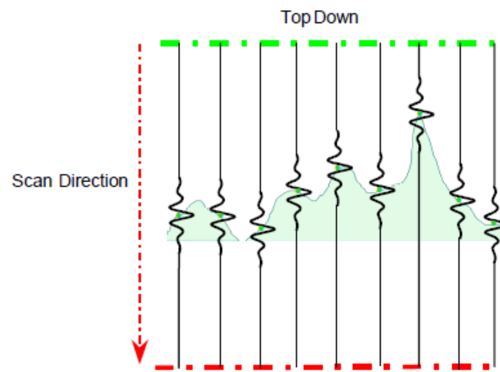


Figure 18. An interferogram on a surface using CSI.

White light is used rather than monochromatic light because it has a shorter coherence length, so avoiding ambiguity in determining the fringe order. The accuracy and repeatability of the CSI measurement depend on many parameters including the stability of the sample, the environment, the performance of the camera, the control and linearity of the vertical actuator, the design of the metrology frame, etc.

### 1.2.2.2 Signal processing in CSI

Fringe signal

The light intensity giving rise to the fringe signal, s(x,y,z), obtained from a detector (digital camera) as the OPD is varied through focus in a white light interferometer, has the following form [56] in Eq.10.

(Eq.10)

The function s corresponds to the intensity signal at a given point of the sample surface (x,y), where z represents a vertical scanning position along the optical axis in relation to the surface. The quantity a(x,y,z) is an offset intensity related to the reference and object beam intensities, b(x,y) is the fringe contrast, g(z) is the fringe envelope function related to the spectral profile of the white light source, and $\lambda_0$ is the mean wavelength of the light source. The phase offset related to the phase change on reflection represented by α(x,y).

Many different algorithms exist for extracting the fringe envelope such as demodulation [64][65], peak fringe scanning microscopy (PFSM) [57][66], Fast Fourier Transform (FFT) [60], wavelets [67] and signal correlation [68]. The techniques used in this work are now described.

### Z-scan technique (1D)

Figure 19 shows how a stack of fringes are acquired for analysis in CSI by means of a single vertical scan of the fringes over the depth of the sample. Signal processing is then used to find the fringe envelope and finally the peak of the envelope that corresponds to the position of the surface. The Z-scan technique developed in the IPP team [4] uses 2D image processing of the XZ images from the XYZ image stack to obtain the fringe envelopes along Z. The technique is based on demodulation and allows the determination of the positions of the peaks of the fringe envelope which corresponds to the height of the surfaces at each pixel in the XY image.

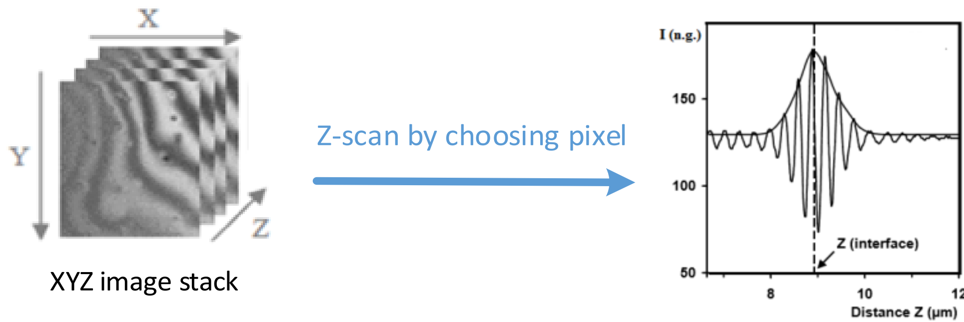


Figure 19. Z-scan technique.

The advantage of this technique is that the XYZ matrix can be manipulated and processed for use in the study of more complex transparent layers, similar to the FF-OCT technique [69].

### FSA fringe envelope algorithm

An efficient and well known algorithm for detecting the fringe envelope is the Five Step Adaptive (FSA) algorithm proposed by Larkin [56] which calculates the fringe visibility at each pixel. This method detects the envelope of the fringe signal using five sampling positions along the optical axis for each point. Eq.4 shows the formula of the calculated envelope. The FSA algorithm requires the values of $\phi$ close to 90° for accurate measurement, as given in Eq.12.

$$4A^2 sin^4\varphi = (I_2 - I_4)^2 - (I_1 - I_3)(I_3 - I_5) \quad \text{(Eq.11)}$$

$$A^2 = \frac{1}{4}[(I_2 - I_4)^2 - (I_1 - I_3)(I_3 - I_5)] \quad \text{(Eq.12)}$$

where A is the amplitude value at the sampling position; $\phi$ is the phase shift due to the scanning step; $I_3$ is the local position and; $I_1$, $I_2$, $I_4$, $I_5$ are the neighboring sampling

positions. The amplitude value of the envelope A can thus be calculated by means of only two multiplications and one square root operation that gives an advantage in terms of the time required for computation compared with other more involved algorithms when implemented in software processing.

# 1.3 Resolution

As with any measuring instrument, resolution criteria are required in interference microscopy in order to know the smallest details observable of a measured structure and to correctly analyze the unknown surface. Hence, there are several different criteria of resolution [70]: two-point resolution, resolution based on the point spread function (PSF), Fourier theorem based resolution and other resolution criteria such as resolution based on the Nyquist theorem, the observation volume, and size.

In considering optical profiling, it is important to take into consideration the limits of resolution which will define the smallest details measurable or the ability of a microscope system to discriminate the constituent parts of an object as being separate in space (spatial) and as being separate in events (temporal). The higher the resolution, the smaller the point difference to distinguish.

In this section, we will focus on the spatial resolution which is commonly further sub-categorized into lateral resolution and axial resolution. These are now presented.

## 1.3.1 Lateral Resolution

A minimum distance between two points in the object plane that are considered to be resolved in the image is a useful definition of the lateral resolution for lateral measurements in a classical imaging (2D) microscope. However, this definition becomes impractical for areal surface topography measurements because the distance between two adjacent points could affect their relative height difference. Use of ISO 25178-601 2010 [8], the width limit for full height transmission, solves the problem of the lateral resolution definition although it is still under debate [71] since it is not appropriate for certain applications. The experimental test using a grating with a period close to the resolution of the instrument is carried out to measure the width limit.

***2D Lateral Resolution***

Two-point resolution, one of the resolution criteria, has various criteria to resolve two points on the object separated by a minimal distance [72]. The ability of an optical system to resolve two nearby point sources of light with equal brightness is referred to by the Rayleigh criterion. These point sources are represented by two well separated diffraction patterns, or Airy disks. The better two-point resolution is obtained by a smaller diameter and smaller detectable distance. This resolution criterion is based on

the full width at half maximum (FWHM) of the point spread function [70]. The PSF is a diffraction pattern of the system's effective aperture. The two-point resolution is the ability of an imaging system by eye or an optical instrument to distinguish two-point sources of equal luminosity and separated by a minimum distance. The criteria of Abbe, Rayleigh, and Sparrow are the two-point resolution criteria which are based on the observation of PSF recovery.

In 1873, the German physicist Ernst Abbe found that the resolution of an optical imaging instrument is not only constrained by the quality of the instrument, but by the wavelength of light used and the aperture or numerical aperture (NA) of its optic or imaging lens. This meant that in the absence of aberrations, lateral resolution is fundamentally limited by the diffraction of light so that two objects located closer than $\lambda/(2NA)$ cannot be resolved. This resolution corresponds to the spatial cutoff frequency of the optical system when it is considered as a linear filter. This is usually the case when the numerical aperture of the lens is low and the illumination is totally coherent or incoherent. Hence the resolving properties are uniquely determined by the impulse response of the system [73][74][75].

Then in 1986 Rayleigh defined his criterion, in which two points are resolved if the center of the spot of the first source point coincides with the position of the first zero of the spot of the other diffracted source point [76]. He stated that for incoherent illumination, two-point images of equal brightness separated by a distance of the Airy disk will be resolved. But the optical aberrations degrade the optical resolution of the imaging system [70].

The difference between the Abbe and Rayleigh criteria is based on the definition of two objects being resolvable from each other. In practical applications, this difference is small. The Rayleigh definition is stated in the form that two points of equal brightness can be distinguished if there is a 26.5% dip in intensity between them. This definition corresponds to the two incoherently illuminated points being separated by a distance $r_R$ (Rayleigh) [4].

While the Sparrow criterion modifies the Rayleigh criterion and defines that the two-point resolution is the smallest distance between two points at which the minimum in the intensity distribution of the combined two luminous points vanishes [70].

The Sparrow criterion is defined by the separation for which the resulting intensity pattern has no curvature in the centre [1]. Approaching the definition of resolution from a different angle, the Abbe resolution limit is the largest diffraction grating pitch that cannot be detected by the optical system. The Rayleigh and Sparrow definitions correspond to objects that are Dirac distributions in the object plane while the Abbe definition corresponds to objects that are Dirac distributions in the spatial frequency domain.

The Rayleigh criterion defines the resolution mathematically given by Eq.8. presents the definition of lateral resolution of an optical system based on the illumination type [77], where $\lambda$ is the wavelength of the light source, n is the index of the medium between the objective lens and the sample and $\alpha$ is the half angle of the lens aperture. The value of ($n \sin\alpha$) is the numerical aperture of the optical lens [78]. Other criteria based on the illmunitation type are presented in Table 6.

Table 6. The lateral resolution criteria based on the illumination type.

| Criteria | Illumination type | |
|---|---|---|
| | Incoherent | Coherent |
| Rayleigh | 0.61 $\lambda$/NA | - |
| Sparrow | 0.47 $\lambda$/NA | 0.73 $\lambda$/NA |
| Abbe | 0.5 $\lambda$/NA | $\lambda$/NA |

Numerical aperture as applied to a microscope objective is a measure of the ability to gather light and resolve fine specimen detail at a fixed object distance. NA determines the resolving power of an objective, but the total resolution of a microscope system is also dependent upon the numerical aperture of the sub-stage condenser (in transmission microscopy). The higher the numerical aperture of the total system, the better the resolution.

The diffraction-limited phenomenon hindered the performance of optical microscopy for over a century, and was considered a fundamental, unbreakable rule. The quality of the resolution measurements is obtained from caution in designing the resolution artefacts. For example, the aspect ratio of a square shaped grating will influence the value of the resolution as well as other errors such as the batwing effect [79] that could increase the apparent height of the profile. However, several approaches in imaging have emerged, using super-resolution imaging techniques that operate beyond the diffraction limit [75]. Super-resolution microscopy is a collective name for a number of techniques that achieve resolution below the conventional resolution limit. Several advantages of imaging exist when it is not limited by diffraction.

***3D Lateral Resolution***

3D resolution is even more difficult to define and determine than 2D. In general, the resolution is determined in 2D. The applicability of conventional concepts of the calculation of the resolution are in debate when applying them to the quantitative measurement in three dimensions [80] so the definitions of Rayleigh and Sparrow are not directly applicable when measuring surface topography.

The PSF in the three spatial directions ($FWHM_x$, $FWHM_y$, $FWHM_z$) can be used to describe the 3D resolution power of a microscope system. For different systems, it may be difficult to do a comparison, so Hell and Stelzer [81] proposed using an additional

criterion of the observation volume ($V_{obs}$), in which it is defined as the volume enclosed by an iso-surface of the 3D-PSF, i.e. the ellipsoid volume [82] formed by the three FWHMs: $V_{obs} = \frac{4}{3}\frac{FWHM_x}{2}\frac{FWHM_y}{2}\frac{FWHM_z}{2} = \frac{4}{6}FWHM_xFWHM_yFWHM_z$.

Another way to determine the resolution of high performance microscopes is by using measurement of the three-dimensional point–spread function (3D-PSF) which is standardized by recording the scattered light of point like objects [83]. The precision of the 3D-PSF and 3D imaging have become possible for the highest NA due to the 3D-piezoelectric scanner.

### 1.3.2 Axial Resolution

Axial resolution refers to how details in the object appear in the image when perfect focus is not obeyed. On the object side, this affects how well 3D objects are imaged. The axial range in object space over which appreciable sharpness is met in the image is known as the depth of field. Pluta [54] shows that the diffraction limit of the depth of field can be given by Eq.14.

The image that is formed in the intermediate image plane by the objective lens is a diffraction image with a finite spread, or known as Fraunhofer diffraction, as shown in Figure 20. It is not an infinitely small point. This pattern is formed by the exit pupil of the objective lens where the spherical waves converge to the focal point. The Airy disk is the central bright disk in the diffraction image, which is the image of a point source of light in an aberration-free optical system. Its radius is from the central peak to the first minimum of the diffraction image given as $\left(r_{Airy} = \frac{0.61\lambda}{NA}\right)$, where λ is the vacuum wavelength of the light.

Figure 20. A circular aperture of Airy pattern in central Airy disk.

In correspondence to the lateral resolution limit [45], the Rayleigh criterion (in Eq.14), which is taken from the Airy disk radius, $z_{min}$ (Eq.15) is used for measuring the axial resolution, in which the ratio of the lateral to axial resolution $\left({z_{min}}/{r_{Airy}} = {3{,}28n}/{NA}\right)$ is inversely proportional to the NA of the objective.

$$z_{min} = \frac{2\lambda n}{NA^2} \quad \text{(Eq. 15)}$$

In CSI, as well as FF-OCT, the mechanism governing the axial resolution is independent of the classical depth of field and may be determined by the coherence length of the illumination source. The axial resolution is defined as the FWHM Δz of the interferogram that is equal to half the coherence length. Eq.16 is an expression of the axial resolution by assuming the spectrum to be Gaussian shaped, where n is the refractive index of the medium, λ is the center wavelength, and Δλ is the spectrum width (FWHM) as shown in Figure 21.

$$2\delta z = \frac{n\lambda}{NA^2} \quad \text{(Eq.16)}$$

$$\Delta z = \frac{2\ln 2}{n\pi}\left(\frac{\lambda^2}{\Delta\lambda}\right) \quad \text{(Eq.17)}$$

$$\text{FWHM} = 2\sigma\sqrt{2\ln 2} = 2.35\sigma \quad \text{(Eq. 18)}$$

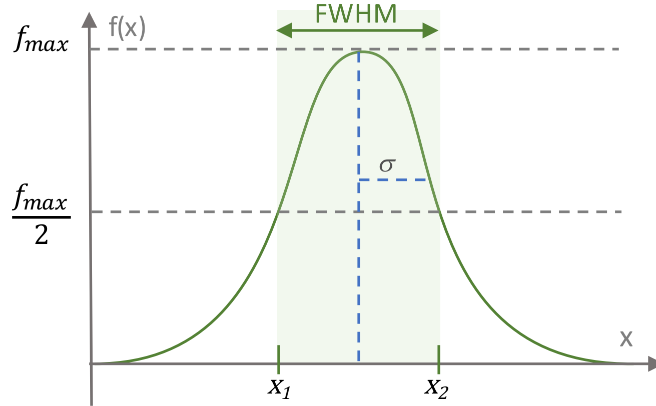


Figure 21. Illustration of a full width at height maximum and the relation with the standard deviation, σ.

## 1.4 Conclusion

In this chapter we have looked descriptions of two main profilometers: contact profilometers and optical profilometers to profile the surface topography in 2D and 3D. There are several techniques with different parameters for both types of profilometers. The advantages and disadvantages of each techniques have been presented including the application field. Continued by presenting the comparison of all techniques in several ways in the next section.

First, the contact profilometers are the stylus profiler and the near field probe microscope, which use a touch probe to measure the surface profile. Their measurement performance differs in terms of resolution and lateral and vertical reach, and for

different applications. Stylus profilers are the oldest techniques used to measure surface roughness by moving the surface of the object under the tip of the stylus or by moving a probe tip-shaped on the surface and detecting variations in height of the tip of the point. Near-field scanning probe microscopy was first developed on the basis of vacuum tunneling and has an unprecedented resolution in real space at the atomic scale.

The stylus profiler has become a standard in the industry, with many ISO standards developed, the technique has several disadvantages such as a relatively low scanning speed that can lead to a thermal increase of the sample and a lack of lateral resolution due to the geometry of the tip.

Second, the optical profilers that has several types existed. Rather than using a mechanical probe, an optical probe can be scanned laterally over an area to measure the height of the surface or an imaging probe can be scanned over the depth to map surface topography over a large area. Optical probes have the advantage of not being in contact with the surface of the sample.

The two most common optical profilers are the confocal microscope and the white light interferometer. These generate measurements by respectively detecting the optimal focus and visibility of the fringes, at different points of an image.

The basic principle of the confocal microscope is to illuminate a single point of the sample at a time through a pinhole. Instead of calculating the phase using image processing (as in PSM), its strong point is the use of the fringe envelope as a virtual probe. To improve the resolution of this microscopy, we proceed by illuminating the field point by point with an Airy diffraction point and by using a small confocal exit hole.

On the other hand, white light interferometry (WLSI) optical profilers use a white light source with a broadband visible spectrum with wavelengths from 380 nm to 750 nm (purple to red) and function as a optical focusing to measure the position of the surface. The use of broadband lighting overcomes some of the limitations found in single and even multiple wavelength methods. The technique is now known as CSI. Several types of interference objectives exist: Michelson, Mirau and Linnik.

The advantage of imaging interferometric systems compared to most other optical profilometers and stylus is their ability to scan the entire field rather than performing spot scanning. Because the entire area is imaged at the same time, side scanning becomes unnecessary, which greatly speeds up the measurement process.

Interference microscopy is the technique developed in this research project. Two main techniques are used in this work: phase-jump microscopy (PSM) and CPM or CSI. PSM is a method of mathematical interpolation of interference fringes based on the introduction of known phase shifts between the two arms of the interferometer, in order to determine the phase. These phase shifts result in several interferograms that are

recorded for different values of the optical path difference (OPD). The CSI, on the other hand, is a non-destructive optical profiling technique based on white light interferometry with a broadband light source. It is well suited for measuring 3D structures of sample depths from a few µm to several tens of µm.

When considering optical profilometry, it is important to consider the resolution limits that define the smallest measurable details or the ability of a microscope system to distinguish the component parts of an object separately in (space) space. and in time (temporal). The higher the resolution, the smaller the difference in point to distinguish. There are many criteria for determining the resolution. In this work, we use the Rayleigh criterion to determine the lateral resolution and the axial resolution is defined as the FWHM $\Delta z$ of the interferogram which is equal to half the length of coherence.

## 1.4 Résumé de chapitre 1

Il existe plusieurs méthodes d'instruments pour mesurer la rugosité de surface et les structures de surface en 3D. Les systèmes de profilométrie présentés dans ce chapitre sont des systèmes de contact par pointe et des systèmes sans contact par moyens optiques. Différentes techniques et configurations, pour les deux types de mesure, sont présentées et comparées dans cette étude bibliographique.

Les deux principaux profilomètres de contact sont le profileur à stylet et le microscope à sonde de champ proche, qui utilisent une sonde tactile pour mesurer le profil de surface. Leurs performances de mesure diffèrent en termes de résolution, de portée latérale et verticale et selon les différentes applications. Les profilomètres à stylet sont les techniques les plus anciennes utilisées pour mesurer la rugosité de surface en déplaçant la surface de l'objet sous la pointe du stylet ou en déplaçant une sonde en forme de pointe sur la surface tout en détectant les variations de hauteur de la pointe. La microscopie à sonde à balayage en champ proche a d'abord été développée sur la base de l'effet tunnel sous vide et a une résolution sans précédent à l'échelle atomique.

Dans le profilomètre à stylet, le rayon de la pointe du stylet, la forme de la surface et l'intervalle d'échantillonnage entre les points de données, sont les paramètres importants pour déterminer la résolution latérale. Plus le rayon de la pointe est petit et net, mieux sera le suivi de la forme de la surface à analyser. Mais d'autres facteurs tels que la force locale sur la surface et l'élasticité de surface doivent être pris en compte pour obtenir un résultat précis. En microscopie à force atomique, le choix d'un cantilever avec un embout approprié est une exigence pour obtenir une très haute résolution verticale et latérale.

Le profileur à stylet est devenu un standard dans l'industrie, avec de nombreuses normes ISO développées. Cette technique présente cependant plusieurs inconvénients tels qu'une vitesse de balayage relativement faible pouvant conduire à une augmentation

thermique de l'échantillon et un manque de résolution latérale due à la géométrie de la pointe.

Plusieurs types de profilomètres optiques existent. Plutôt que d'utiliser une sonde mécanique, une sonde optique peut balayer latéralement une zone pour mesurer la hauteur de la surface ou une sonde optique plane peut balayer la profondeur de l'échantillon pour cartographier la topographie de la surface. Les sondes optiques ont l'avantage de ne pas être en contact avec la surface de l'échantillon.

Un capteur de mesure de distance optique permet généralement la mesure des distances ou des longueurs absolues en un seul point à l'aide d'un détecteur optoélectronique et de techniques spécifiques de traitement du signal. Il peut être utilisé dans des applications d'automatisation telles que l'assemblage, l'inspection et les applications militaires. La résolution de distance de chaque système dépend de la spécificité du capteur et de la plage de travail.

L'avantage des systèmes interférométriques, objet du présent travail, par rapport à la plupart des profilomètres optiques et à stylet est leur capacité à balayer le champ entier plutôt que de procéder par balayage point par point. L'imagerie AFM souffre d'un manque de vitesse de mesure. Par exemple, la forme d'une pointe idéale présente un rapport d'aspect élevé par rapport à la forme de la surface d'un échantillon afin de donner une meilleure résolution, ce qui nécessite un temps de mesure plus élevé afin de ne pas abimer la pointe. Au contraire, le profilomètre optique par imagerie est plus rapide que l'AFM, mais présente une résolution latérale plus faible inhérent au système optique.

Les deux profilomètres optiques les plus courants sont le microscope confocal et la microscopie interférométrique en lumière blanche. Ils sont basés respectivement sur la mise au point optimale et la visibilité des franges, aux différents points d'une image de l'échantillon.

Le principe de base du microscope confocal est d'éclairer un seul point de l'échantillon à la fois à travers un trou d'épingle. Au lieu de calculer la phase en utilisant le traitement d'image (comme dans la PSM), son point fort est l'utilisation de l'enveloppe de franges comme une sonde virtuelle. Pour améliorer la résolution de cette microscopie, on procède en éclairant le champ point par point en utilisant un petit trou de sortie confocal.

Les profileurs optiques à interférométrie à lumière blanche (WLSI) utilisent une source de lumière blanche avec un spectre visible à large bande de longueurs d'onde allant de 380 nm à 750 nm (violet à rouge) et fonctionnent comme un capteur de focalisation optique pour mesurer la position de la surface. L'utilisation de l'éclairage à large bande outrepasse certaines limitations qu'on trouve dans les systèmes monochromatiques ou quasi monochromatiques. La technique est connue sous le nom d'interférométrie à

balayage cohérente (CSI). Plusieurs types d'objectifs ou d’architectures d'interféromètre existent : Michelson, Mirau et Linnik.

L'avantage des systèmes interférométriques par rapport à la plupart des autres profilomètres optiques ou à stylet est leur capacité à balayer le champ entier plutôt que de procéder par balayage pixel à pixel. Toute la zone étant imagée en même temps, le balayage latéral devient inutile, ce qui accélère considérablement le processus de mesure.

La microscopie d'interférentielle est la technique développée dans ce projet de recherche. Deux techniques principales sont utilisées dans ce travail : la microscopie à saut de phase (PSM) et CPM ou CSI. La PSM est une méthode d'interpolation mathématique de franges d'interférence basée sur l'introduction de déphasages connus entre les deux bras de l'interféromètre, afin de déterminer la phase. Ces déphasages résultent de plusieurs interférogrammes qui sont enregistrés pour différentes valeurs de chemin optique (OPD). La CSI par contre est une technique de profilométrie optique basée sur l'interférométrie en lumière blanche avec une source lumineuse à large bande. Il est bien adapté pour mesurer les structures 3D de profondeurs d'échantillons de quelques µm à plusieurs dizaines de µm.

En considérant la profilométrie optique, il est important de prendre en considération les limites de résolution qui définissent les plus petits détails mesurables ou la capacité d'un système de microscope à distinguer les parties constitutives d'un objet séparément dans l'espace (spatial) et dans le temps (temporel). Il existe de nombreux critères pour déterminer la résolution. Dans ce travail, nous utilisons le critère de Rayleigh pour déterminer la résolution latérale et la résolution axiale est définie comme la FWHM $\Delta z$ de l'interférogramme égale à la moitié de la longueur de cohérence.

# CHAPTER 2

# OPTIMIZATION OF A LINNIK MICROSCOPE

Having considered the different profilometers in the first chapter and the notions of resolution, now we present a specific type of interference microscope based on the Linnik design. As mentioned previously, in a Mirau objective, the two path lengths are matched (see section 2.1). Because there are two separate objectives used in the Linnik design, a more complex optical setup is required in order to match the two optical paths.

# 2.1 Linnik Setup

A Linnik setup requires two matched objectives for the two arms of the interferometer, with each one being directly in front of the sample and reference mirror respectively, together with a beam splitting cube (Figure 22). In this setup, because no component is required between the objective and sample, higher magnification objectives can be used, typically from ×50 to ×200, although lower magnifications can also be used. One requirement is that the optical path lengths of the two arms need to be equal, thus necessitating separate adjustment of the optical path length difference and focusing of the reference mirror and sample, which are not easy [84][85][7]. Its sensitivity to mechanical influences is another reason why it is rarely used and thus it is rather limited in commercial use [85][73]. However, there are several advantages of using the Linnik setup, including [84][86]:

a. Optical path lengths and focusing in both arms can be adjusted independently.
b. High magnification objectives can be used (50×, 100×, 200×).
c. Immersion objectives can be used.
d. Higher-NA objectives can be used to improve the spatial resolution.
e. Extra optical components can be easily inserted in both the object and reference arms of the interferometer, such as wave plates together with a polarizing beam splitter to work in polarised light.

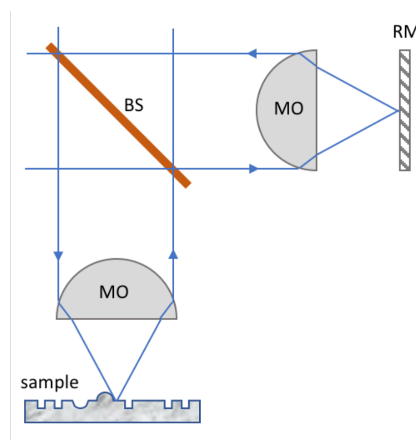


Figure 22. Linnik configuration in air.

The illumination beam, in the Linnik setup, is split into two by the beam splitter and the reflected beams from the sample and reference mirror are recombined and detected by the detector (the camera). The two images are hence superimposed on the camera target. The configuration can be used in the imaging mode by blocking the path of the light in the reference arm.

In simple terms, matching the two arms in a Linnik interferometer requires three steps: firstly, the reference arm is blocked, secondly, the objective is focused on the object with some features like the edge of a sharp but not too tall step (fringes are not visible at this moment) and thirdly, the reference mirror is brought into focus. Then the OPD between the two arms is changed in order to find the best contrast fringes which occurs at zero OPD. As the objective (or the sample) is scanned axially through focus, each pixel on the camera registers the irradiance; the highest point on the fringe envelope determines the best focus position on the sample.

***Immersion Linnik setup***

Immersion objectives can be used in order to allow the measurement of the sample in a liquid medium, and so increase the lateral resolution of the microscope due to the higher numerical aperture resulting from the water (or other liquid such as oil) which has a higher refractive index than air. An ideal configuration of a Linnik water-immersion head is shown in Figure 23. Water immersion objectives are used to minimize dispersion mismatch in the interferometer arms for depth scanning in transparent samples and to reduce light reflection from the sample surface [7][78].

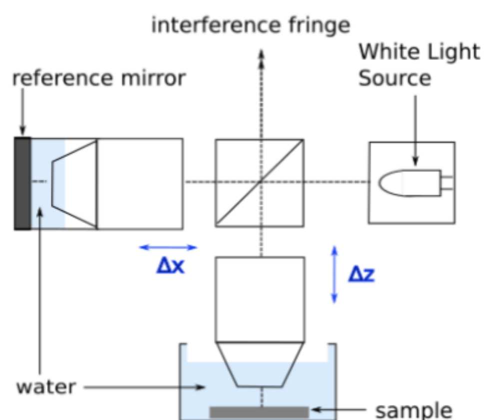


Figure 23. Configuration of a Linnik water-immersion objective.

## 2.2 Linnik designs

The Linnik setup is used less than the other interferometer objective configurations such as the Mirau and Michelson. This is mainly due to the difficulties in optimizing the design and in the adjustment of the configuration. In the literature search, it was not

easy to actually find many designs that have been published. Several Linnik configurations in air as well as those using water immersion objectives were finally found and these are now presented in order to show the different designs developed.

### 1. Linnik for FF-OCT analysis of tissue

The Linnik design proposed by A. Dubois et al. [84][7][86] (Figure 24) is for use in FF-OCT imaging in living tissue. The imaging method adapts an interference microscope to perform OCT using whole images instead of point scanning using the traditional point scanning fibre based OCT. Higher resolutions approaching 1 µm can be attained in FF-OCT compared with OCT [87]. The light source used is a near infrared light emitting diode (LED) with a center emission wavelength of 840 nm, a coherence length of 20 µm, and 40 mW of output power. This source was chosen to meet several requirements:

(i) The short coherence length reduces the width of the interferogram, which enhances background rejection for imaging inside a scattering medium, as in conventional OCT.
(ii) The spatial incoherence minimizes speckle formation in the images.
(iii) NIR emission (840 nm) reduces light scattering in biological tissue.
(iv) The LED can be switched on and off at a high frequency of 50 kHz for stroboscopic illumination.

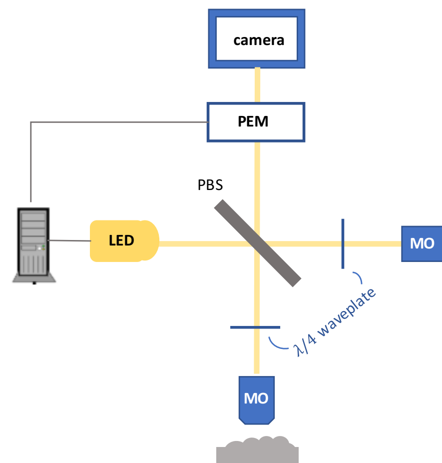


Figure 24. Experimental setup of a Linnik for FF-OCT imaging in living tissue [84].

The use of a polarizing beam splitter (PBS) is to split light into reflected s-polarized and transmitted p-polarized beams. It provides the advantage of the simplicity of intensity balance to overcome the problem of the different reflectivities of the optical surfaces [88]. Moreover the PBS minimizes the loss of light using a polarized beam, allowing a lower intensity source [48].

Other designs for tissue imaging are shown in Figure 25 (a) showing a vertically mounted reference arm and (b) a horizontally mounted reference arm [7][86]. This allows achieving a higher 3D spatial resolution of 1.8 µm × 0.9 µm (transverse × axial)

by means of the extremely short coherence length of the source, the compensation of dispersion mismatch in the interferometer arms, and the use of relatively high-NA microscope objectives.

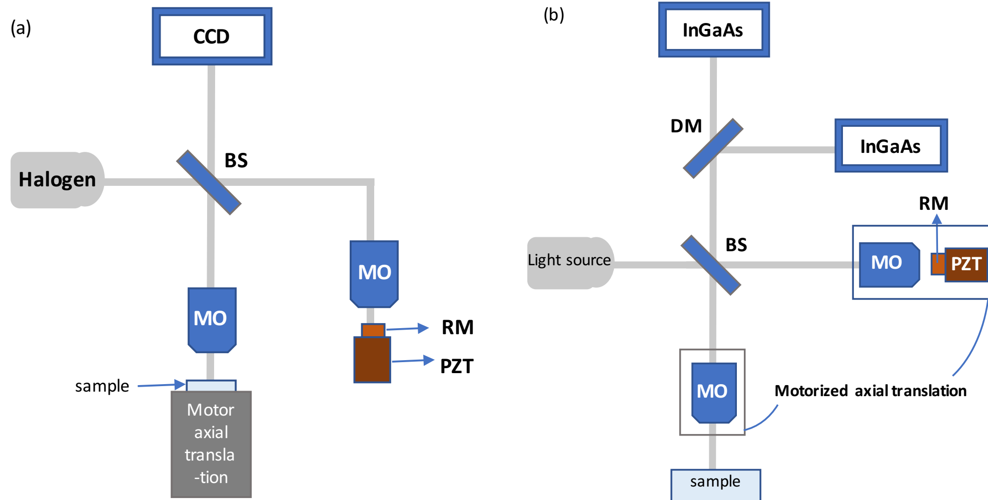


Figure 25. Schematic of (a) the ultrahigh-resolution full-field OCT setup [7] and (b) the experimental setup of FF-OCM [86]. MO, microscope objective; BS, beam-splitter cube; DM, dichroic mirror; PZT, piezoelectric actuator.

In the schematic of Figure 25 (b), water immersion microscope objectives (Olympus, 10x, NA 0.3) are used, with the reference objective being held in a reservoir of water to minimize dispersion mismatch in the interferometer arms with the imaging depth in the sample, and to reduce light reflection from the sample surface.

## 2. High precision Linnik in air

The Linnik design proposed by P. Lehman et al. [85] in Figure 26(a) is a high precision system for high resolution measurement of samples in air. Due to the fact that the interference takes place behind the objectives then dispersion effects have to be minimized. Thus, the beam splitter cube has a high planarity and low dimensional and angular tolerance. The optical path lengths in the glass in both arms of the interferometer are nearly the same. The mechanical setup provides a number of adjustment axes, with high tolerance as shown in Figure 26.

Both objectives have to be placed exactly on the optical axes. Even small tilt angles would lead to significant dispersion effects in the measuring results. Then the object and the reference mirror have to be placed exactly at the Working Distance (WD) given by the focal length of the objective. The axial Objective Lens Distance (OLD), i.e. the distance between the microscope objectives and the center of the beam splitter is important as well.

The WD, one of the considered factors of microscope objectives, is the actual distance between the objective front lens and the surface of the cover glass when the specimen is in sharp focus When the objective is moved closer to the sample, the focal plane moves further into the specimen. However, this is physically limited by the fact that the objective can only be moved until it is in contact with the cover glass. There is an inverse relationship between working distances and the magnification of each objective. For example, a 10x objective may have a working distance of 4 mm, whereas the working distance of a 100x oil objective will typically be in the region of 130 µm.

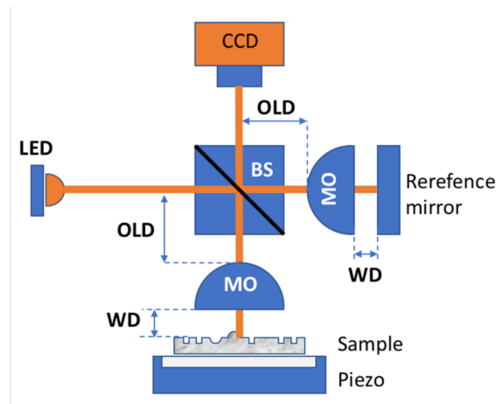


Figure 26. General scheme of a high precision Linnik interferometer. working distance (WD), the axial objective lens distance (OLD) [85].

This system results in a lateral resolution in the submicron range and a working distance of more than 5 mm. Moreover, it is capable of resolving small rectangular structures of 300 nm lateral extension and 600 nm of pitch length.

### 3. Immersion Linnik in water

The Linnik design proposed by Oh et al. [89] is for an immersion system for measurements in water, using a vertical reference arm. Two identical microscope objectives were used in both the reference and sample arms (Figure 27). A wavelength range of 0.9 µm to 1.4 µm was used for the water-immersion objectives employed, giving decreased scattering and greater optical penetration into tissue and aberration-free imaging. Several inexpensive off-the-shelf microscope objectives were tested, and an objective from Optics for Research (OFR-LMO 20×, 0.45 NA in air, working distance 2.1 mm) provided good imaging performance in this wavelength range. With water-immersion, the round-trip loss of this objective was about 4.5 dB, which can be mainly attributed to the mismatch between the illuminating wavelength and the design wavelength of the stock dielectric anti-reflection coating (optimized for a wavelength of 0.8 µm).

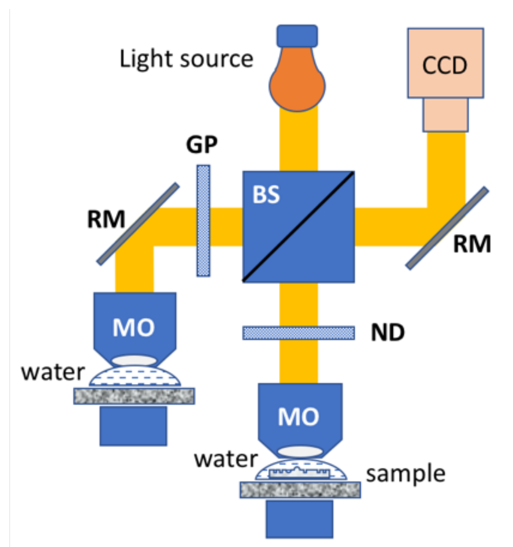


Figure 27. Schematic of Linnik setup. ND, neutral density filter; GP, glass plate; DAQ, data acquisition board in computer [89].

A neutral density filter (NDF) was used to adjust the intensity of the reference light in the reference arm of the interferometer so as to enhance the visibility of the interferogram [87]. Due to the material dispersion imbalance of the NDF, a glass plate of the same material was placed in the sample arm [90].

### 4. Leitz-Linnik microscope in air

At ICube, an older Leitz-Linnik microscope has been used for several years [91][92][93], and has turned out to be one of the best Linnik designs used in the team. The particularity is the very well designed mechanical mechanism for changing the OPD between the two arms of the interferometer using a fine rotational screw as well as the angular tilt mechanism of the reference objective and mirror arm. The reference mirror is also very well designed, with a focusing screw. The modified system developed at ICube is shown in Figure 31, equipped with two 50× objectives and an incandescent lamp (centered at a wavelength of 580 nm), giving a lateral optical resolution of 0.42 µm with a CCD camera (Basler-AVA 1000), and using a piezo scanner (PIFOC from PI) for vertical scanning of the sample. The computer specification is an Intel® Xeon® CPU working at 2.33 GHz with a RAM of 8Gb.

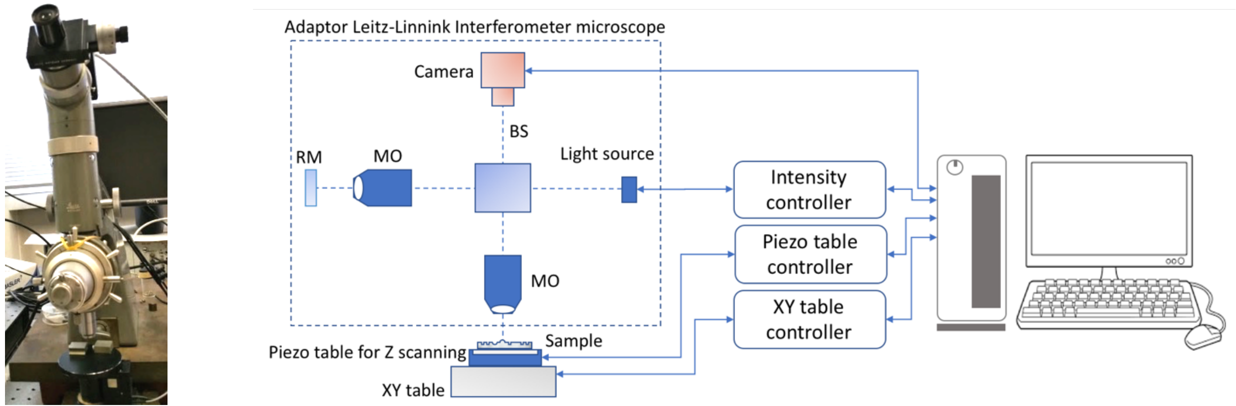


Figure 28. The system of Leitz-Linnik microscope developed at ICube [92].

## 2.3 Compact system vs breadboard

To carry out such work on new microscope instrumentation, there is a choice between using a breadboard based system and an integrated, more compact microscope system. Breadboard systems are usually used for new microscopes, but in the case of the Linnik design, using a commercial system has its advantages. The selection of using which system has its own advantages and disadvantages based on the purpose, the stability, the cost and other reasons. Table 7 presents the comparison of both systems according to the experience gained in the IPP team.

Table 7. Comparison of compact system and breadboard system

| **Comparisons of** | **Compact system** | **Breadboard** |
|---|---|---|
| Stability | Higher stability | Needs realigning everyday |
| System | Protection of optical parts required (closed system) | Regular cleaning of optical components required due to exposure to dust and dirt (open system) |
| In practice | More practical for characterizing samples | More adapted to demonstrating proof of principle |

In practical applications, the compact system has certain advantages compared with the breadboard, such as its better stability. Unlike the breadboard, the compact system does not need realignment every time it is used. But, the breadboard system is much easier to change or to adapt for certain purposes and for demonstrating proof of principle in practical applications. Then, the disturbance from the outside environment of the breadboard system is sometimes not able to avoid dust or dirt in the system. With the compact system, the optical parts inside the system are more protected from outside influences such as dirt, dust, etc. These are the main reasons why we chose to modify a compact commercial system.

## 2.4 Conclusion

In publication record, the Linnik configuration is less used than other interferometer configurations such as Mirau and Michelson. This is mainly due to the difficulties of optimizing the design and adjusting the configuration. It also was not easy to find many models described in the literature search. But finally, several configurations of Linnik in the air as well as those using water immersion objectives were found, published by P. Lehman and Al., A. Dubois et al., And Oh et al.

In this chapter we have summarised the different designs of Linnik interferometers described in the literature, working both in air and in liquid immersion such as the Linnik design proposed by A. Dubois et al. used in FF-OCT imaging in living tissue uses a polarizing beam splitter that provides the advantage of the simplicity of intensity balance to overcome the problem of the different reflectivities of the optical surfaces. Then the Linnik design in water proposed by Oh et al. [89] uses a neutral density filter to adjust the intensity of the reference light in the reference arm of the interferometer so as to enhance the visibility of the interferogram and a glass plate was placed in the sample arm to overcome the material dispersion imbalance of the filter.

While in the IPP team (ICube), an older Leitz-Linnik microscope was used for several years and proved to be one of the best Linnik models used in the team. The peculiarity is the mechanical mechanism very well designed to change the OPD between the two arms of the interferometer using a fine rotation screw as well as the mechanism of angular inclination of the reference lens and the mirror arm. The reference mirror is also very well designed, with a focus screw.

## 2.5 Résumé du chapitre 2

Dans ce chapitre sont présentées des différentes configurations de l'interferomètre Linnik dans le but de voir comment optimiser le design. La configuration Linnik nécessite deux objectifs appariés pour les deux bras de l'interféromètre directement en face de l'échantillon et du miroir de référence, ainsi qu’un cube séparateur de faisceau. Dans cette configuration, aucun composant est nécessaire entre l'objectif et l'échantillon, permettant ainsi l'utilisation des objectifs de fort grossissement, typiquement de 50× à 200×. Des grossissements inférieurs peuvent bien sûr également être utilisés. Une des principales exigences est que les longueurs des trajets optiques des deux bras doivent être égales, ce qui nécessite le réglage séparé de la différence de longueur de chemin optique et la focalisation du miroir de référence et de l'échantillon, souvent très difficile à obtenir. La sensibilité de l’interféromètre Linnik aux influences mécaniques est une des raisons pour laquelle il est très rarement utilisé et donc très peu utilisé dans des

systèmes commerciaux. Cependant, l'utilisation de la configuration de Linnik présente plusieurs avantages, notamment :

a. Les longueurs de trajectoire optique et la mise au point dans les deux bras peuvent être ajustées indépendamment.
b. Des objectifs à fort grossissement peuvent être utilisés (50×, 100×, 200×).
c. Les objectifs d'immersion peuvent être utilisés.
d. Il est facile d'insérer un composant optique dans les bras objet et de référence de l'interféromètre, comme par exemple des lames demi-onde, des polariseurs pour travailler en lumière polarisée.

Le faisceau d'éclairage, dans l'installation de Linnik est divisé en deux par le séparateur de faisceau et les faisceaux réfléchis provenant de l'échantillon et du miroir de référence sont recombinés et détectés par le détecteur (caméra). Les deux images sont donc superposées sur le détecteur de la caméra. Cette configuration peut être utilisée en mode imagerie classique (microscopie optique) en bloquant le trajet de la lumière dans le bras de référence. Les deux objectifs doivent être placés de façon précise sur les axes optiques. Même de petits angles d'inclinaison ou désalignement peuvent conduire à des effets de dispersion importants dans les résultats de mesure. Ensuite, l'objet et le miroir de référence doivent être placés exactement à la distance de travail (WD) donnée par la distance focale de l'objectif. La distance axiale de l'objectif (OLD), c'est-à-dire la distance entre les objectifs du microscope et le centre du séparateur de faisceau, est également importante.

Dans un interféromètre Linnik, la recherche des franges se fait en trois étapes :

1. La distance miroir-objectif doit être réglée de façon à être focalisé par l'objectif de référence et le bras de référence est bloqué.
2. L'objectif objet est focalisé sur un endroit de l'échantillon relativement plat (les franges ne sont pas encore visibles)
3. Enfin la distance axiale de l'objectif miroir (OPD) est modifié afin de trouver le meilleur contraste de franges tout en restant focalisé sur l'objectif (avantage du Linnik)

Lorsque l'échantillon est balayé axialement (Z) par l'actionneur piézoélectrique, chaque pixel de la caméra enregistre l'amplitude du signal d'interférence. Le point le plus haut sur l'enveloppe des franges détermine la position axiale de l'échantillon.

Les objectifs d'immersion peuvent être utilisés pour permettre la mesure de l'échantillon dans un milieu liquide et ainsi augmenter la résolution latérale du microscope en raison de l'ouverture numérique plus élevée résultant du milieu de mesure d'indice de réfraction plus élevée que celle de l'air. Les objectifs à immersion dans l'eau sont

utilisés pour minimiser les effets de dispersion dans les bras de l'interféromètre pour un balayage en profondeur dans des échantillons transparents et pour réduire la réflexion de la lumière à la surface de l'échantillon.

La configuration Linnik est moins utilisée que les autres configurations d'interféromètre tels que Mirau et Michelson. Ceci est principalement dû aux difficultés d'optimisation de la conception et au réglage de la configuration. Dans la recherche bibliographique, il n'était pas facile de trouver un grand nombre de publications relatif à l'utilisation de Linnik. Cependant plusieurs configurations de Linnik dans l'air ainsi qu'en immersion dans l'eau ont été publiés notamment par P. Lehman et Al., A. Dubois et al., Et Oh et al.

Dans l'équipe IPP (ICube), un microscope Leitz-Linnik compact, plus ancien, a été utilisé pendant plusieurs années et s'est avéré être l'un des meilleurs modèles Linnik utilisés dans l'équipe. La particularité de ce système est le mécanisme de réglage très bien conçu pour changer l'OPD entre les deux bras de l'interféromètre en utilisant une vis de rotation fine ainsi que le mécanisme d'inclinaison angulaire de l'objectif de référence et du bras de miroir. Le miroir de référence est également très bien conçu, avec des vis de mise au point.

# CHAPTER 3

# WATER IMMERSION LINNIK HEAD AND COMPENSATION

# 3.1 Introduction

A second commercial design of Linnik developed within the IPP team is based on the Fogale-Nanotech OEM system with a Linnik interferometer (Figure 30), financed by the IPHC team (R. Barillon) in the context of a collaboration for studying pollutants in colloidal layers. A basic system that was incomplete, without the reference mirror mechanism was acquired, with the aim of modifying it at ICube. The modifications carried out to the Fogale microscope were performed in several steps starting by adding a reference mirror mechanism within the framework of the PICS project (BAS, Bulgaria) and then changing the original Linnik Fogale from use in air to use in water.

To convert the interference objective head to a Linnik-immersion setup, several steps had to be taken such as adding immersion objectives and developing a path length compensation solution to the horizontal reference arm. In addition, some important modifications had to be made to the system to make it practically useable. Certain mechanical parts had to be designed, made and installed in the new system and a motorised table added to the reference arm to simplify path length compensation.

The final purpose of this modification work is to combine CSI with ATR-FTIR for the combined analysis of thick inhomogeneous colloidal layers [93], shown in Figure 29. To this end, the system will be tested on the characterization of colloids (dry, wet, cell with flowing water containing contaminants) at IPHC. The ATR-FTIR technique is possible to obtain the information in molecular level of the colloid or solution surface. The result of CSI is used as the control parameters in order to compare the measurement result and to obtain information of the reproducibility of sample used in ATR-FTIR measurement. These control parameters are as following:

1. Coverage rate of the surface.

   The coverage rate of the colloid or material distribution on the substrate surface could be observed and controlled by the 2D image of CSI. This information then is used to control measurement of ATR-FTIR technique.

2. Maximum thickness of colloidal/ sample layers.

   The maximum thickness of colloidal layers is observed by the 3D image of CSI. The maximum layer thickness is not allowed beyond the penetration depth of the evanescent wave in ATR. Otherwise, reproducing the new sample will be carried out.

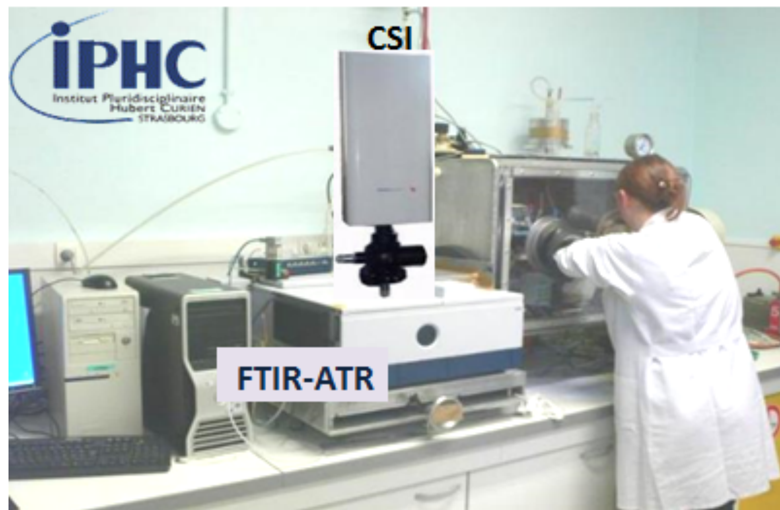


Figure 29. Illustration of combining CSI technique and ATR-FTIR.

The next sections present the Fogale microscope design, specifications, modifications carried out, resulting performance, measurement results, and a discussion related to the problems of being able to use it for measuring in water.

The section will be started by presenting the initial Fogale microscope design with the specifications and the performance. Then the different steps of the modifications are described:

- Changing the initial Fogale Linnik design and support system for use with a Mirau objective and a more stable microscope support.

- Modifying the microscope for use from the Mirau objective to the Linnik in air.

- Modifying the Linnik in air for measurements in water by using polymer compensation in the horizontal arm between the reference mirror and the reference objective.

- Installing the stepper motor in the reference arm for simplifying the finding of the fringes.

The performance of the system after each modification is tested by measuring different types of test samples and comparing the results with those from other microscopes on the same samples. In order to determine the resolution, measurements were performed on a RS-N type grating standard calibration (SiMETRICS). Presentations of the problems found and how they were resolved are discussed throughout the chapter.

# 3.2 Initial Fogale microscope

The original Fogale microscope existing at the beginning of the project was the partial immersion Linnik head shown in Figure 30. The old support column and optical benches used for supporting the microscope can also be observed. A teflon reservoir with glass window had been developed (Figure 31) for studying the growth of biomaterial layers under the microscope in a bath of simulated body fluid (SBF). This had been developed within the context of the PICS project [94] and in collaboration with the team at IPHC (Strasbourg) for the study of thick layers of colloids [93].

## 3.2.1 Instrumentation description

The photos in Figure 30 show the different parts of the microscope: the piezoelectric scanning system (in the middle of the column), the interferometer Linnik head (at the bottom of the column) and the teflon water bath (white) in the SBF solution in a pyrex container which is mounted on an XY manual positioning stage. The whole assembly is mounted on an anti-vibration optical table.

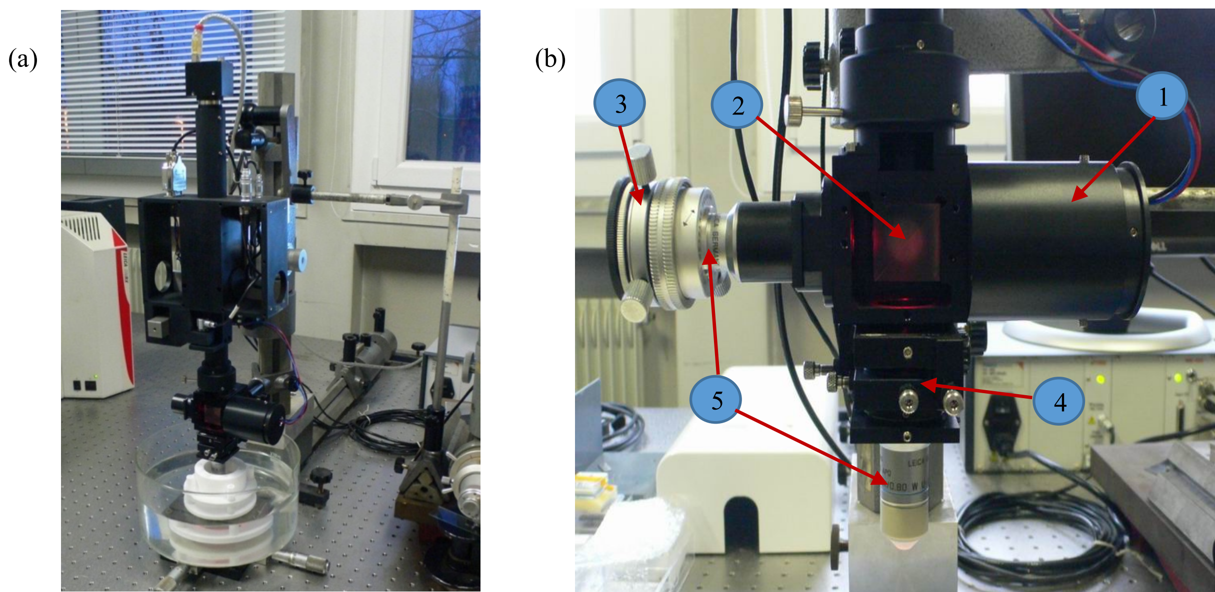


Figure 30. Details of the initial Fogale Nanotech microscope in 2014 showing (a) the microscope mounted on old optical benches on the vibration isolated table and (b) the previous Linnik immersion head [94] with (1) LED light source, (2) beam splitter, (3) reference mirror assembly consisting of an adapted Mirau mechanism, (4) orientation adjustment and (5) the immersion objectives.

The details of the different components used in the initial Fogale microscope design are as follows:

1. The light source used is a switchable double LED system, with one red LED (wavelength 640 nm) and one white LED (LXHL-MW1D, centre wavelength of 550 nm) with 45 lm of luminous flux and 3.99 V of the maximum forward voltage. The white LED is based on Indium gallium nitride (InGaN) semiconductor material (data sheet in Annex 1).
2. The beam splitter consists of a non-polarizing cube beam splitter with R/T= 45/45 and a size of 25.4 mm (data sheet in Annex 2).
3. The reference mirror mechanism consists of an adapted older Mirau mechanism, making use of the tip/tilt stage, the screw path length adjustment ring and the semi-reflecting window as the reference mirror.
4. The object path objective is mounted on a tip/tilt stage which also includes a centering mechanism for changing the lateral position of the objective in the optical path.
5. The two Leica immersion objectives consist of two pairs corrected for water immersion, one having magnifications of ×20 with a working distance of 3.5 mm and the other having magnifications of ×40 with a working distance of 3.3 mm (specifications in Annex 3).

The details of the Teflon bath and previous immersion head are shown in Figure 31.

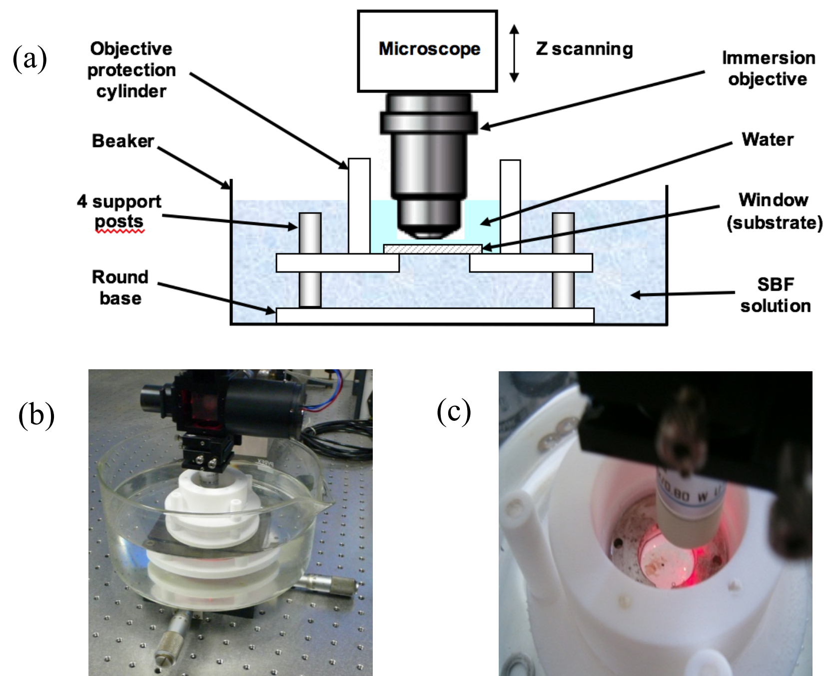


Figure 31. Details of the previous immersion head for the *in situ* characterization of the growth of HA layers in SBF solution, showing (a) the schematic layout, (b) the immersion head immersed in SBF solution and (c)the inside of the Teflon bath with the immersion objective, the water and the observation window [94].

### 3.2.2 Description of control and analysis software

The control and analysis software at the end of the PICS project (2013) was based on CPM2011, the main software at that time developed in the IPP team under LabView with the ImaqVision module for image processing. Different tools were available for measuring samples and processing the resulting data. The interface can be used for both the phase stepping (PSM) and envelope processing (CPM) techniques.

In the PSM technique, the main algorithm used is the five-step technique in which phase steps of $\pi/2$ are chosen. These are used to actuate the piezo positioner which moves the whole interferometer head and the images acquired at each phase position. After processing, the gray-scale image is obtained and can be analysed for example using the line profile function to observe and measure the surface profile.

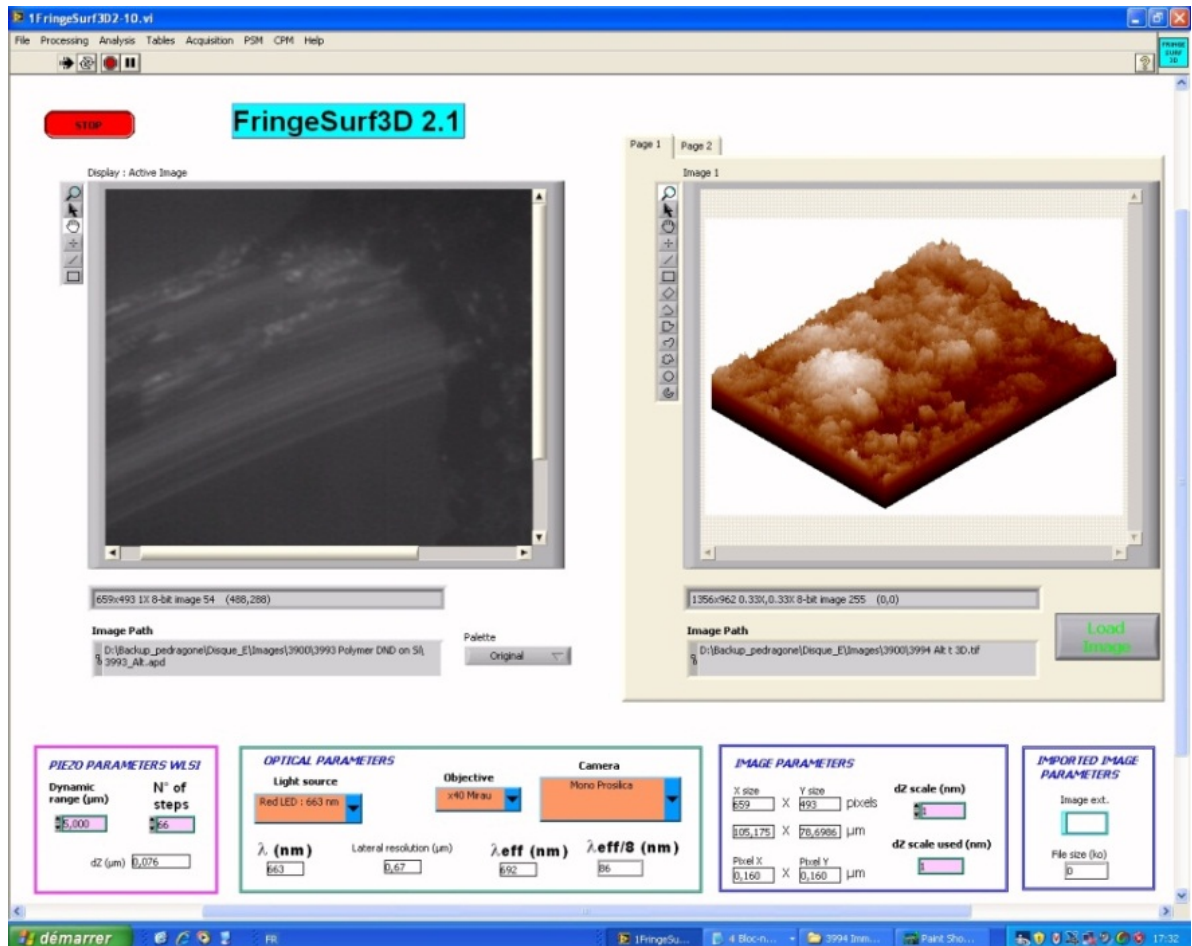


Figure 32. Interface software “FringeSurf 3D 2.1” for measuring the surface roughness (2013).

In the CPM technique, a series of images are acquired during the actuation of the piezo to each step height (dZ) along the dynamic range (DR), where DR and dZ values are set before the acquisition process. Then the gray-scale image (heights) and the maximum

intensity image $I_{max}$ are obtained by processing the stack of scanned images using the FSA method with or without the averaging option. Then the gray-scale image can be used to analyse the surface profile and generate a 3D image. The $I_{max}$ image consists of an accumulation of the maximum visibility values at each pixel (peak of the envelope) resulting in an extended depth of field image. Other algorithms exist such as the PFSM algorithm (maximum fringe intensity) and demodulation using image processing of the XZ images in the XYZ stack. The new versions of the software and the modifications made to the version used for the present work are described throughout the text.

The software “FringeSurf 3D 2.1” developed during the PICS project for the previously modified Fogale microscope was a simplified version taken from CPM2011 in 2014. This software enabled the control of the LED illumination, the piezoelectric table and the camera through the Fogale control box. The number of functions had been reduced to the minimum needed for ease of use. Details of the front panel can be seen in Figure 32. Further sub-programs allowed for example the taking of snapshots using a "time lapse" function over intervals of 5 -10 minutes to several hours/ days.

### 3.2.3 Discussion

In considering the modification to be carried out, two main difficulties existed in the design of the original Fogale microscope based on the Linnik head. The first one was the difficulty of balancing the distance of the two arms of the Linnik interferometer to obtain the interference fringes suprimposed on a focused image of the submerged substrate. The initial system was so difficult to align that in practice, the fringes had been found only once! The problem was the tip/tilt adjustment mechanism being placed on the sample objective arm, leading to defocusing each time the OPD was changed. The second main problem was the overall instability of the microscope with it being placed on old style steel optical benches.

## 3.3 Modification of Fogale microscope

The first steps of the project of developing an immersion Linnik therefore involved making modifications to the original Fogale microscope to make it stable and workable for making measurements in air with a standard Mirau objective. To reach this aim, several steps of modification needed to be done that are described in the following sub-sections.

### 3.3.1 Initial Fogale to Mirau setup

In face of the difficulties and limitations of the initial Fogale microscope, the first modification to be performed was to change the objective setup from Linnik to Mirau.

This step was taken with the aim of testing the microscope using a Mirau objective which would be easier for finding the fringes and making some of the first measurements.

#### 3.3.1.1 Instrumentation modification

The mechanical instability problem in the initial Fogale microscope was solved by replacing the old steel optical bench column (item 1 in Figure 33(a)) with a new modern aluminium optical bench as the column (piece 1 in Figure 33(b)) that is wider, taller, and more robust than the old one. This was firmly fixed to a metal baseplate, making the overall much more stable. The Mirau objective was then installed in the position of the sample objective of the Linnik (Figure 33(b)), on the manual tip/tilt stage (item 3 in Figure 33(b)). The modification can be followed by the details given in Figure 33.

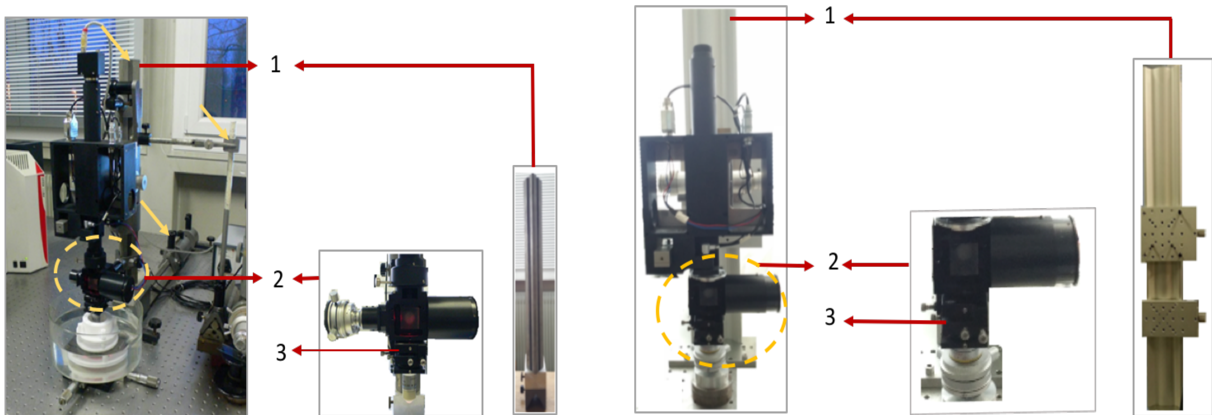


Figure 33. The first step of the modifications from (a) the initial Fogale Linnik microcope design on the old steel optical bench column (1) to (b) the Mirau objective setup on the new aluminium optical bench column (1) and the head (2). The tip/tilt mechanism is indicated at (3).

#### 3.3.1.2 Description of "FringeSurf 3D 3.1" control and analysis software and of "MountainsMap" surface roughness analysis software

The new "FringeSurf 3D 3.1" control and analysis software dedicated to this modified Fogale microscope setup (2014) for making measurements of sample surfaces was developed by Audrey Leöng-hoi (PhD in 2016). The main interface window can be seen in Figure 39.

The functions retained were the simple 5-step PSM algorithm for measuring small roughness and the FSA algorithm for measuring deeper µm depths. The classical analysis tools of line profile and 3D image were also retained.

A supplementary commercial software was also used for analyzing the measurement data, namely "MountainsMap Universal" version 6.2 developed by Digital Surf. This

software is used to present measurement data in several ways such as line profile of certain areas, the grey scale image in 2D, 3D image, and height-depth measurement of surface profile.

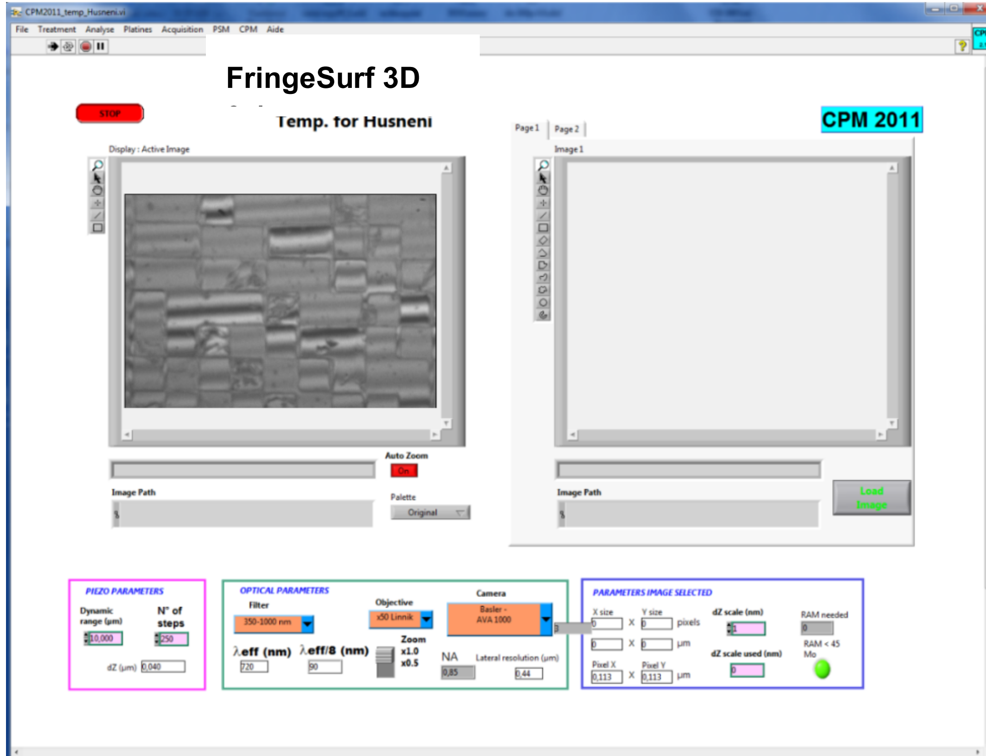


Figure 34. The control and analysis software “FringeSurf 3D 3.1” for measuring surface roughness with the Mirau Fogale microscope (2014).

### 3.3.1.3 First measurements using the Mirau Fogale

With the modifications previously described, the very first results using the Mirau setup on the Fogale microscope could be made. The fringes were of high contrast and the fringe spacing and orientation could be controlled using the dedicated adjustment screws on the Mirau mechanism.

Some of the first measurements were carried out on a diffractive optical element (DOE) consisting of resin on silicon and on a C-S-H colloid sample. C-S-H is an aggregation of precipitated, colloidal-size particles that bond together over time [95].

The experimental conditions used were the Leica Mirau ×10 objective, red LED illumination, and the Basler AVA 1000-100gc CCD camera (color, resolution 1024×1024 pixels, digitization 8 bits, image rate 101 im/s). The use of the red LED for the first measurements was chosen due to the ease in obtaining fringes because of the longer coherence length of the light.

The first fringes found on DOE are shown in Figure 35 and the results of the measurement using the FSA technique are shown in Figure 36 and Figure 37 using the line profile and 3D image function of the “FringeSurf 3D 3.1” software.

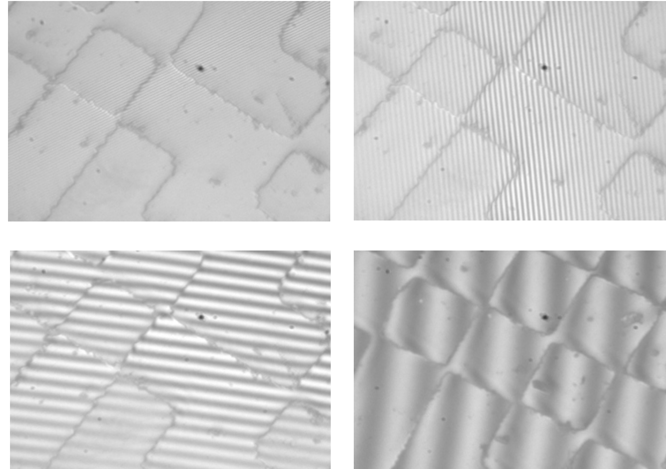

Figure 35. The first fringes were found for testing the Mirau Fogale using the red LED. The contrast and spacing are changed by using the adjustment screws in the Mirau mechanism.

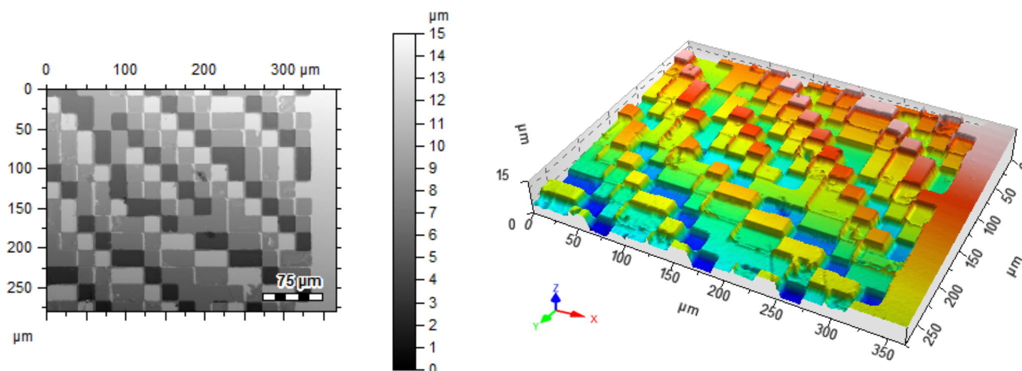


Figure 36. The altitude and 3D images of DOE using the ×10 Mirau Fogale head with the red LED, $\lambda_{eff}$ = 640 nm, dynamic range 15 µm, and step height 0.078 µm [4415].

These results were very encouraging as they are similar to what can be found using other interference microscopes [96].

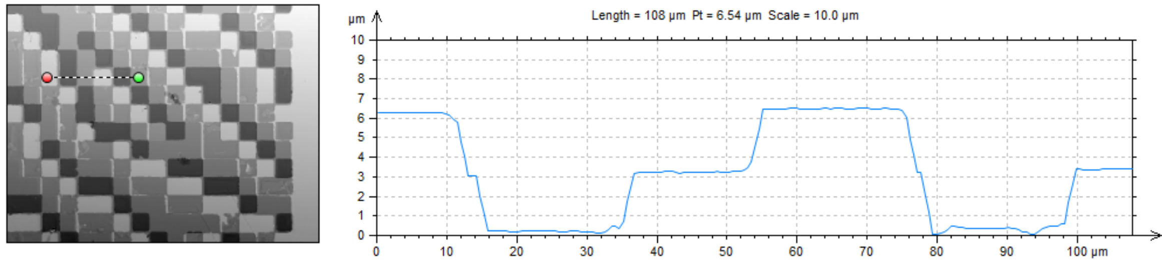


Figure 37. Line profile of the measured area of DoE using the ×10 Mirau Fogale head with the red LED, $\lambda_{eff}$ = 640 nm, dynamic range 15 µm, and step height 0.078 µm [4415].

The results of the measurements on the C-S-H are shown in Figure 38 (the altitude and 3D images of C-S-H colloid) and Figure 39 (a line profile taken from the measured area). These results were obtained using the MountainsMap software by exporting the greyscale altitude image resulting from “FringeSurf 3D 2.1”.

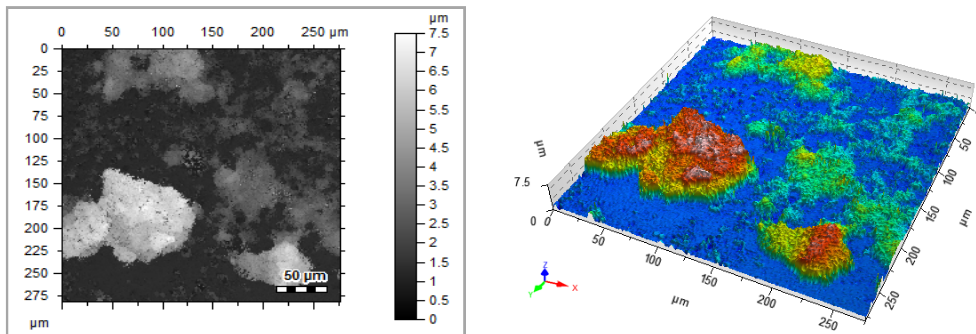


Figure 38. The altitude and 3D images of C-S-H colloid using the ×10 Mirau objective and the Fogale head with the red LED [4433].

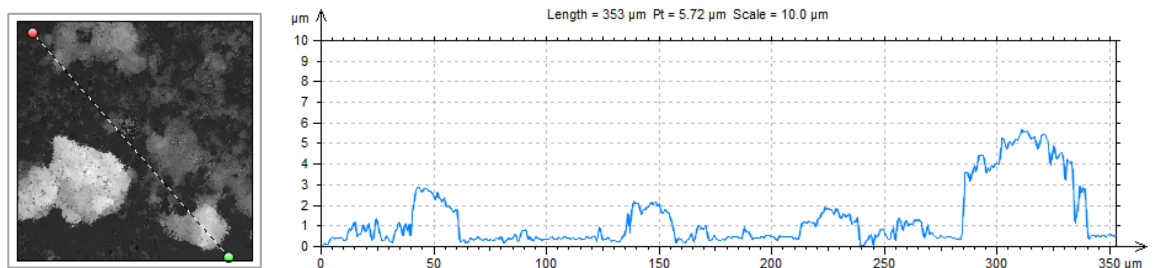


Figure 39. Line profile of the measured area of C-S-H colloid on the line using ×10 Mirau Fogale head with the red LED [4433].

Colloids are known to be difficult to measure because of their high roughness [93]; however, the first measurements on this sample were encouraging, without too many artifacts. The artifacts that can be observed consist of unmeasured points and observation of the buried substrate through the colloid.

In conclusion, the first modifications of the original Fogale microscope in using a more stable column and the Mirau objective results in a system that is more stable and able to be used for measuring different samples and then studied using the "FringeSurf 3D 2.1" software.

### 3.3.2 Mirau to Linnik in air

After successfully obtaining measurements with the new Fogale system using the easier to use Mirau objective, several modifications and adaptations were then needed to move towards the use of the Linnik objective setup.

#### 3.3.2.1 Instrumentation modification

To change the setup from Mirau to Linnik, several steps were performed, as illustrated in Figure 40. These consisted of:

1. Moving the objective tip/tilt stage and OPD adjustment from the sample objective arm to that of the reference mirror arm of the Linnik setup (block 1 in Figure 40 (a), see also the detail of orientation in Figure 41). This was not easy to carry out, requiring several adaptations and modifications to succeed.

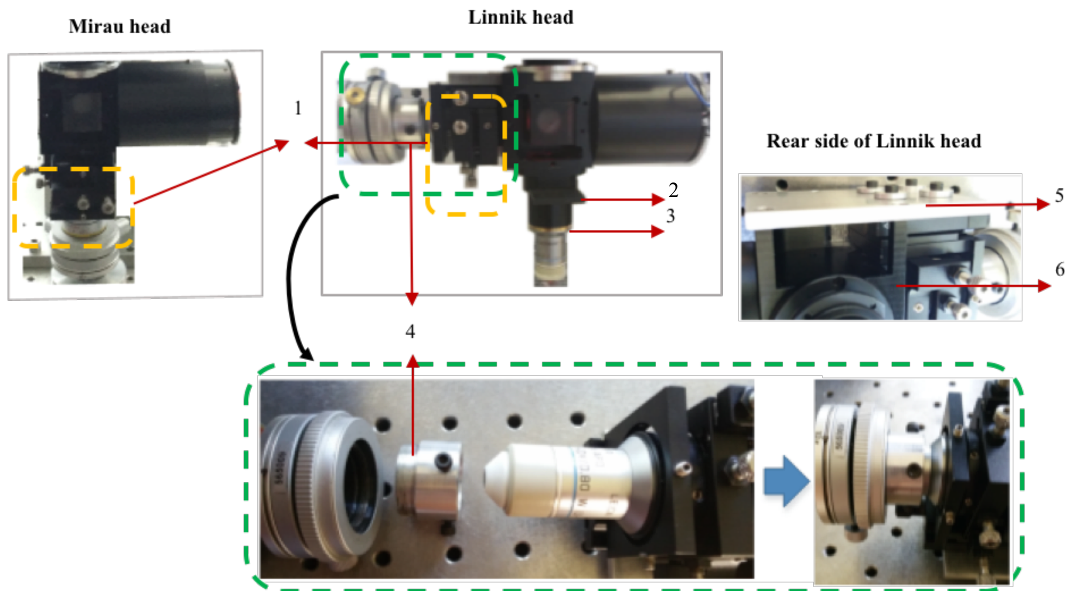


Figure 40. Illustration of the modification of the Linnik head. The tip/tilt and centering mechanism (1) is moved from the object to the reference arm and the beam stopper (2) and 8 mm-thick ring (3) are moved from the reference arm to the object arm. An adaptor tube (4) is used to mount the Mirau mirror mechanism on the reference arm. An adapted back plate (5) and an adapted cube holder (6) are installed on the rear side of the Linnik head mounted on the microscope.

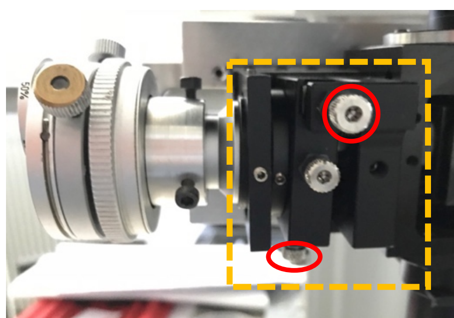

Figure 41. The objective tip/tilt and centering mechanism. The screws marked by red circles are used to change the angle of the objective in order to change the fringe orientation separation.

2. Changing the old Mirau mechanism used for the reference mirror (Figure 33) for a new Mirau mechanism (Figure 40). An aluminium tube adaptor was designed and fabricated for mounting this new Mirau mechanism (piece 4 in Figure 40, the design of piece 4 is also attached in Annex 4). The Mirau mechanism uses a semi-reflecting window as the reference mirror and allows the focusing and tilting of the mirror (see the detail in Figure 42).
3. Machining the main aluminium central cube and objective support so as be able to mount the orientation adjustment part on the reference arm, as shown in Figure 40 (rear side of Linnik head).
4. Designing and fabricating an adapted back plate for mounting the reference arm on a linear stage (OPD adjustment) which is fixed to the piezo table of the microscope (piece 5 in Figure 40).

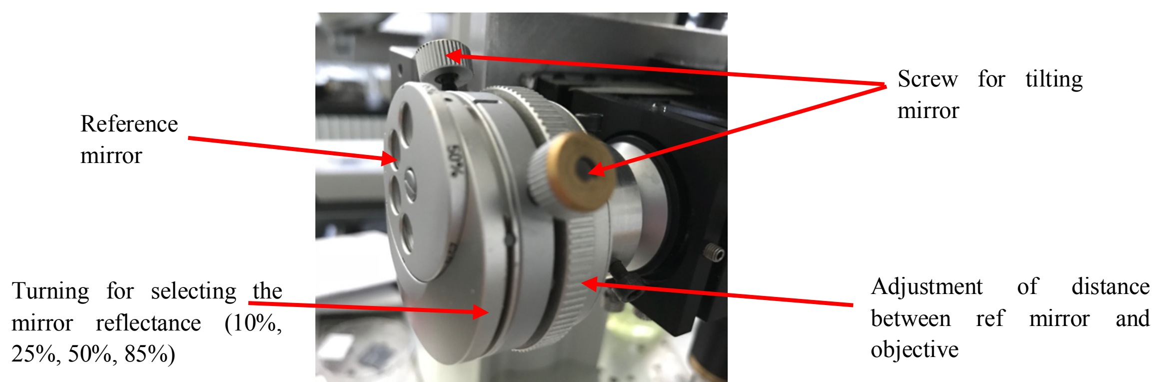


Figure 42. Adjustment control in reference arm.

#### 3.3.2.2 Problems to solve to achieve the first measurements

So as to be able to make measurements, it was necessary to obtain high quality and controllable fringes in this new modified Linnik interferometer. In order to do this, several difficulties had to be overcome. The following presents a discussion of the difficulties that had to be overcome.

**Problem of OPD to find fringes**

First, the fringes had to be found, which is not an easy task with a white light Linnik interferometer, requiring manual adjustment of the OPD to within a few µm over a few mm. One solution was to first use a laser as the light source, with a long coherence length which made finding the fringes much easier, although not at the zero OPD. The orientation of the fringes could be controlled using the tip/tilt mechanism on the reference mirror arm.

Then a red LED illumination with a shorter coherence length could be used to approach the zero-path difference, and the white light LED to find the better precision of this position. Once found, a marked plate was put on the top of the linear stage to indicate the position of the zero OPD to enable easier and quicker finding of the fringes. During this procedure, it was found necessary to make and introduce an extension ring between the objective and the cube support to extend the distance in the sample arm (piece 3 in Figure 40).

The results in Figure 43 show the first fringes with the Linnik interferometer in air using red and white LEDs and the x20 immersion objectives. It can be observed that he first fringes found using the white LED had a lower contrast than those using the red LED. While this may be partly due to the fact that the immersion objectives are not adapted for use in air, it was also due to misalignment of the Linnik and the white light fringes can be seen to be improved by certain adjustments over the course of the subsequent experiments.

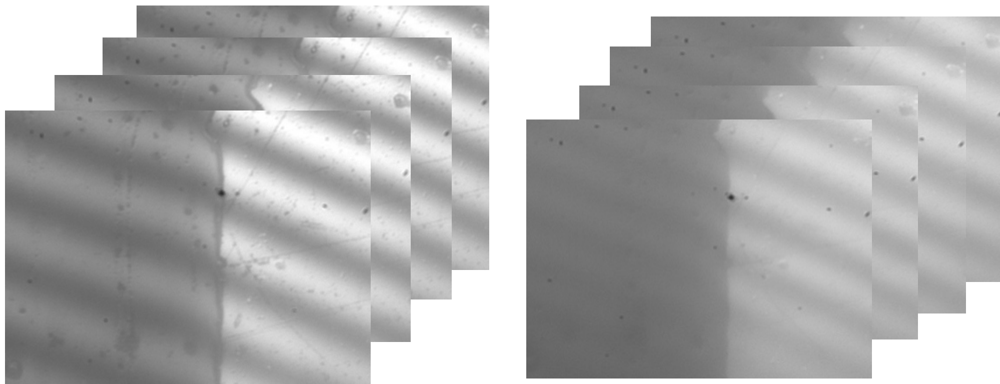

Figure 43. First fringes found by ×20 (immersion objectives) Linnik Fogale in air with red LED (left) and white LED (right) illumination.

**Difficulties associated with the white LED light source**

The first white light fringes found by measuring the intensity at a pixel along the Z-axis had an envelope that was asymmetrical (Figure 44), requiring an optimisation of the illumination source spectrum. By measuring the spectrum of the white light LED source of the original Fogale microscope using a portable spectrometer (Figure 45), this was found to be due to the existence of a gap in the mid-range of the spectrum. This is due to the LED being based on a UV excitation LED with phosphor emission in the visible

range. The UV LED is based on InN (Indium nitride) which is a semiconductor material with a small bandgap of about 2 eV emitting at 440 nm [97]. Since this problem can lead to inaccurate signal processing and surface measurements, this LED was changed for a different white light LED (LUXEON Rebel lime color, typical spectral half-width 100 nm, centre wavelength 567 nm) having a more balanced spectrum (Figure 46), the data sheet of this new LED shown in Annex 5.

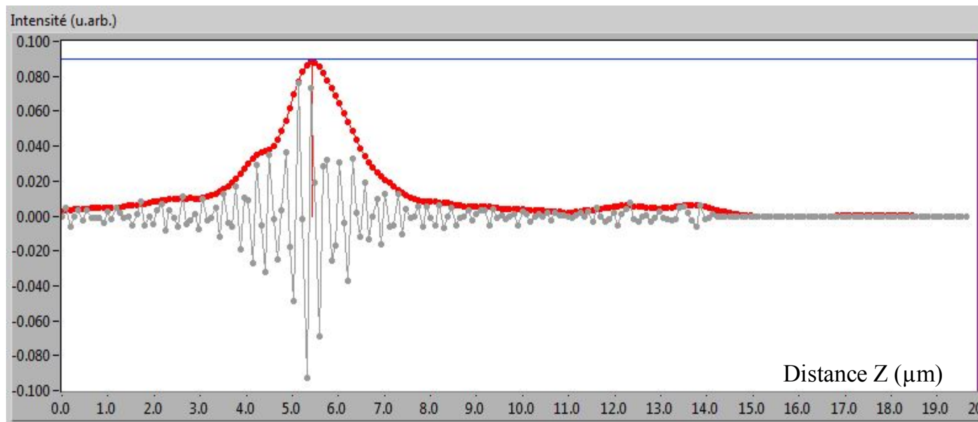


Figure 44. The asymmetrical envelope of an interferogram using the original white LED LXHL-MW1D.

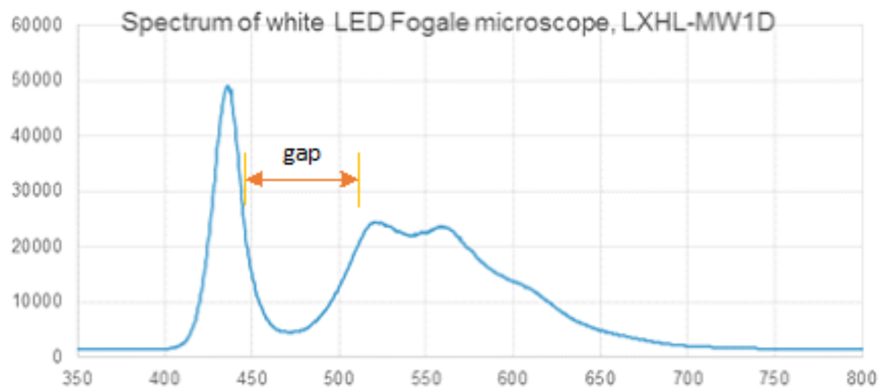


Figure 45. The measured spectrum of the original phosphor-based white LED LXHL-MW1D of the initial Fogale microscope.

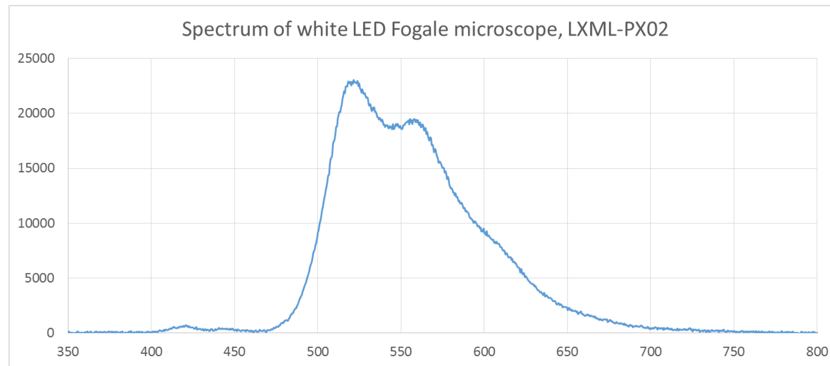


Figure 46. The measured spectrum of the new white LED (LUXEON Rebel lime color) chosen for its more balanced spectral range.

**Details of white light LED designs**

White light LEDs to replace the conventional halogen microscope source are commonly used in optical microscopy. A comparison between the use of LEDs and halogen source is given in Table 8 [98] in which it can be seen that LEDs have many advantages. A low coherence light source for white light interferometry needs to have a continuous broadband emission without spikes or modulation that can also leading to higher quality of the axial PSF [69][99].

Although white light LEDs are convenient for microscopes, compared with traditional halogen sources, as has been found in this application of white light interferometry, the variation in emission spectrum can perturb the results. This has been noted by I. Kassamakov [100] and by A. Dubois [101][98]. A. Dubois et al. demonstrated that both light sources of halogen and LED provide identical performance in terms of spatial resolution and detection sensitivity, and they declared that LED could favorably replace the halogen lamp due to the advantages of LEDs. I. Kassamakov et al. improved the sidelobe-frequency of a stroboscopic white light intererometer by choosing two nonphosphor LEDs emitting visible light with different wavelengths to balance the spectrum.

Table 8. Comparison of white light LED and conventional halogen source.

| | White light LED | Conventional Halogen source |
|---|---|---|
| Shape/form | Very compact | Fragile |
| Power consumption | Little | High |
| Energy efficiency | High | Low |
| Spectral emission | Limited solid angle | So wide |
| Long Lifetime? | Yes | No |
| Heat dissipation | None | A lot |

| Cost | Relatively cheap | Very cheap |
|---|---|---|
| Maintenance | Easy | Careful |

After many years of research and recent developments, it is now possible to generate white light using LEDs by two approaches. The first way consists of a combination of (at least) three LEDs, with power ratios adjusted to obtain white light with a specific color temperature. The second one, a single LED can be used in combination with one or more phosphor materials to partially or fully convert the LED emission, as shown in Figure 47.

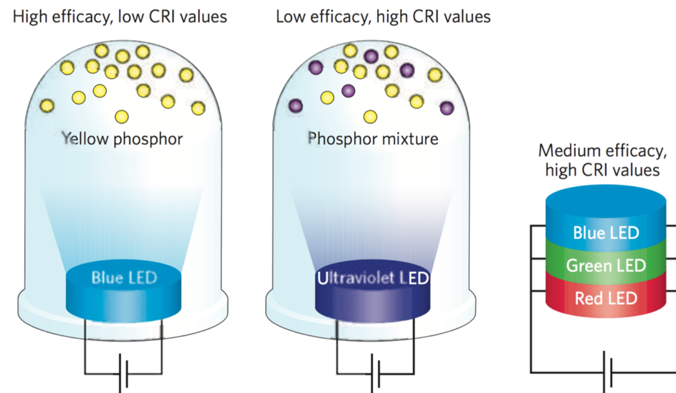


Figure 47. Three dominant ways to produce white light based on LEDs [102].

Several ways to create white LEDs using organic and inorganic sources and phospors are shown in Figure 48 [103].

| | LED based | LED plus phosphor based |
|---|---|---|
| **Di-chromatic White source** | Blue, yellow LED | Blue LED + yellow phosphor |
| **Tri-chromatic White source** | Blue, green, red LED | UV LED + triphosphor |
| **Tetra-chromatic White source** | Blue, cyan, green, red LED | Blue, red LED + cyan, green phosphor |

Figure 48. Several ways to generate white light based on LEDs implemented with di-, tri-, and tetra chromatic white sources [103].

One approach is to mix the light from several colored LEDs (Figure 49) to create a spectral power distribution that appears white. Similarly, so-called tri-phosphor fluorescent lamps use three phosphors, each emitting a relatively narrow spectrum of blue, green or red light upon receiving ultraviolet radiation from the mercury arc in the lamp tube. By locating red, green and blue LEDs adjacent to one another, and properly mixing the amount of their output the resulting light is white in appearance.

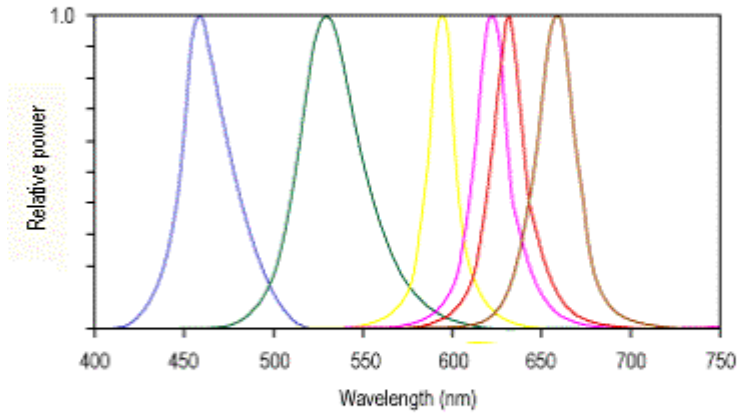


Figure 49. Spectral power distributions of several types of LEDs.

In contrast to the RGB approach, a single LED light source can be combined with one or more conversion phosphors to obtain white light. For example, when one phosphor material used in LEDs is illuminated by blue light, it emits yellow light having a fairly broad spectral power distribution. Figure 50 presents the spectra for two phosphor-based white LEDs and sunlight. In practice, by incorporating the phosphor in the body of a blue LED with a peak wavelength around 450 to 470 nm, some of the blue light will be converted to yellow light by the phosphor. The remaining blue light, when mixed with the yellow light, results in white light. New phosphors are being developed to improve color rendering as shown in Figure 51.

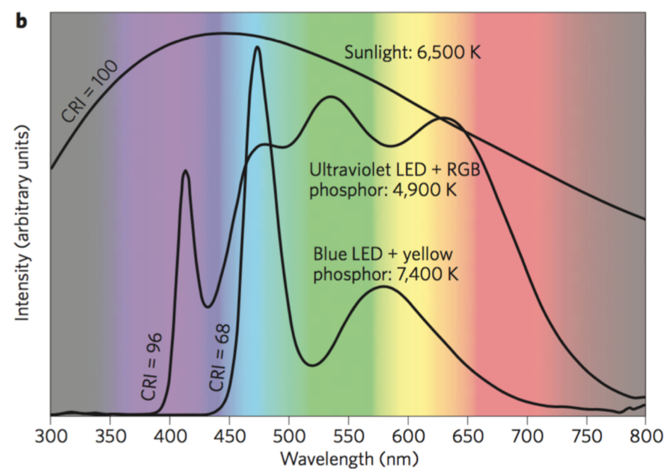


Figure 50. Comparison of the spectrum of ideal sunlight with two LED-based white-light sources.

We can conclude that most commercial white LEDs are based on a conversion process, in which the light emitted by a blue LED is absorbed by a phosphor that reemits in the yellow part of the visible spectrum, resulting in a spectrum that looks white to the human eye. This conversion approach however suffers from an inherent energy loss due to the absorption and reemission process (Stokes' loss), which can reduce the overall efficiency by as much as 30% [103]. Moreover, the emission spectrum and the lifetime of phosphor based white LEDs depend mostly on the properties of the phosphor employed.

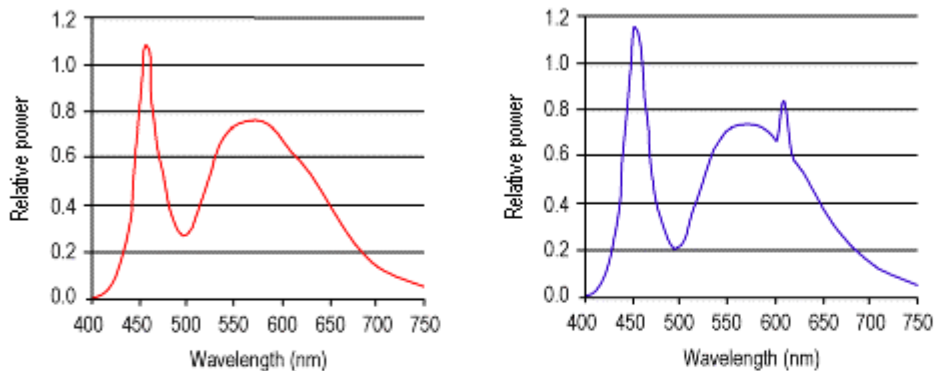


Figure 51. Spectral power distributions of early phosphor-based white LEDs (left), and white LEDs using more developed phosphors (right, in 2003) with increased output between 600 and 650 nanometers.

Higher efficiencies and better control on the emission spectrum can be obtained by mixing the light from differently colored LEDs. Usually, an RGB approach is followed by combining a red, green and blue LED into single LED light source. For even better color rendering, a yellow LED can be added to the system [104].

The higher overall efficiency of such a light source is due to the fact that there is no phosphor involved, eliminating thus the conversion loss. However, very efficient individual LEDs are required. While highly efficient red and blue LEDs are readily available, green and yellow ones currently show much lower efficiencies. This is known as the "green gap" [104][105].

In this modification, as has mentioned, the reasons that the white LED (LUXEON Rebel lime color) were chosen:

- The size of whole LED package including the thermal pad is suitable and fit for the hose body of illumination part of Fogale.

- It has no gap on the spectrum and has a more balanced spectral range, resulting in a more symmetrical fringe envelope.

Characteristics of the new LED

While checking the effective wavelength of the illumination for sample measurements carried out at different times, with different LEDs and different media, it was observed that it changed slightly. Therefore, a test of the effective wavelength of the 2 LED's was performed to observe the changes as a function of the values of the voltage and intensity. These experiments were carried out in water with dZ= 0.02 μm and DR= 3.7 μm for red LED and with dZ= 0.02 μm and DR= 1.9 μm for white light LED. The selection or determination of the LED voltage value was determined by the peak intensity of the histogram. Three peaks in the intensity were observed, at 100, 150 and 175 on an 8-bit scale.

The results of the characteristics of the red LED and white light LED are presented in Table 9 and Table 10, respectively. We can see that for the white light LED, the LED voltage and the exposure times do not change the effective wavelength. But for the red LED, there are slight changes for the effective wavelength. Subsequently, for all sample measurements, the same exposure time was used and the voltage was modified to give the same effective wavelength.

Table 9. Characteristics of the red LED with a variation in the LED voltage and exposure times that affect the effective wavelength.

| Peak intensity of histogram | exp times1 = 47998 μs | | exp times2 = 96000 μs | | exp times3 = 191999 μs | |
|---|---|---|---|---|---|---|
| | LED voltage (V) | lambda eff (nm) | LED voltage (V) | lambda eff (nm) | LED voltage (V) | lambda eff (nm) |
| **100** | 3,84 | 496 | 3,66 | 493 | 3,52 | 500 |
| **150** | 3,95 | 500 | 3,76 | 500 | 3,60 | 496 |
| **175** | 4,05 | 484 | 3,81 | 493 | 3,64 | 500 |

Table 10. Characteristics of the white light LED with a variation in the LED voltage and exposure times that affect the effective wavelength.

| Peak intensity of histogram | exp times1 = 46998 μs | | exp times2 = 57998 μs | | exp times3 = 116000 μs | |
|---|---|---|---|---|---|---|
| | LED voltage (V) | lambda eff (nm) | LED voltage (V) | lambda eff (nm) | LED voltage (V) | lambda eff (nm) |
| **100** | 2,62 | 430 | 2,6 | 450 | 2,54 | 440 |
| **150** | 2,68 | 440 | 2,65 | 440 | 2,57 | 440 |
| **175** | 2,7V | 440 | 2,67 | 440 | 2,59 | 440 |

### 3.3.2.3 Description of Linnik head and the new integrated control software

The new modified Linnik configuration uses two identical water-immersion microscope objectives in each of the reference beam and object beam arms. The microscope objectives used in this experiment are ×20 (0.5 numerical aperture and 3.5 mm working distance) and ×40 (0.8 numerical aperture and 3.3 mm working distance) from Leica. The two LED light sources that can be chosen between thus consist of the same quasi-monochromatic red LED (central wavelength of 625 nm, bandwith of 20 nm) and the new broadband white light LED (central wavelength of 567 nm, bandwith of 100 nm). Due to the numerical apertures of the objectives, the central effective wavelengths for calculating the axial fringe period are 640 nm and 620 nm respectively. These effective wavelengths are defined as twice the period of interference fringe closest to the modulation envelope peak and are affected by parameters such as the light source spectrum, the spectral emission of the optical components, the surface roughness, the NA of the objectives, and the spectral response of the image sensor array. Since the new modifications to the Linnik, a new camera had been purchased, consisting of the Photonfocus model: MV1-D2048-96-G2, having a sensor with 2048 x 2048 pixels and digitized to 8 bits at the rate of 22 frames/s. This camera is based on a CMOS image sensor optimized for low light conditions.

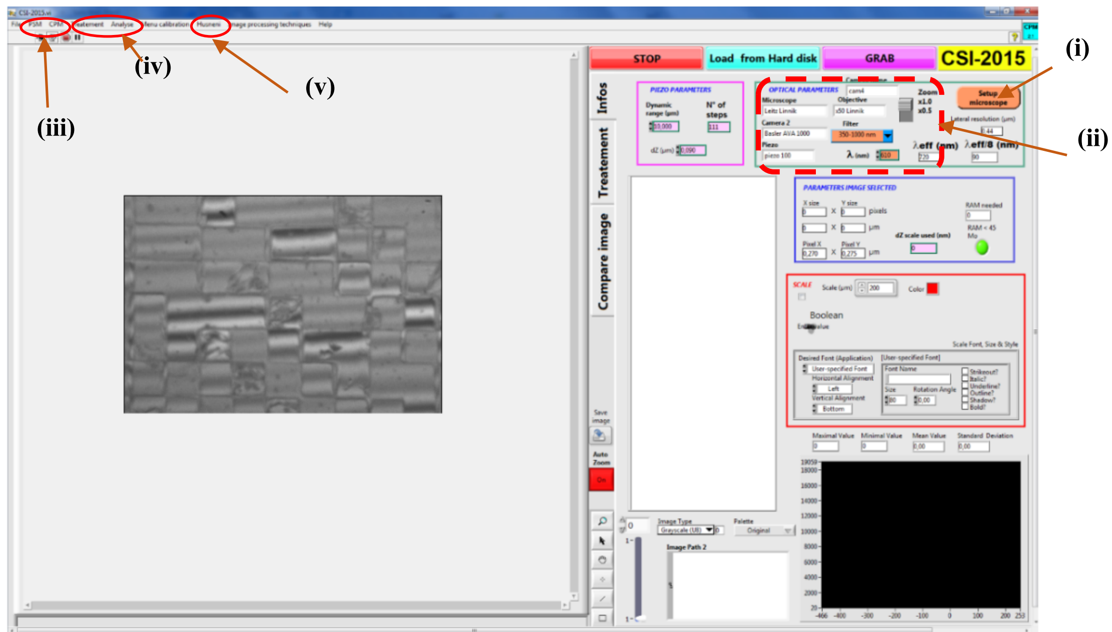


**(i)** Selecting microscope, objective and camera; **(ii)** Setting of optical parameters (DR, dZ, lambda, etc); **(iii)** Image processing CPM and PSM; **(iv)** Tools of treatment (filtering, tilting, arithmetic, etc) and analyse (line profile); **(v)**Grab and scanning image

Figure 52. Interface software “CSI-2015” for measure the surface roughness on the Linnik Fogale microscope.

New interface software dedicated to this Linnik setup was also developed by Audrey LEONG-HOI (PhD in 2016) based on the "CSI-2015" LabView programme which had a new improved user interface including choices for each microscope, camera, piezo and interference objectives.

### 3.3.3 Immersion linnik head and water compensation

The last step of the modification of the Linnik system was to adapt it for use in water. This subsection will describe the modifications carried out and the details of the results.

#### 3.3.3.1 Instrumentation modification

The experimental setup of the microscope with the water-immersion Linnik head is represented schematically in Figure 53. A water-immersion objective and a reference mirror are placed in the reference beam arm while the other water-immersion objective and sample are placed in the object beam arm. The sample to be measured is placed in a container filled with distilled water.

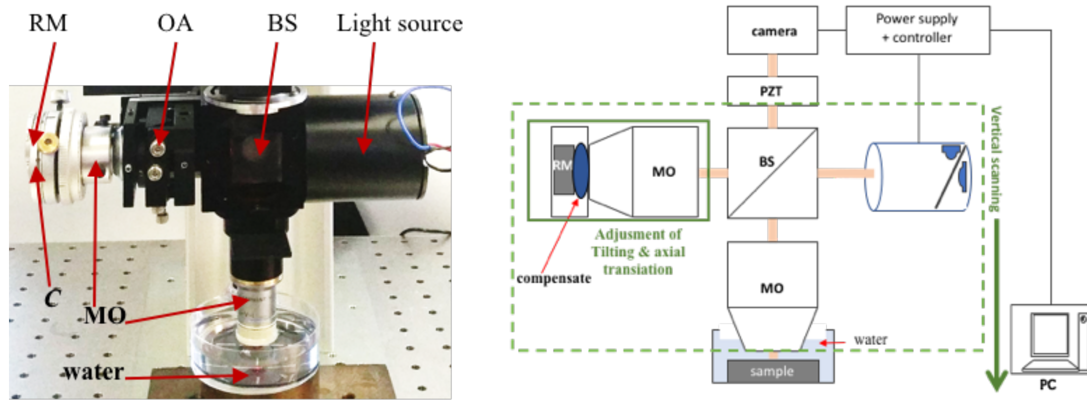


Figure 53. Experimental arrangement of water-immersion Linnik head. BS, beam splitter (broadband, nonpolarizing); MO, microscope objective (water immersion); RM, reference mirror (80% reflectivity); PZT, piezo translation.

#### 3.3.3.2 Compensation in mirror arm

The immersion Linnik configuration ideally uses water as the medium in the reference arm, to match the optical properties of the sample arm with the sample objective being immersed in water which has a refractive index of $n$ = 1.3325. But since in most Linnik designs the reference arm is mounted horizontally, this makes the use of water mechanically tricky. It is not easy to setup water in the reference arm because of its horizontal position. One solution is to put the reference objective in a miniature reservoir, such as that developed by J. Ogien [101] by designing and making a cylindrical reservoir that is fixed to the horizontal reference objective. While this has

demonstrated good results for imaging in skin, it has the inconvenience of water leakage.

Another way of compensating the reference path is by using a glass plate [89][90] in the reference arm instead of water, which enhances the visibility of the interferogram, but still introduces a slight dispersion mismatch. Yet another way is to use an objective with a correction collar to compensate for a range of OPL's (Figure 54) that is normally used to correct for spherical aberration due to the presence of a cover slip.

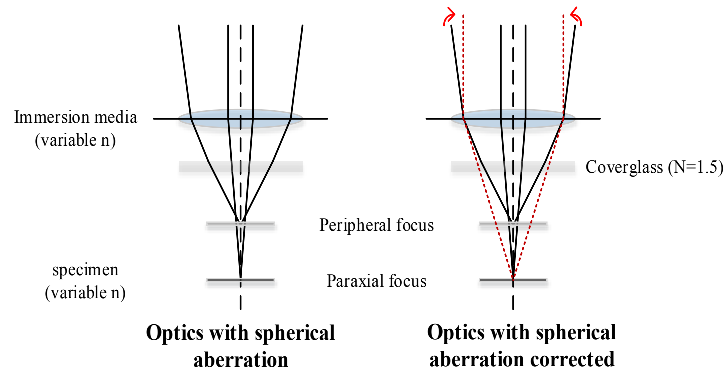


Figure 54. The schematic of how a correction collar works [106].

In this work we have investigated alternative solutions based on non-liquid elastic polymers placed between the end of the reference objective and the reference mirror. Two types of polymers were tested. The first one consists of adapted sodium polyacrylate (SPA) beads, with a refractive index very close to that of water and the second consists of polydimethylsiloxane (PDMS) slabs with a refractive index in the range of 1.335 to 1.400. The measurement values of refractive index of sodium polyacrilate and polydimethylsiloxane were measured manually using an Abbe-refractometer (the test procedure is attached in Annex 6. The procedure of Abbe-refractometer, giving values of 1.335 and 1.401 respectively.

***Sodium Polyacrilate (SPA)***

Sodium polyacrilate, known as “water lock” and “water beads”, is a polymer that has the remarkable ability to absorb as much as 200 to 300 times it's mass in water, although they have a certain fragility due to being made mainly of water. These beads, shown in Figure 55 are commonly used in different fields such as in health care (sanitary towels, paper diaper, medical bandage), industry or agronomy for retaining moisture in cultures in dry regions or in potted plants.

Figure 55. Samples of water retaining SPA polymers in the bubble shape.

In our application, SPA can be used as a substitute for water in both arms or only in the reference arm, as shown in Figure 56. As far as we know, this type of path length compensation for interference microscopy has not yet been reported in the literature. In practice, a 8-mm-diameter SPA bead is placed between the reference mirror and the objective after being cut to the thickness of the working distance of the objective used (3.5 mm and 3.3 mm respectively for the ×20 and ×40 objectives).

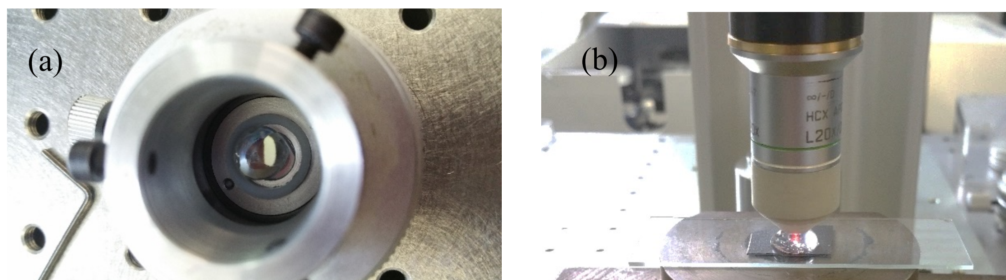


Figure 56. Use of SPA beads in the mirror arm (a) and in the object arm (b).

The advantages of using SPA are its ease of use and application in the reference arm, its ability to provide a refractive index close to that of water and the stability in its form at a maximum temperature of 25°C [107]. The only inconvenience in using this material is the bead needing to be changed after a few hours or days because of water evaporation.

***Polydimethylsiloxane (PDMS)***

The second polymer material studied is PDMS, a Si based organic polymer made of a group of polymeric organosilicon compounds with a refractive index between 1.400 – 1.405. Also known as dimethicone, this polymer is optically transparent, inert and non-toxic. The main advantages of using this material in our application are its viscoelasticity, enough flexibility to manipulate across macroscopic scales, bio-compatibility, high chemical inertness, optical transparency, and being stable at room temperature.

Unlike SPA, PDMS requires several steps of preparation before it can be used as a compensator in the reference arm. It is necessary to design the PDMS slab with the correct size so that it is suitable for the variation in working distance of each objective

magnification. We therefore made the first design of PDMS mold out of Teflon for forming the PDMS as shown in Figure 57. Then an improved second mold (Figure 58) was made with a glass plate forming the base of the mold during molding of the PDMS compound o give a flatter surface.

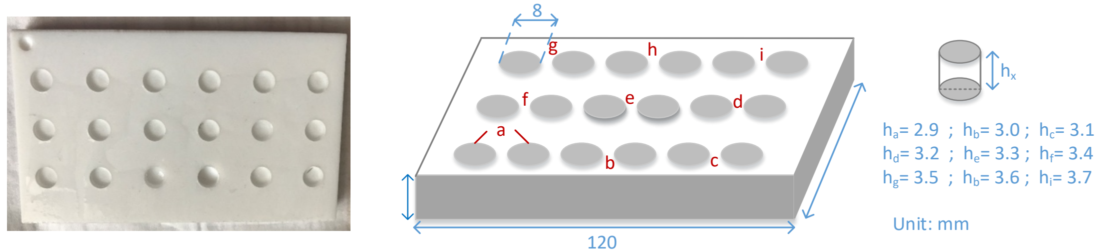


Figure 57. Design (right) and mold plate (left) for making PDMS slabs in various heights to suit the working distance of the objective.

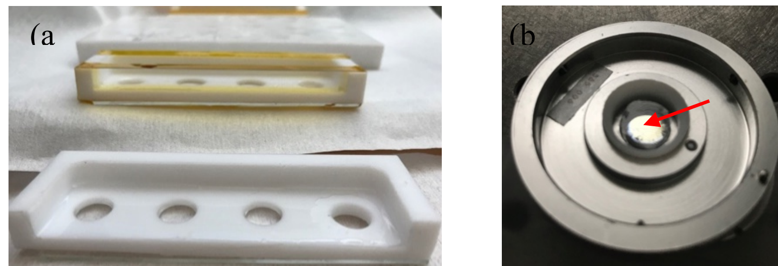


Figure 58. (a) An second improved mold design of PDMS made of Teflon with a glass plate forming the base of the mold, (b) PDMS contacts with reference mirror.

One of the requirements that needs to be considered in the preparation of the PDMS slab as a medium is that it should present an optically flat, smooth and transparent surface without marks or scratches. Furthermore, the PDMS slab should have a sufficient elasticity in order to avoid the possibility of excessive pressure on the optical components when performing the measurements. A degassing process was employed to remove bubbles after well mixing the components, before pouring the mixture into the mold, curing with an oven and drying at room temperature.

Bluesil RTV 141 was used to make the PDMS by mixing the two components. Both the PDMS base and catalyst or curing agent are scaled with a certain mass ratio. Using a different lot of catalyst/ hardener agent may affect the properties of the product, especially concerning its elasticity. Obtaining the sufficient or proper elasticity is the main aim of this PDMS experiment so that it could be applied safely on to the objective or mirror. It took several trial and error experiments of mixture composition. After performing experimental tests with different concentrations, we obtained a ratio with a satisfactory elasticity of PDMS of 25 : 1 for the PDMS base to catalyst, compared with

the commonly used ratio of 10 : 1. Some examples of molded PDMS slabs are shown in Figure 59.

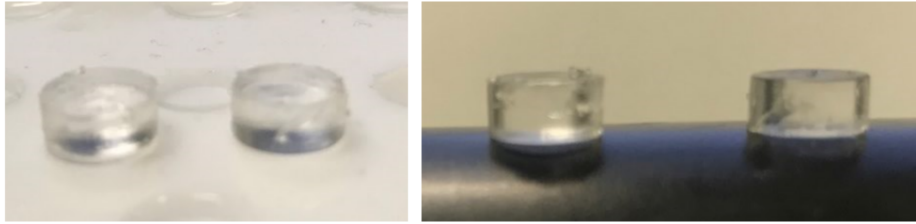

Figure 59. Some PDMS slabs.

Initial tests of these PDMS slabs were carried out by placing them in the object arm on the sample to replace the water medium. The results in Figure 60 show the variation in focusing of an aluminium layer on silicon sample demonstrating that object will be obtained using a proper elasticity of PDMS slab

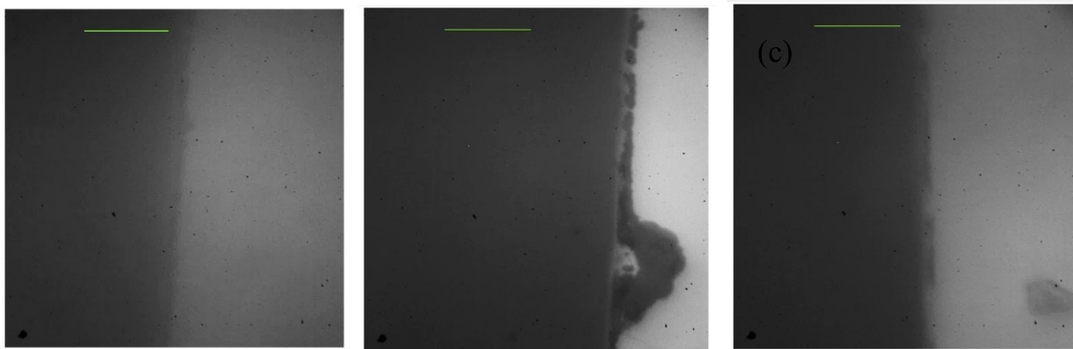


Figure 60. Difference focus positions of an aluminium layer on silicon sample placed under the sample objective with the thickness of PDMS slabs of (a) 3.4 mm, (b) 3.5 mm and 3.6mm; using ×20 immersion objective with a working distance of 3.6 mm. The best focus is (b).

As with the SPA polymer bubbles, the PDMS polymer slabs can then be used as a compensator in the reference arm. Having a non-liquid form, both of them can easily be placed in a vertical position between the reference objective and the reference mirror. However, for long term utilization, the PDMS should be stored at a temperature of less than 20$^{o}$C so as not to become too hard (the result of experimental observation), making it unsuitable for use in the reference arm.

**3.3.3.3 First measurement with immersion Linnik setup**

The first measurements made with the polymer compensated immersion system are now presented in this section. While the first results showed degraded image contrast and resolution due to the optical aberrations not being well corrected, further results showed

improvements in the measurement quality by adjusting the optical path length (OPL) to best fit the experimental design and using water-immersion objectives in both interference arms.

#### 3.3.3.3.1 Measurements with no reference arm compensation

The results of some of the first measurements performed using the water immersion Linnik head are now presented. For these experiments, measurements of an Al step on Si in air are compared with those made in water. In the first experiment with the water-immersion Linnik system, the objective scanned over the whole depth of the sample first placed in air and then in water. The images of fringes, raw signal, and envelope interferogram with red LED obtained are respectively shown in Figure 61 to Figure 63 using the ×20 objective and in Figure 64 to Figure 66 using the ×40 objective. As expected, the images of the sample are much sharper by observing it in water than in air. The fringes are also of much higher contrast in water.

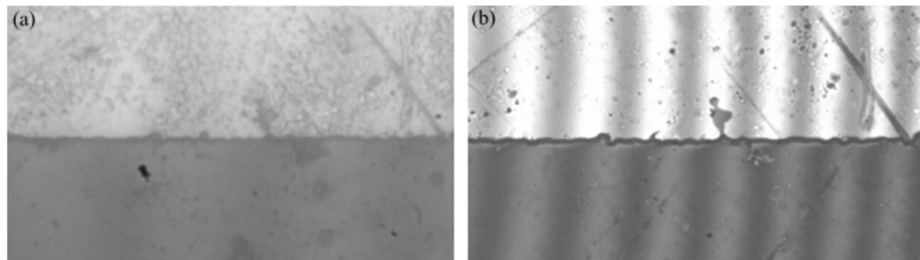


Figure 61. Comparison of fringe images of Al step on Si using red LED, ×20 immersion Linnik objectives in (a) air (0.05 step height, 26 dynamic range, $\lambda_{eff} = 640$ nm, 4579); and (b) water (0.05 step height, 25 dynamic range, $\lambda_{eff} = 640$ nm, [4580]).

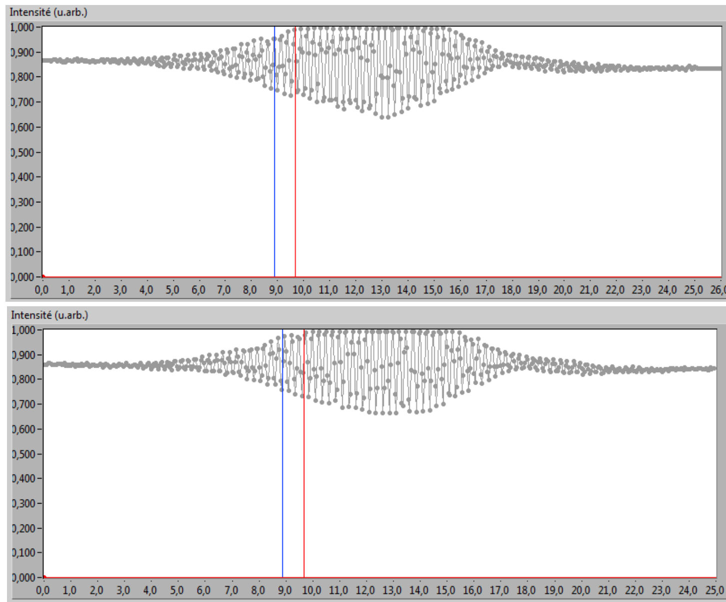


Figure 62. Comparison of raw fringe signal on Al step on Si using red LED, ×20 immersion Linnik objectives in air (top) (0.05 µm step height, 26 µm dynamic range, $\lambda_{eff} = 640$ nm, 4579); and water (bottom) (0.05 µm step height, 25 µm dynamic range, $\lambda_{eff} = 640$ nm, [4580]).

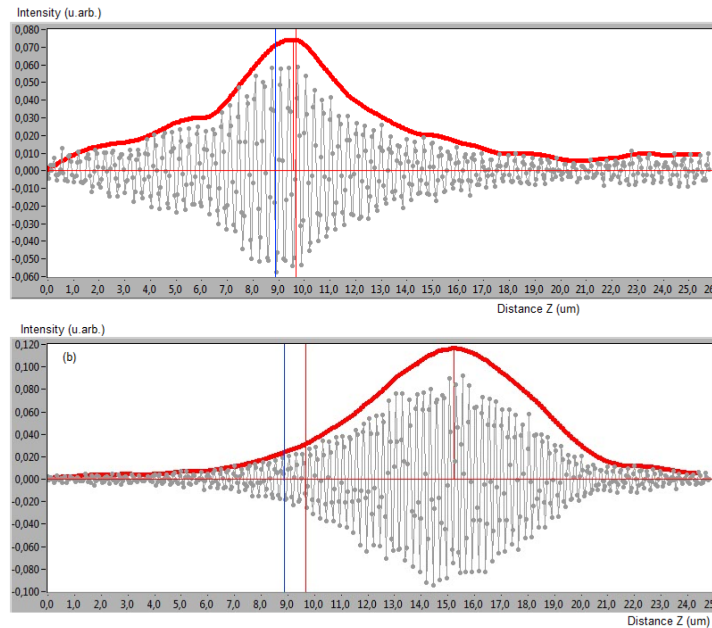


Figure 63. Comparison of fringe signals and fringe envelopes on Al step on Si using red LED, ×20 immersion Linnik objectives in (a) air (0.05 µm step height, 26 µm dynamic range, $\lambda_{eff} =$ 640 nm, rectify, 4579); and (b) water (0.05 µm step height, 25µm dynamic range, $\lambda_{eff} =$ 640 nm, FSA interpolation, [4580]).

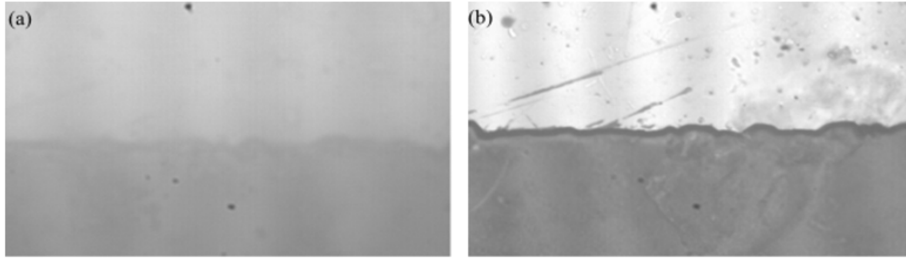


Figure 64. Comparison of fringe images of Al step on Si using red LED, ×40 immersion Linnik objectives in (a) air (0.05 µm step height, 21µm dynamic range, $\lambda_{eff}$ = 640 nm, 4584); and (b) in water (0.05 µm step height, 18 µm dynamic range, $\lambda_{eff}$ = 640 nm, [4585]).

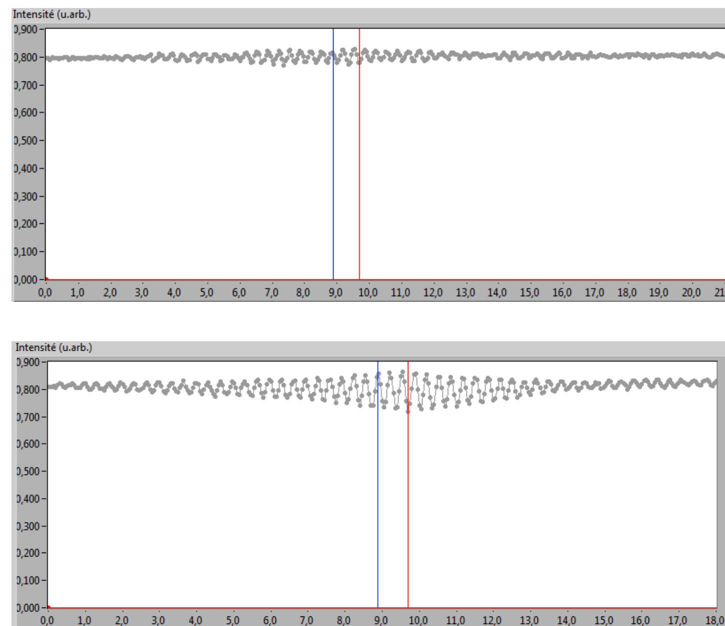


Figure 65. Comparison of raw fringe signals on Al step on Si using red LED, ×40 immersion Linnik objectives in air (top) (0.05 µm step height, 21 µm dynamic range, $\lambda_{eff}$ = 640 nm, 4584); and water (bottom) (0.05 µm step height, 18 µm dynamic range, $\lambda_{eff}$ = 640 nm, [4585]).

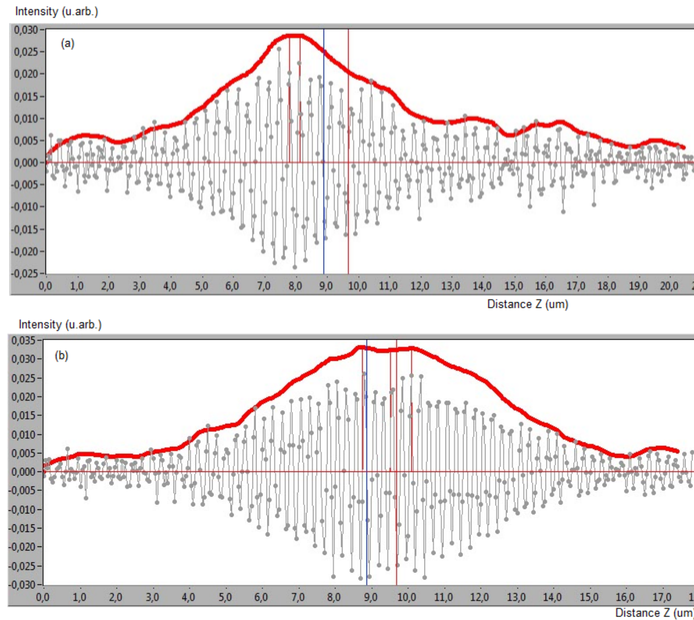


Figure 66. Comparison of fringes signals and fringe envelopes on Al step on Si using red LED, ×40 immersion Linnik objectives in (a) air (0.05 µm step height, 21 µm dynamic range, $\lambda_{eff}$ = 640 nm, FSA interpolation, 4584); and (b) water (0.05 µm step height, 18 dynamic range, $\lambda_{eff}$ = 640 nm, FSA interpolation, [4585]).

The results of the images made in water (Figure 61 and Figure 64) show fringes with higher contrast and images of the sample that are sharper than those made in air. The comparisons of the raw fringe signals (Figure 62 and Figure 65) and the fringe envelopes (Figure 63 and Figure 66) also show the improvement. These results confirm the correct functioning of the immersion objectives in water which reduce the effects of aberrations when imaging in air.

Continuing results of image processing on Al step on Si, the 3D results of measurements in air and water on the Al step on Si are shown in Figure 67 for the ×20 objective and in Figure 68 for the ×40 objective. These results show lower values of measured roughness in the 3D images from the measurements in water compared with those made in air due to the improvement in fringe contrast and sharper image details in water.

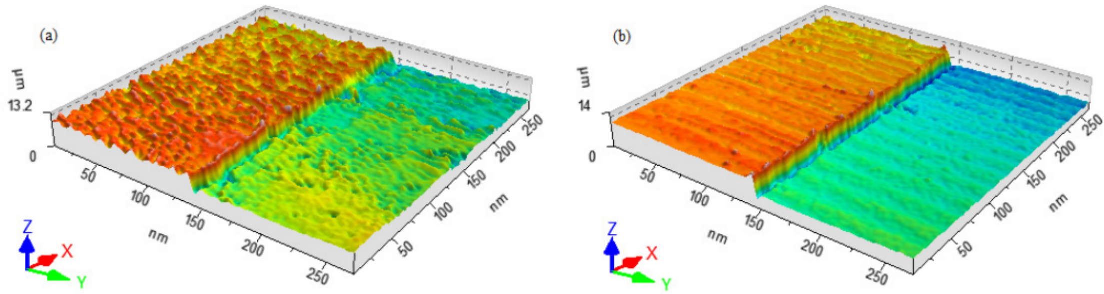


Figure 67. Comparison of 3D images of Al step on Si using red LED, ×20 immersion Linnik objectives in (a) air (0.05 µm step height, 26 dynamic range, $\lambda_{eff} = 640$ nm, rectify, 4579); and (b) water (0.05 µm step height, 25 dynamic range, $\lambda_{eff} = 640$ nm, FSA technique [4580]).

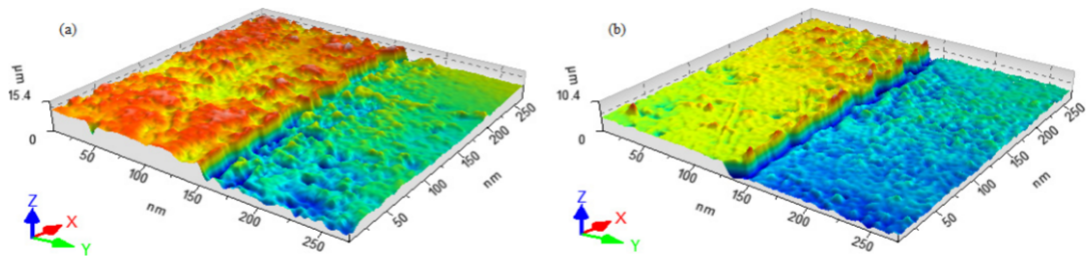


Figure 68. Comparison of 3D images of Al step on Si using red LED, ×40 immersion Linnik objectives in air (top) (0.05 step height, 21 dynamic range, $\lambda_{eff} = 640$ nm, 4584); and water (bottom) (0.05 step height, 18 dynamic range, $\lambda_{eff} = 640$ nm, [4585]).

The step height profiles in Figure 69(a) and (b) and Figure 70(a) and (b) are obtained from the height images at the lines indicated in Figure 69(c) and (d) and Figure 70(c) and (d). The lateral resolutions of the 20x and 40x objectives are determined by analyzing the slopes of the line profiles of the steps. They are estimated by taking the lateral distance between the 10% and 90% values of the total step heights. The theoretical lateral resolutions of the 20x and 40x objectives in water using the red LED are 0.78 µm and 0.48 µm, respectively. The measured lateral resolutions (ΔX) for the x20 objective are 0.6 µm in air and 0.5 in water whereas for the 40x objective these values are 0.6 µm and 0.4 µm respectively. These results demonstrate that the lateral resolution of the measurements of the sample made in water are better than those made in air.

Concerning the height measurements of the steps (ΔZ), these can also be determined from Figure 69 and Figure 70. For the ×20 objective, ΔZ is 2.71 µm in air and 2.54 µm in water. For the ×40 objective the values are respectively 2.49 µm and 2.60 µm. Measurements made on a different interference microscope (Leitz-Linnik ×50 objective in air) show the step height to be 2.5 – 2.7 µm, with an average value of 2.6 µm. The

measurements made using the immersion objectives are therefore more accurate when measured in water than in air.

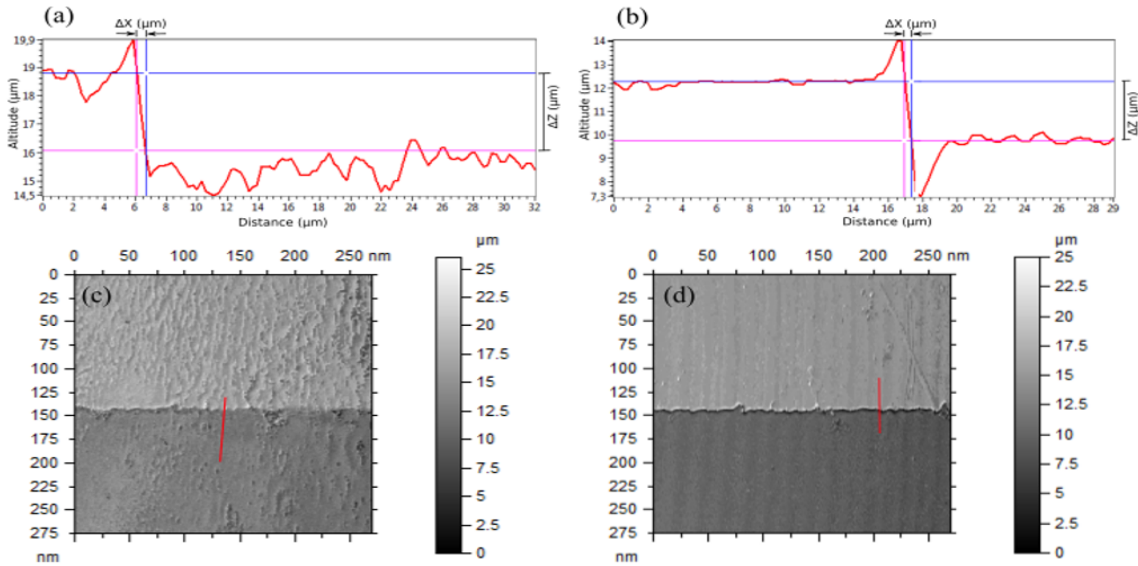


Figure 69. Comparison of the line profiles of the measured height of the Al step on Si using red LED, ×20 immersion Linnik head in air (shown in (a) and (c)) and in water (shown in (b) and (d)). The measurements of the step height (ΔZ) of the sample are 2.49 µm (0.05 step height, 25 dynamic range, $\lambda_{eff}$ = 640 nm, FSA interpolation, [4580]).

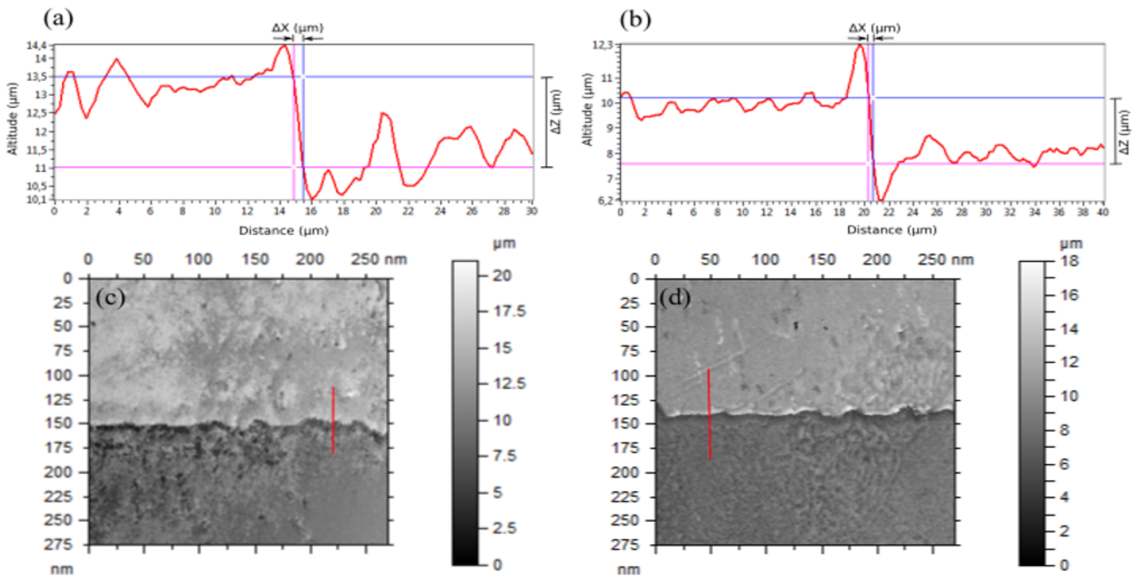


Figure 70. Comparison of line profiles of the measured height of the Al step on Si using the 40x immersion Linnik head in air (shown in (a) and (c)) and in water (shown in (b) and (d)). The measurements of the step height (ΔZ) of the sample are 2.49 µm ) (0.05 step height, 18 dynamic range, $\lambda_{eff}$ = 640 nm, [4585]).

#### 3.3.3.3.2 Measurements with reference arm compensation

As reported previously in section 3.3.3.2, the advantages and disadvantages of the experimental preparation using SPA and PDMS have been described. In this section, we present the measurement results using these elastic polymers for measuring the samples in water. The polymer is placed between the reference mirror and the reference objective. Figure 71 shows the reference objective focused on the reference mirror using each polymer with the ×20 objective, scratches and marks on the reference mirror being visible that help in focusing the reference objective.

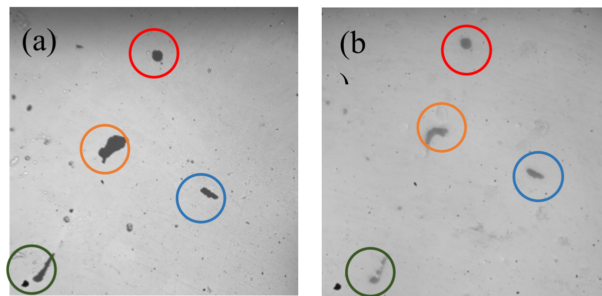


Figure 71. Focus of the reference objective on reference mirror. An elastic polymer of (a) SPA and of (b) PDMS is placed between the reference mirror and the objective

It can be seen that the SPA polymer gives a sharper image of the reference mirror than that using the PDMS slab. This may be due to an inaccuracy in the PDMS thickness or to the polymer being slightly translucent and diffusing the light. In the case of using the SPA, it is not necessary to cut it with such a high accuracy of thickness. On the other hand, SPA will break due to the pressure between the objective and reference mirror if it is too thick. To test the use of the polymers in the reference arm, measurements were made on a silicon sample having a series of numbered etched squares of different sizes. This sample consisting of a silicon wafer with a pattern made by marking with a fractal, multi-scale photolithographic mask and etching.

However, these two polymers are able to provide the surface profiling results as shown in Figure 72 and Figure 73. These results show that the measurements using SPA for reference arm compensation are more accurate and less noisy than those using PDMS compensation.

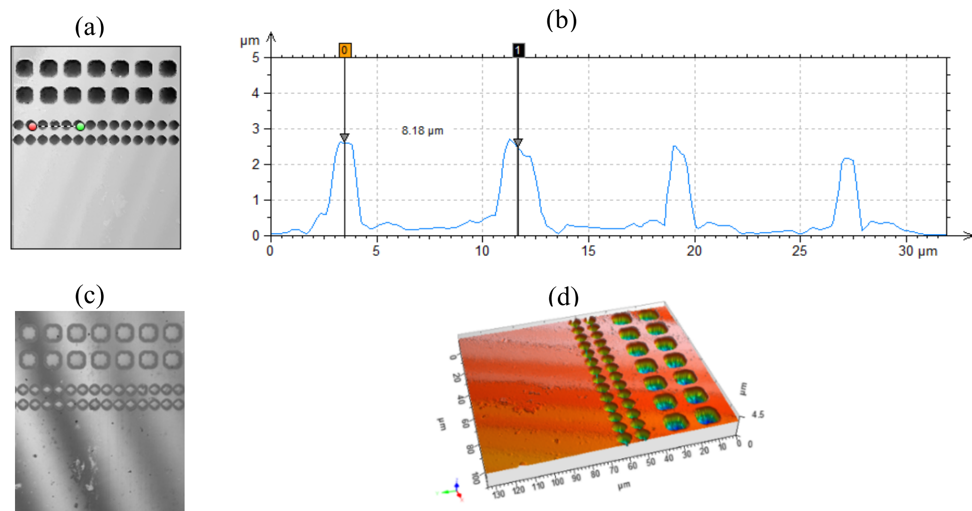


Figure 72. Etched squares in silicon, 8 µm wide and 2.5 um deep measured with the ×40 water immersion Linnik system (NA=0.8, $\lambda_{eff}$=450 nm) with SPA placed in the reference arm showing (a) height image, (b) line profile from (a), (c) fringe image and (d) 3D image.

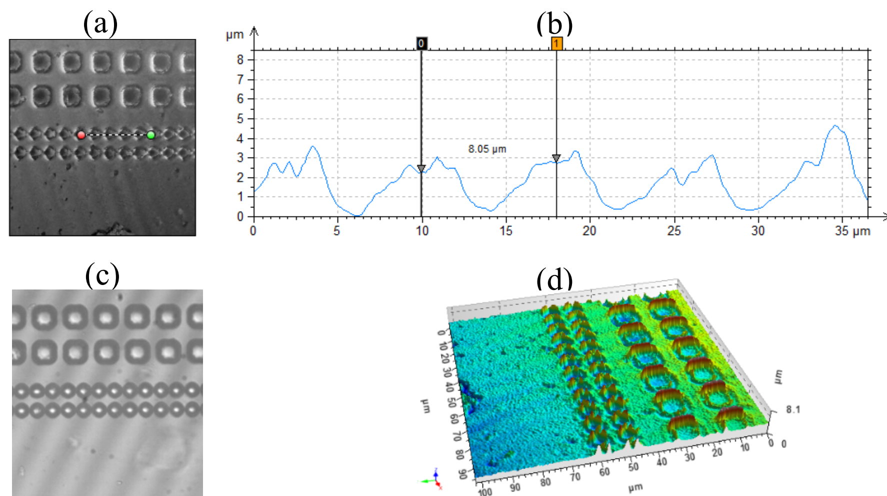


Figure 73. Etched squares in silicon, 8 µm wide and 2.5 um deep measured with the ×40 water immersion Linnik system (NA=0.8, $\lambda_{eff}$=450 nm) with 3.25 mm thickness of PDMS placed in the reference arm showing (a) height image, (b) line profile from (a), (c) fringe image and (d) 3D image.

The first measurements carried out with Aluminum step on Silicon performed using the new immersion polymer compensated Linnik head are now presented using water in the sample arm and SPA in the reference arm. The images of the fringes, raw fringe signal, fringe envelope, and line profile obtained are respectively shown in Figure 74 to

Figure 76 using the ×20 objective. Measurements at a point along the optical axis show $\lambda_{eff}$ of the white LED light source in water to be 450 nm.

As previously stated, utilization of SPA might be crushed by pressure when putting and adjusting it between the reference mirror and reference objective in the reference arm, so as it should be careful in the adjustment process. Moreover, the water bead must be removed after the experiment when it is no longer used in the same day. Otherwise its size will shrink, dry up and harden over time and temperature. The hardened water bead will stick to the mirror and probably cause damage to the mirror when forcibly removed.

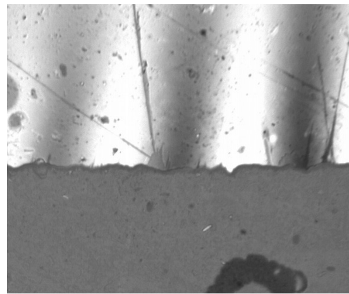

Figure 74. Fringe image of Al step on Si using white light, ×20 immersion Linnik objectives in water (0.05 µm step height, 12 dynamic range, $\lambda_{eff} = 640$ nm, [4634-5]).

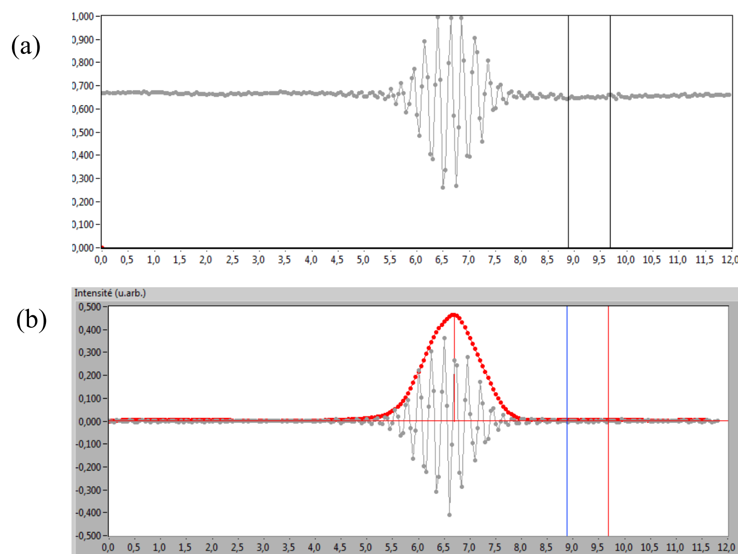


Figure 75. (a) The raw fringe signal and (b) the fringe envelope on the Al step on Si using white light, ×20 immersion Linnik objectives in water (0.05 µm step height, 12 dynamic range, $\lambda_{eff} = 640$ nm, [4634-5]).

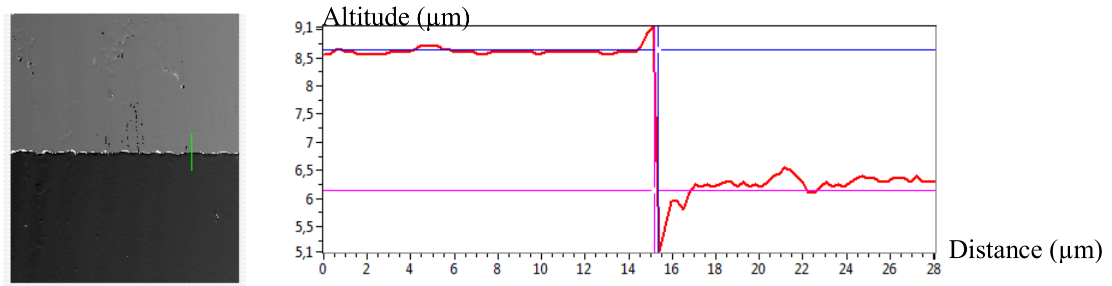


Figure 76. Line profile of the measured height of the Al step on Si using ×20 immersion Linnik objectives with white light in water (0.05 µm step height, 12 dynamic range, $\lambda_{eff}$ = 640 nm, [4634-5]). The step height of Aluminum on Silicon (ΔZ) and the measured lateral resolution (ΔX) are 2.50 µm and 0.2 µm respectively.

The result of these experiments is that the use of SPA in the reference arm provides a convenient solution for path length compensation. Compared to PDMS, SPA is able to provide better fringe contrast and better profiling results. In addition, it is easy to obtain and is quicker for finding the focus of the reference objective. In contrast, while sturdier than SPA, the use of PDMS leads to a degradation in the quality of the results (Figure 73), which requires further studies to see if it could provide a satisfactory solution.

The first results of measurements without reference arm compensation and with compensation have been presented. The first results without compensation were carried out by comparing the measurements of the edge of an aluminium layer on Si using immersion objectives in water and in air. The results of measurements on the same sample and on etched squares in Si with compensation were than carried out using SPA and PDMS. Both elastic polymers provide compensation of water in the reference arm, but the first results show that the SPA provides better results than the PDMS.

### 3.3.4 Linnik using motor in mirror arm

In the previous Fogale system, adjustment of the displacement of the reference mirror arm in order to reach zero OPD with the sample arm was conducted by using a manual linear stage. This manual adjustment takes a certain amount of dexterity and time to first find the fringes. Once the fringes are found, the process of optimization is fairly straightforward. Marking the position of the linear stage for zero OPD and the obtaining of fringes makes it easier to subsequently find the fringes.

To overcome this problem, replacement with a motorized linear stage controlled by an algorithm with the computer would allow to facilitate searching the fringe position (zero OPD) by controlling the motor motion.

This section describes the installation of a motorized stage in the reference arm for automatic path length adjustment. Details of the control added to the software are also presented for controlling the motor motion.

### 3.3.4.1 Introduction

The stage chosen is made of steel (model MFA-PP from Newport, data sheet is in Annex 7) and has a precision of 0.1 µm minimum incremental motion and excellent stability and stiffness. Its 25 mm travel range is more than enough to adjust the displacement. Other features are 0.3 mm/s maximum speed, 50 N load capacity, a backlash compensated leadscrew of drive mechanism, and equipped with micro step driver (1 full step = 0.485µm).

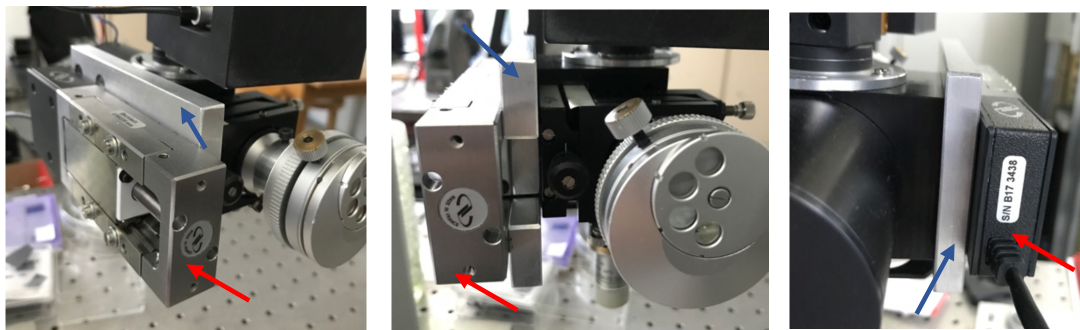


Figure 77. Motorized control installed on block of the reference arm for adjusting the path length or reference arm. Images viewed in three sides are marked by red arrows (motor) and blue arrows (adapted plate).

The movement of the motor is controlled by an NSC200 controller, with 0.1 µm minimum incremental motion and 0.33 mm/s maximum speed. Figure 77 shows the installation of the motorized stage on the reference arm.

### 3.3.4.2 Description of motor control software

Figure 78 shows the user interface and Figure 79 shows the flow-work of it. The difficulty of finding the fringe position is micrometer-scaled shifting on reference arm. The utilization of stepper motor provides ease in moving the reference arm to find the fringes. An interface software under LabView (Figure 78) was created for controlling the movement of the stepper motor. The resolution of shifting is 0.0001 µm. The speed of movement can be configured according to setting requirement in range of 0.1 – 0.00001 µm.

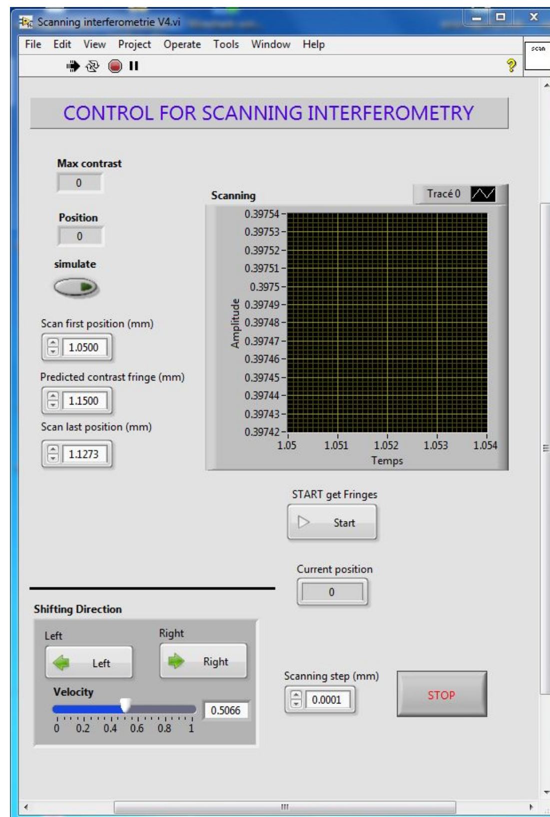


Figure 78. Graphic user interface for controlling the stepper motor (created by Husneni Mukhtar & Christophe Hoffman, IPHC).

To control the motor driver, LabVIEW carries out the workflow that is shown in Figure 79. The initialization of the motor detects the motor driver and moves it to the home position. Then the motor can be manually adjusted to move the stage to the predicted fringe position. The features of the interface provide fast and slow shifting for movements to the left and right directions.

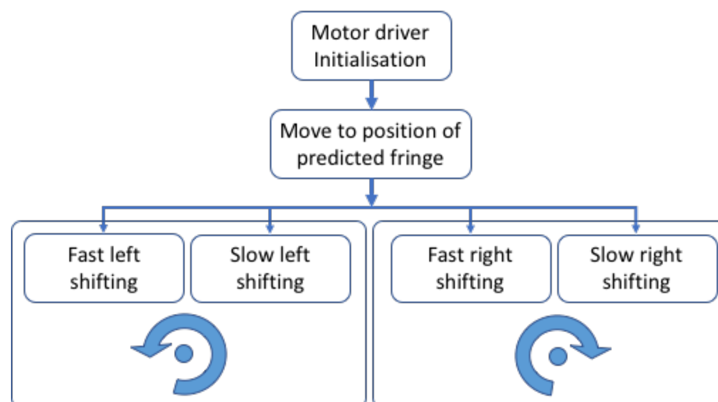


Figure 79. Flow-work of the interface for controlling the motorized stage in the reference arm.

### 3.3.4.3 Measurement tests of the motorised stage

To test the microscope after installing the stepper motor, some measurements were performed. The results in Figure 80 show one of the measurements of a sample of etched Silicon (grating pattern) in water using the white light LED, the ×20 immersion Linnik, and scanning images captured by the CMOS camera (Photonfocus).

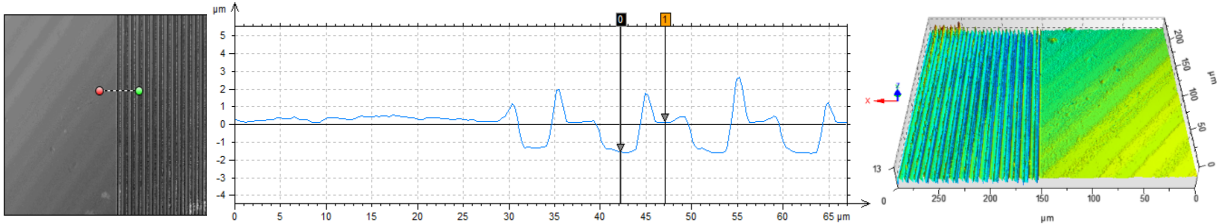

Figure 80. Results of measuring an etched silicon grating sample in water using the ×20 immersion Linnik Fogale microscope with the white light LED after motorized positioning of the OPD, showing the altitude image, a line profile and the 3D results [4701-4].

The results showed that the stability of the microscope after installing the stepper motor was sufficient for performing measurements and remained as in the previous conditions with the manual positioner.

## 3.4 Comparison of measurements using water-immersion Linnik Fogale and other microscopes

In this section, we compare the measurements of different samples made on the immersion Linnik Fogale system (×20 immersion, white LED light, in water) and those made on other microscopes in air: a commercial Zygo interference microscope ( ×50 Mirau, in air), AFM in air and the Leitz-Linnik microscope. The specification of these microscopes are shown in Table 11 [59]. SPA and water are the media used in the reference arm and sample arm respectively. The results are first presented and then discussed in section 3.5.

Table 11. Specification of the comparative microscopes

| Microscope | Objective magnification | NA | Lateral resolution (μm) | Max image size (pixels) | Sample pixel size (μm) | Max FoV (μm) |
|---|---|---|---|---|---|---|
| Leitz | x50 Linnik | 0.85 | 0.45 | 1360x1024 | 0.135 | 184x138 |
| Zygo New View 7200 | x50 Mirau | 0.55 | 0.52 | 640x480 | 0.22 | 140x110 |
| Park XE 70 AFM | - | - | 0.012 to 0.195 | 256x256 | 0.012 to 0.195 | 50x50 |

Two types of samples were used to test the new water immersion Linnik system. The first was an etched silicon wafer [108] with some patterns made using a mask with UV

photolithography and RIE etching. The second was a colloidal sample of alumina consisting of a chemical compound of aluminum oxide (Al2O3). The alumina compound was mixed in water and placed on the surface of a glass plate, and then allowed to dry. Different alumina concentrates i.e. 1 g/l, 2.9 g/l, and 14 g/l, were made to observe the distribution of alumina in suspension and the size of the alumina aggregates.

***Etched Silicon samples***

**1. Patterned etched silicon wafer hole area-1** [108]

Figure 81 shows the results of measurement of the pattern of squares etched in silicon with the similar range for or all microscopes while Table 12 shows the measurement values of the three microscopes. The width and depth of the valley are around 18 µm and 2.8 µm for all microscopes in the same area of the sample surface.

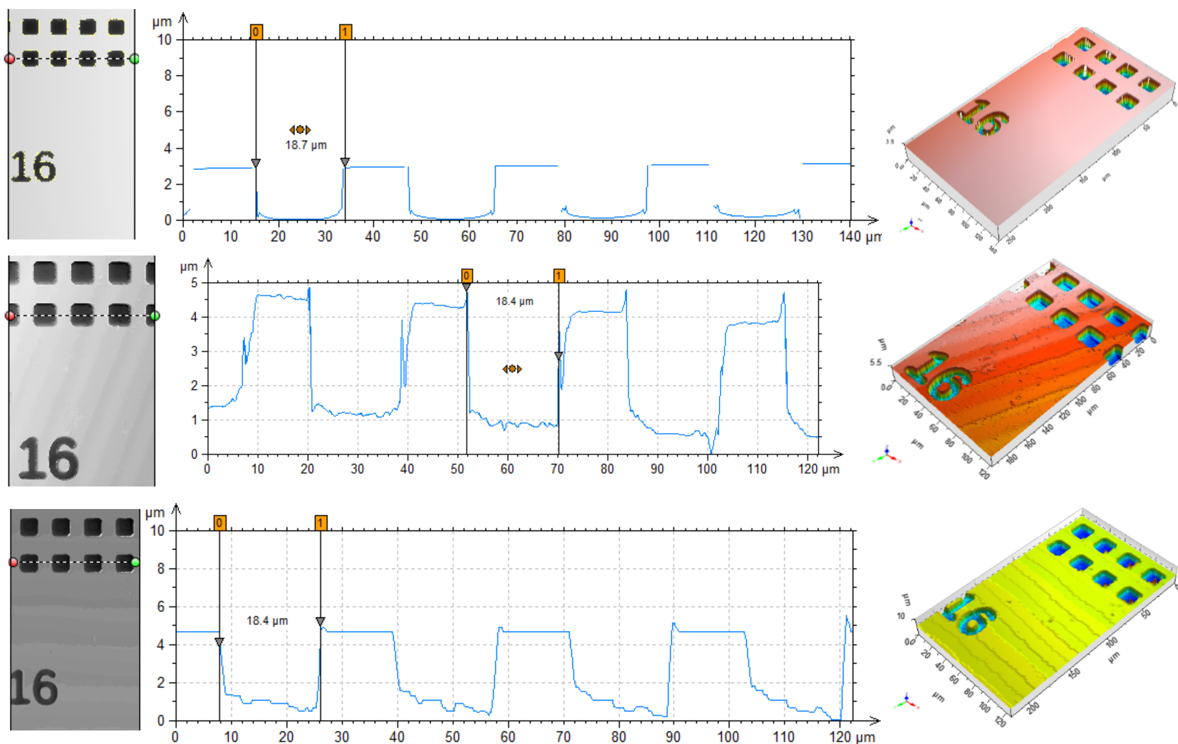


Figure 81. Etched Silicon hole area-1, is measured by: (first row) the Zygo microscope in air (×50 Mirau, NA=0.55); (second row) the Fogale Linnik water immersion system (×40, NA=0.8, 0.056 µm step height, 5.5µm dynamic range, $\lambda_{eff}$=450 nm, [4721]); and (third row) the Fogale Linnik water immersion system (×20, NA=0.5, 0.056 µm step height, 10 µm dynamic range, $\lambda_{eff}$=450 nm, [4637]).

Table 12. Comparison of measurements of etched silicon area-1 using each microscope

| Microscopes | Measurement of valley (µm) | | | |
|---|---|---|---|---|
| | Area-2 | | Area-3 | |
| | Width | Depth | Width | Depth |
| Zygo NewView 7200 commercial microsope, ×50 Mirau | 12.6 | 2,74 | 8.09 | 2.22 |
| Immersion Fogale, ×40 Linnik | 12.5 | 2.75 | 8.03 | 2.42 |
| AFM (Park XE70) non-contact mode | - | - | 8.61 | 2.27 |

## 2. Patterned etched silicon hole area-2 and area-3

Figure 82 shows the results of measurement with the similar range for all microscopes while Table 13 shows the measurement values of the three microscopes. The width and depth of the valley for hole area-2 and hole area-3 are around 12 µm and 2.75 µm and 8 µm and 2.2 µm for all microscopes in the same area of the sample surface. The raw signal and the envelope interferogram images are shown in Figure 83.

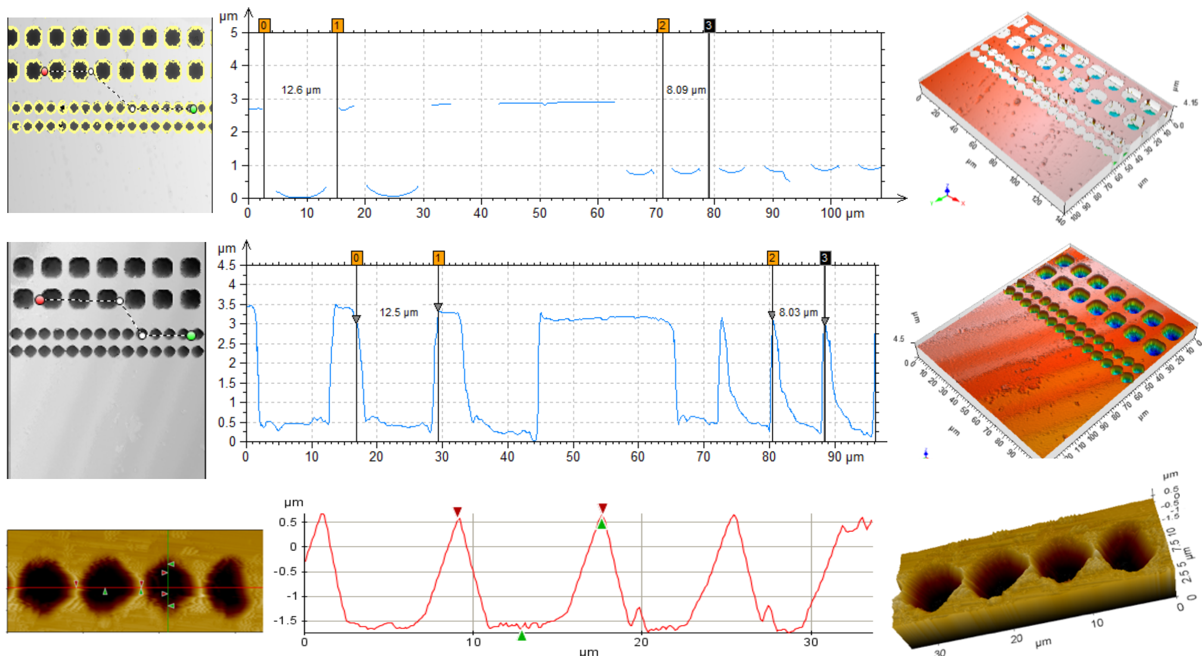


Figure 82. Etched Silicon hole area-2 and area-3, measured by (first row) the Zygo microscope in air (×50 Mirau, NA=0.55,); (second row) Fogale Linnik water immersion system (×40, NA=0.8, 0,056 µm step height, 4.5µm dynamic range, $\lambda_{eff}$=450 nm, [4721]); and (third row) AFM non-contact mode.

Table 13. Comparison of measurements of etched silicon area-2 and area-3 using each microscope

| Microscopes | Measurement of valley (µm) | |
|---|---|---|
| | **Width** | **Depth** |
| Zygo NewView 7200 commercial microsope, ×50 Mirau | 12.10 | 2.09 |
| Immersion Fogale, ×40 Linnik | 12.00 | 2.00 |
| AFM (XE Park) non-contact mode | 12.33 | 2.19 |
| Immersion Fogale, ×20 Linnik | 12.10 | 2.10 |

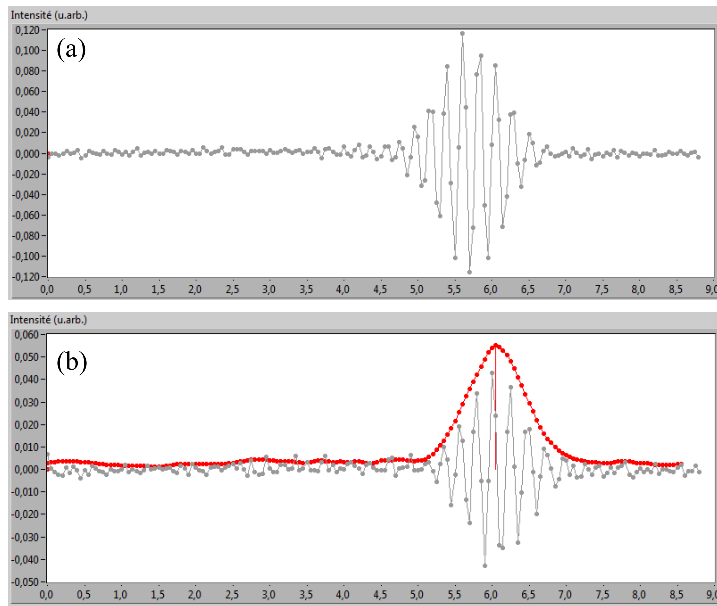


Figure 83. (a) The raw fringe signal and (b) the fringe envelope on the etched silicon sample no.16 h-3 using the Fogale immersion Linnik with the ×20 immersion objective and the white LED (0.05 µm step height, 9 dynamic range, $\lambda_{eff}$ = 450 nm, [4667a]).

### 3. Patterned etched Silicon

Figure 84 shows the results of measurement of patterned etched silicon with the similar range for or all microscopes while Table 14 shows the measurement values of the four microscopes. The width and depth of the oval hole are around 12 µm and 2 µm for all microscopes in the same area of the sample surface.

Table 14. Comparison of measurements of etched silicon (oval pattern) using each microscope.

| Microscopes | Measurement of valley (µm) | |
|---|---|---|
| | **Width** | **Depth** |
| Zygo NewView 7200 commercial microsope, ×50 Mirau | 12.10 | 2.09 |
| Immersion Fogale, ×40 Linnik | 12.00 | 2.00 |
| AFM (XE Park) non-contact mode | 12.33 | 2.19 |
| Immersion Fogale, ×20 Linnik | 12.10 | 2.10 |

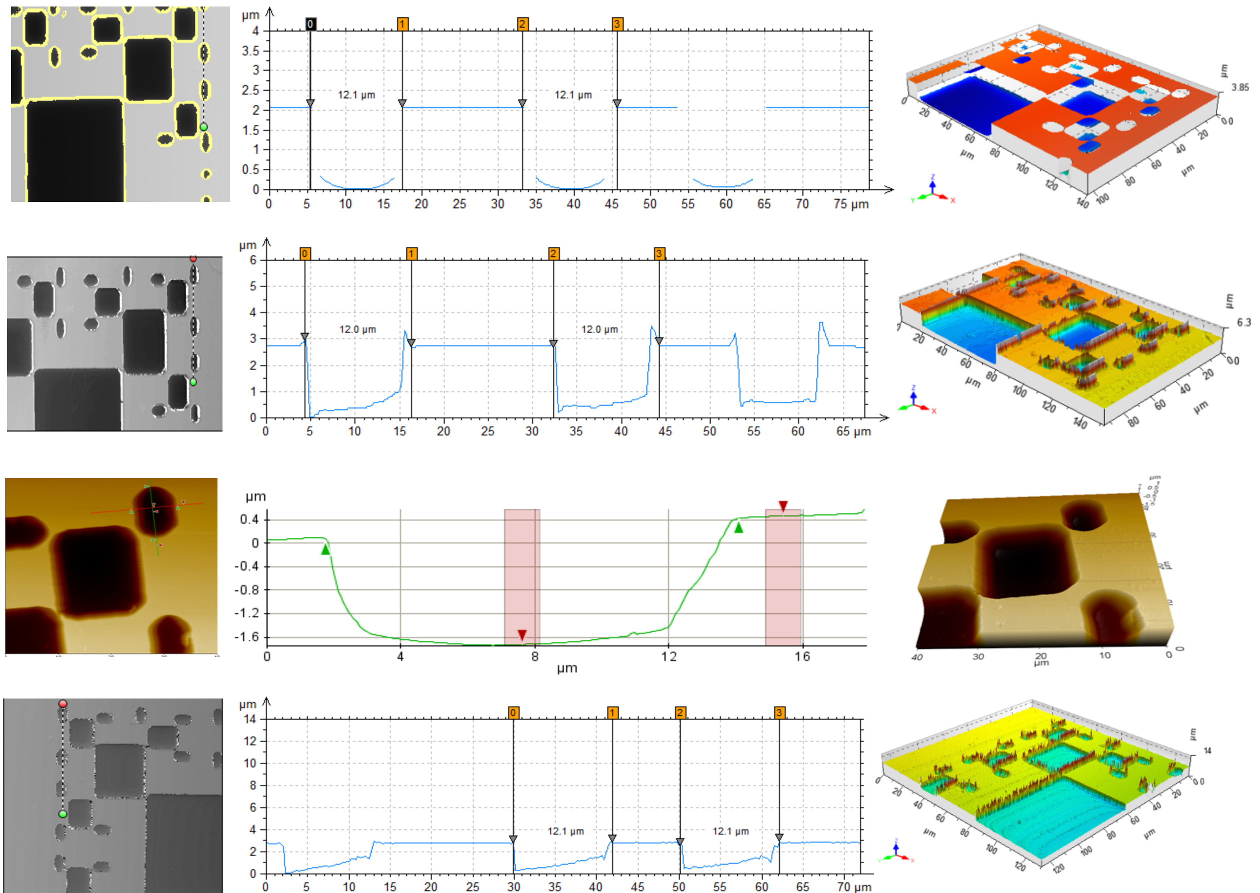


Figure 84. Etched Silicon, oval pattern, is measured by (first row) the Zygo microscope in air (×50 Mirau, NA=0.55); (second row) the Fogale immersion Linnik system in water (×40, NA=0.8, 0.056 µm step height, 6.3 µm dynamic range, $\lambda_{eff}$=450 nm, [4721]); (third row) AFM non-contact mode; and (fourth row) the Fogale Linnik immersion system in water (×20, NA=0.5, 0,056 µm step height, 14 µm dynamic range, $\lambda_{eff}$=450 nm, [4675a]).

## 4. Patterned etched Silicon (grating)

Figure 85 shows the results of measurement of the etched silicon grating with the similar range for or all microscopes while Table 15 shows the measurement values of the four microscopes. The pitch and depth valley of grating are around 10 µm and 2 µm for all microscopes in the same area of the sample surface.

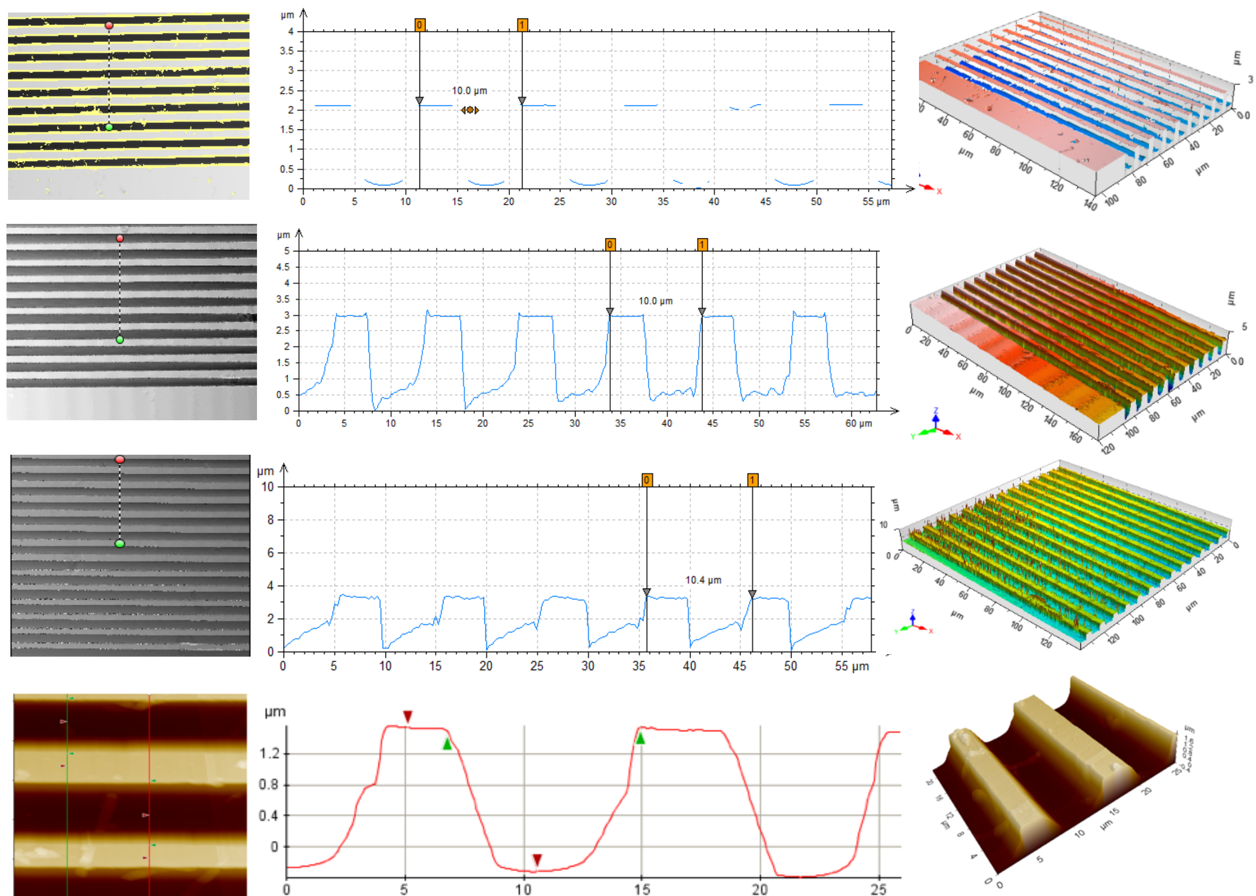

Figure 85. Etched Silicon grating pattern, is measured by (first row) the Zygo microscope in air (×50 Mirau, NA=0.55); (second row) the Fogale Linnik immersion system in water (×40, NA=0.8, 0.056 µm step height, 5 µm dynamic range, $\lambda_{eff}$=450 nm, [4721]); (third row) the Fogale Linnik immersion system in water (×20, NA=0.5, 0.056 µm step height, 10 µm dynamic range, $\lambda_{eff}$=450 nm, [4674]); and (fourth row) AFM non-contact mode.

Table 15. Comparison of measurements of etched silicon (oval pattern) using each microscope.

| **Microscopes** | **Measurement of pitch (µm)** | |
|---|---|---|
| | **Width** | **Depth** |
| Zygo NewView 7200 commercial microsope, ×50 Mirau | 10.00 | 2.06 |
| Immersion Fogale, ×40 Linnik | 10.00 | 2.15 |
| Immersion Fogale, ×20 Linnik | 10.40 | 2.10 |
| AFM (XE Park) non-contact mode | 9.51 | 1.84 |

## 5. Al on Si, 2 µm in step height

Figure 86 shows the results of measurements on the 2 µm high Al step on silicon with the similar range for or both microscopes while Table 16 shows the measurement values of the four microscopes. The step height Aluminum on Silicon is around 2 µm for both microscopes in the same area of the sample surface.

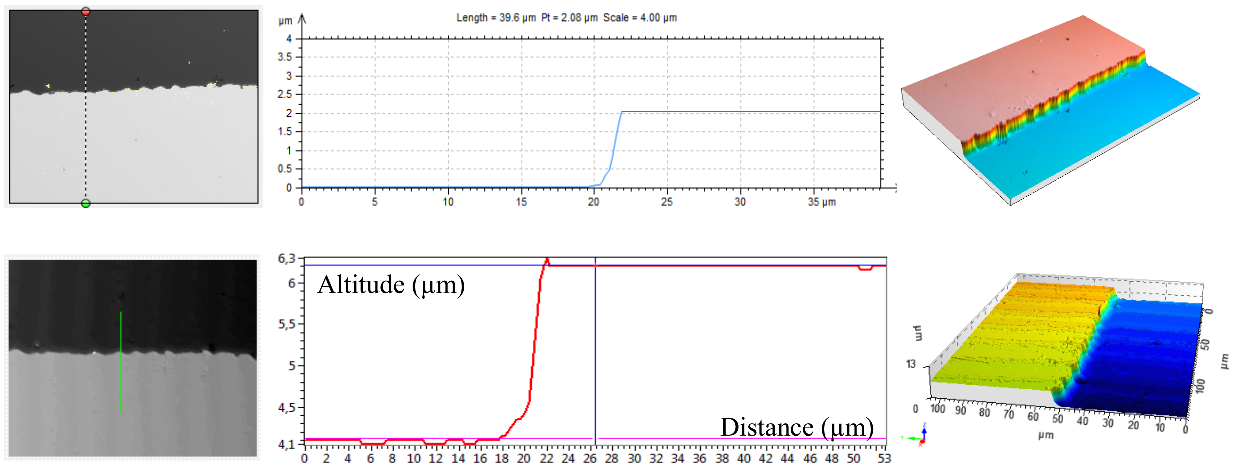


Figure 86. 2 µm high Al step on Si is measured by (first row) the Zygo microscope in air (×50 Mirau, NA=0.55); and (second row) the Fogale Linnik immersion system (×20, NA = 0.5, 0.05 µm step height, 13 dynamic range, $\lambda_{eff}$ = 450 nm, rectify, [4644]).

Table 16. Comparison of measurements of etched silicon (oval pattern) using each microscope.

| **Microscopes** | **Measurement of step height (µm)** |
|---|---|
| Zygo NewView 7200 commercial microsope, ×50 Mirau | 2.10 |
| Immersion Fogale, ×20 Linnik | 2.03 |

## 3.5 Discussion of measurement results

This section presents the analysis of the previous measurements and some of the problems found in some of the measurements during and after the modification. It will be described in several parts.

### 3.5.1 Hardware misalignment

For most of the measurement results, the Fogale Linnik immersion system performs very well in comparison to the other microscopy techniques, giving similar widths and depths of the various structures tested. It also shows the improved lateral resolution due to operation in a water medium. Nonetheless, a slight "batwing" effect can be observed on some of the results (Figure 85, second and fourth rows; Figure 86, second row).

A more significant artifact was observable in some of the measurements, particularly on the vertical straight edges ("vertical" meaning as viewed on the page) which appeared to be sloping on one side and not on the other. This can be observed in Figure 85 (second row) for the Fogale immersion Linnik system in water with the ×40 objective on the etched squares in silicon, where the line profile clearly shows different slopes. The Zygo and AFM results show similar slopes on each side of the hole. On the contrary, horizontal straight edges ("horizontal" meaning as viewed on the page) do not display this effect.

After visually observing the process of image scanning during capture with the camera, several shifts of visible lateral image could be observed by eye in one direction but not in the other. An etched grating sample was therefore positioned "vertically" and a series of images captured while scanning over a depth of 5 µm. The results are shown in Figure 87. Line profiles from a series of successive images clearly show a lateral displacement of the sample during scanning. These shifts are most likely due to the misalignment of the microscope in one axis in the vertical direction.

Such a misalignment could explain the difficulty in obtaining the best fringe contrast in certain measurements. A first solution was tested, consisting of mounting the sample on a manual goniometric stage, and inkling the sample in one direction. New measurements of the fringe intensity showed more easily obtainable fringes and an improvement in the fringe contrast. In a first instance, fixing the misalignment mechanically was much more difficult to implement. Another solution was to correct the image positions in one direction after image acquisition.

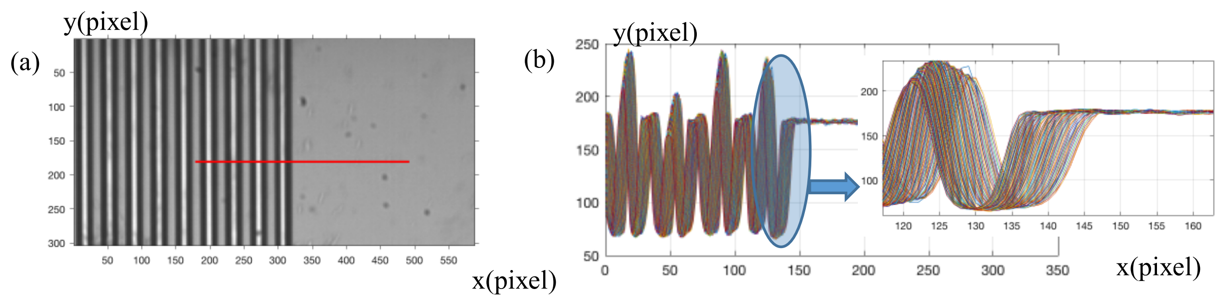


Figure 87. Illustration of the problem of lateral image displacement during axial scanning over a dynamic range of 5 µm using the x20 immersion Linnik: (a) measured area of displacement test; (b) Line profile of the measured area on a stack of scanned images, with a zoom of a specific area.

This first required measuring the image shift as a function of axial displacement. A flowchart for illustrating the procedure is shown in Figure 88. The software of "Image displacement analysis for CSI scanning" was developed in Matlab to correct those images, as shown in Figure 89.

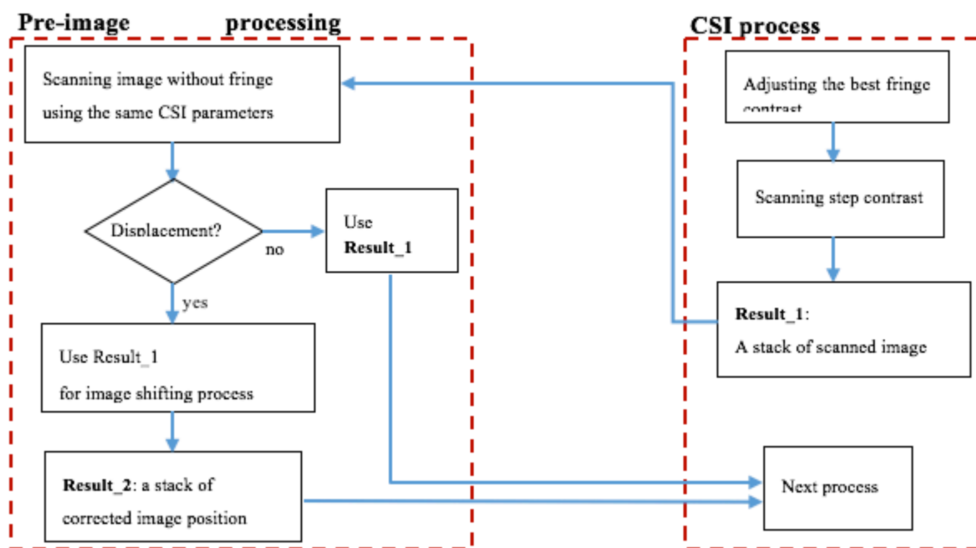


Figure 88. Flowchart of proposed technique to measure the displacement of misalignment and to correct the image position.

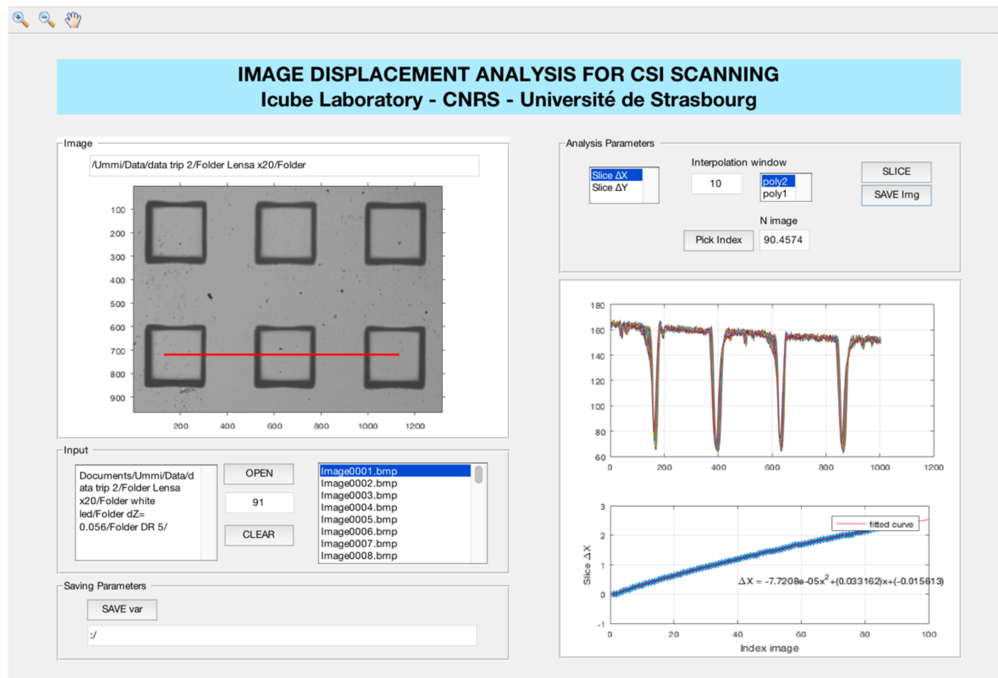


Figure 89. Interface software “Image displacement analysis for CSI scanning” for checking and correcting the position of scanned images along the x- and y-axis caused by misalignment (created by H Mukhtar).

Description of correction treatment

In order to see if the error in image shift could be reduced using certain adjustments, three possible cases were studied (detailed in Figure 90):

Case-1. Using only the reference mirror angle adjustment, without the manual goniometric stage.

Case-2. Using only the adjustment of the manual goniometric stage.

Case-3. Using the adjustment of both the reference mirror angle adjustment and the manual goniometric stage.

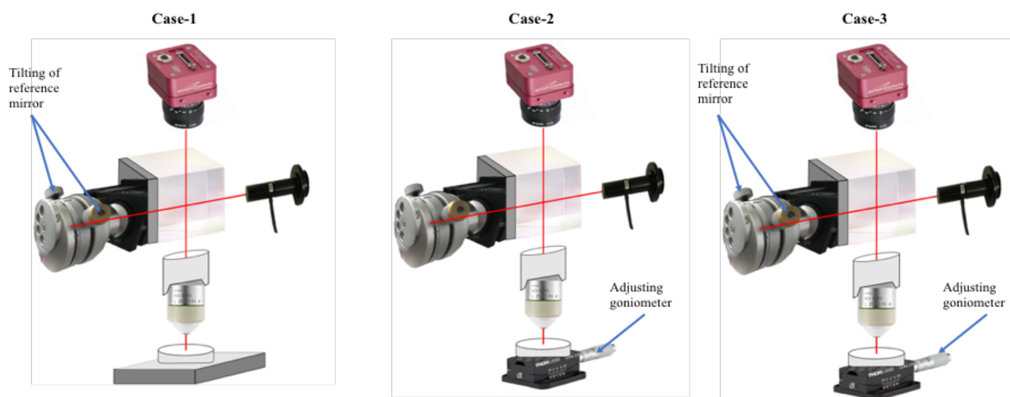


Figure 90. Description of three cases to test and observe the effect of misalignment.

To study the three cases and influence on image shift during the piezo scanning over the depth of sample, different dynamic scan ranges were tested, together with different piezo step heights objective magnifications. After studying these three cases, the shifts were still observable. Nonetheless, while in case-1, it was difficult and took time to obtain the best fringe contrast by adjusting the mirror, in case-2 and case-3, it was found to be easier.

The steps carried out are as follows:

**1. Investigating the displacement over whole images.**

A spatial correlation technique is used to measure the amount of lag spatially between two signals for each scanned image. This technique is implemented in three cases for different values of the dynamic scan range, the step height of the scanning and the objective magnification in order to obtain each displacement function, an example of which is shown in Figure 93.

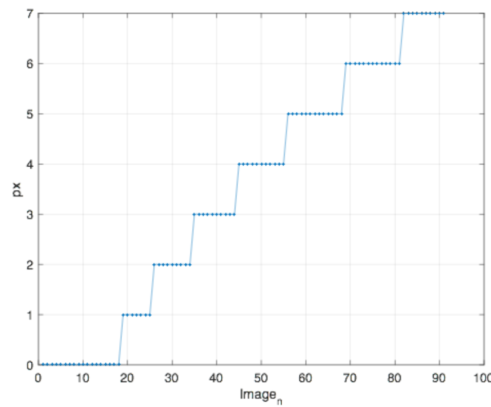


Figure 91. The lateral displacement in x in pixels between successive images over 100 steps using the cross-correlation function. The dynamic range is 5 µm, dZ = 0.056 µm, $\lambda_{eff}$= 450 nm, for the x20 immersion objective.

Using this technique, the image shifting could only be detected by units of 1 pixel of displacement over several images, resulting in a displacement of around 0.15 – 0.2 pixels per image. This is the reason why from image 1 to 18 for example in Figure 91, the shift is not detected due to the incapacity to detect fractions of a pixel. A resizing technique then should be used to improve the detection of the image shift.

**2. Improving the detection of displacement by resampling the image**

Enhancing the image by pixel resampling, so as to increase the number of and the size of the image as shown in Figure 92 is obtained by using a cubic kernel interpolation in order to be able to detect the displacement in the up-scaled images. The displacement results shown in Figure 93 demonstrate that in each case the image shift shows a similar trend and displacement range.

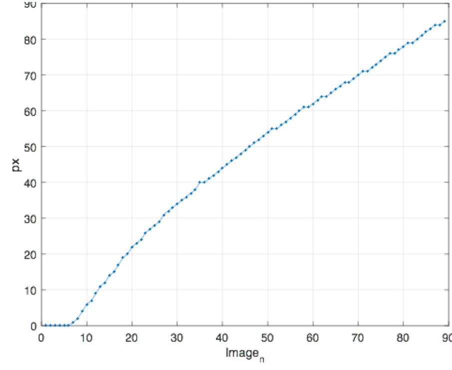


Figure 92. The shift along the x-axis between two images for each measurement using the cross-correlation function after 10× pixel resampling by a cubic kernel interpolation. Dynamic range= 5 μm, dZ= 0.056 μm, λeff= 450 nm, ×20 immersion objective.

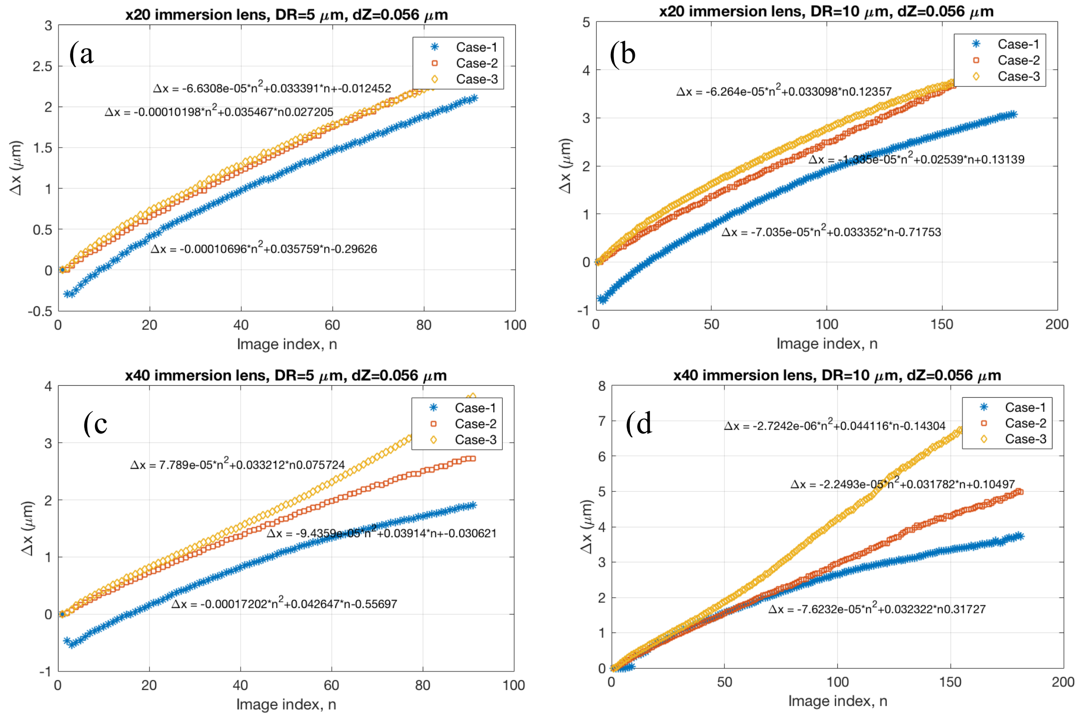


Figure 93. The shift between successive images for each scanning step for the case of the x-axis. Dynamic range = 5 μm, dZ= 0.056 μm, λeff= 450 nm for (a) ×20 immersion objective and (b) ×40 immersion objective. Dynamic range = 10 μm, dZ= 0.056 μm, λeff= 450 nm for (c) ×20 immersion objective and (d) ×40 immersion objective.

By using the following equation,

$$\overline{\Delta x} = \frac{\Delta x_n - \Delta x_{n-1}}{n-1} \qquad \text{(Eq.10)}$$

the mean values of the shift between two images in Figure 93 is mostly similar as shown in Table 17.

Table 17. Mean of the lateral shift between successive images for each case and objective magnification.

| Case-n | $\overline{\Delta x}$ (μm) | | | |
|---|---|---|---|---|
| | ×20 immersion objective | | ×40 immersion objective | |
| | DR 5 μm | DR 10 μm | DR 5 μm | DR 10 μm |
| 1 | 0.0259 | 0.0205 | 0.0268 | 0.0253 |
| 2 | 0.0261 | 0.0229 | 0.0304 | 0.0297 |
| 3 | 0.0272 | 0.0216 | 0.0272 | 0.0416 |

In addition, for a short dynamic range (2.5 μm), shown in Figure 94, the lateral image shift using the ×20 immersion objective is Δx= 0.038 μm while the total shift is Δx= 1.587 μm or 5-6 pixels. One pixel-x is equal to 0.026935 μm. Then, to check the trend of the shift based on the length variation of the dynamic range, Figure 95 confirms the continuity trend of the shift with a variation in the value of the dynamic range.

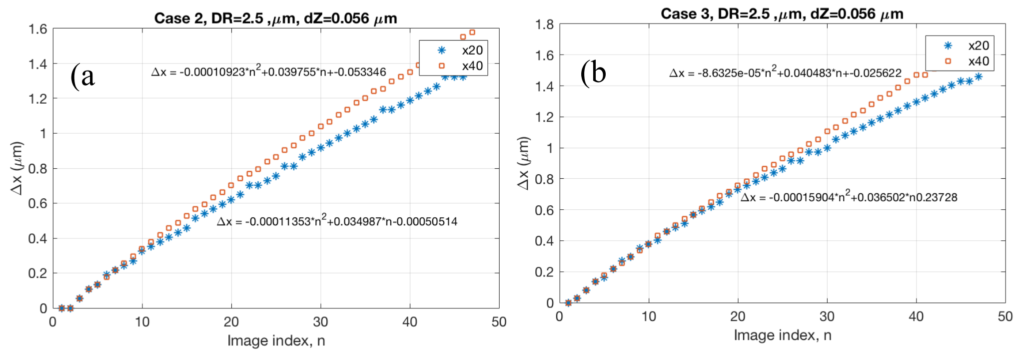


Figure 94. The lateral image shift for a short dynamic range (2.5 μm) of each objective and case.

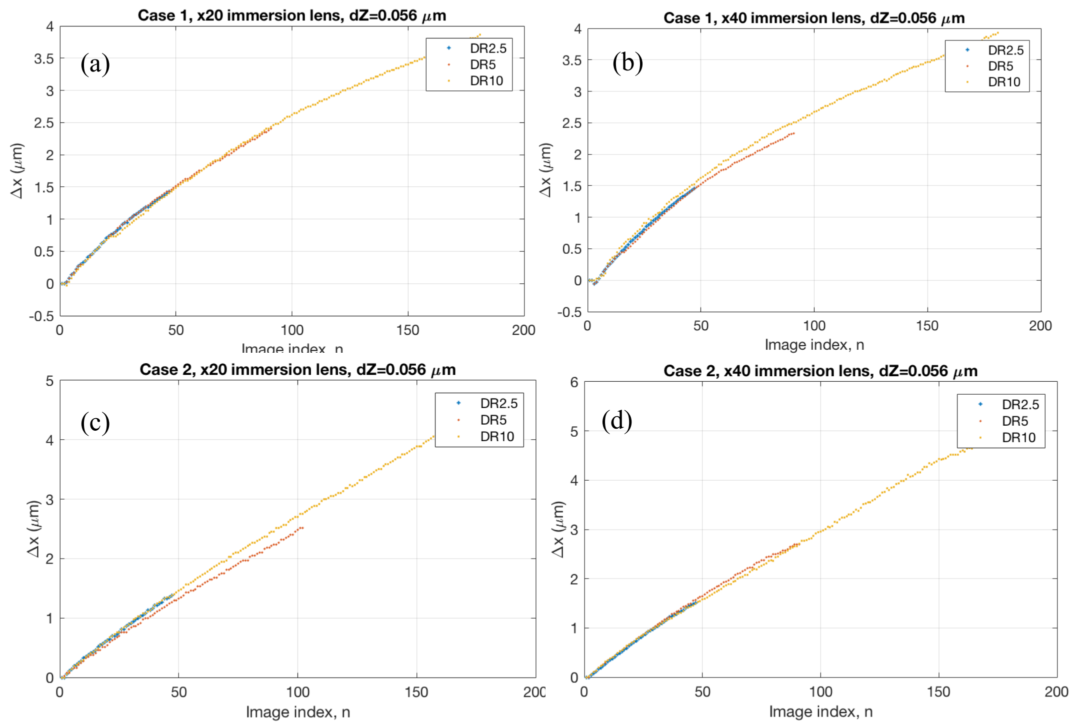


Figure 95. The continuity trend of the lateral image shift during axial scanning for larger values of dynamic range (2.5 µm, 5 µm, and 10 µm): (a),(c) using ×20 immersion objective for case 1 and case 2; (b),(d) using the ×40 immersion objective for case 1 and case 2.

A study of the trend in image shift was also made for different step heights over the same dynamic range as shown in Figure 96. It can be seen that the total shift from these two tests is similar at 1.5 µm.

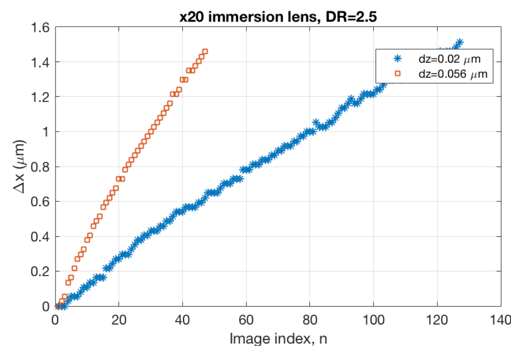


Figure 96. The shift response for different step heights (dZ) over the same dynamic range, using the ×20 immersion objective.

Similar measurements of the lateral image shift were also made along the y-axis. The results in Figure 97 show that the lateral image shift is less than 0.25 µm so that it can be neglected.

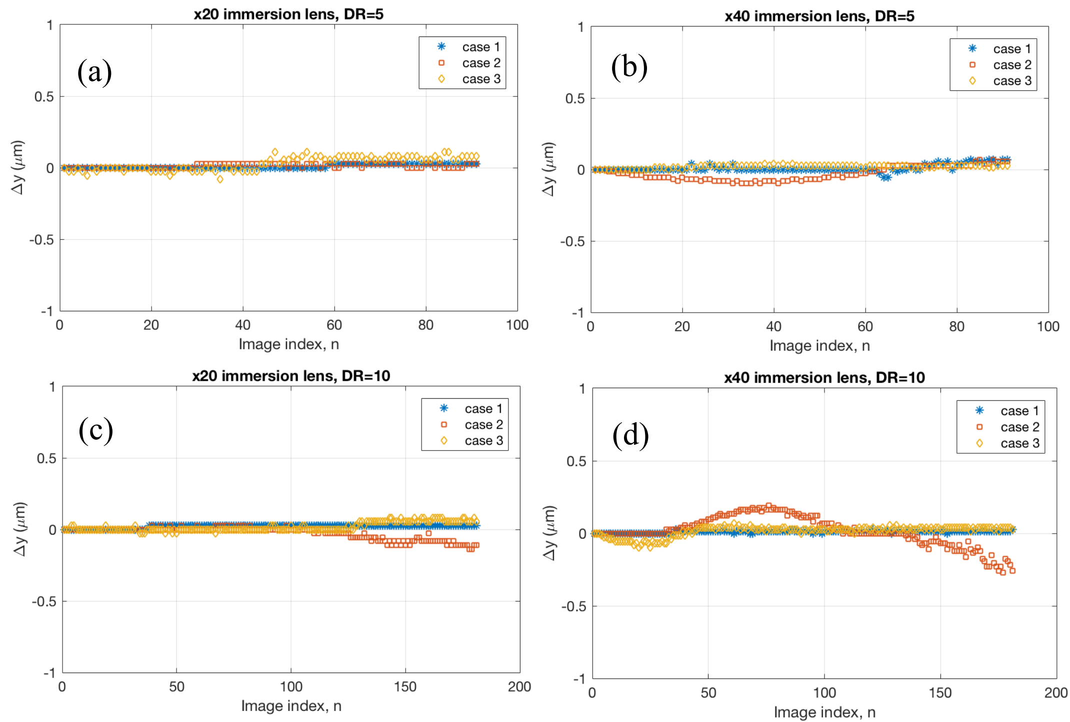


Figure 97. The lateral image shift between two images for each scanning step and cases along the y-axis. The dynamic range= 5 µm, dZ= 0.056 µm, λeff= 450 nm for (a) ×20 immersion objective and (b) ×40 immersion objective; The dynamic range =10 µm, dZ= 0.056 µm, λeff= 450 nm for (c) ×20 immersion objective and (d) ×40 immersion objective.

### 3. Image correction

The image correction technique was implemented on the whole set of resized images in order to correct the position of the details in each image based on the second procedure. This assumes that the images are spatially periodic.

### 4. Back to original size (second resizing)

After the correction process of the image position, the second resizing is performed to return them to their original size. A comparison of the corrected image (part of Result_2 in Figure 88) with the original image (part of Result_1 in Figure 88) is shown in Figure 98.

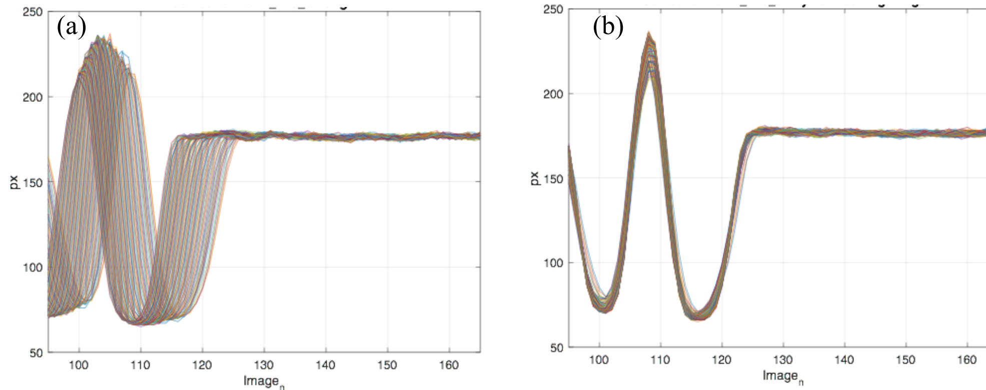


Figure 98. Successive profiles of the grating for (a) before correction of the image shift measured in the same area using the ×20 immersion objective and (b) after correction of the image shift, 10 µm dynamic range and 0.056 µm step height.

Finally, we can make the following important observations:

1) In all the measurement cases, it is clear that adjusting the reference mirror and goniometric stage do not significantly affect the value and trend of the lateral image shift during axial scanning.

2) For each case of different dynamic range, objective magnification, and the step height value (dZ), the shift of lateral image is similar for the x-axis.

3) There is no lateral image shift along the y-axis.

We can conclude from those observations that the lateral image shift along the x-axis is most likely caused by the vertical alignment of the microscope on the vertical optical bench and not by the piezo translation or the adjustment components.

Precise measurements can often be worsened due to mechanical movements involved in the measurement. In the case of this immerson Linnik microscope, a vertical misalignment of the microscope has been detected along the x-axis, resulting in the horizontal shifting of images during the axial scanning process. The results of this misalignment lead to a lack of the measurement accuracy in the 3D shape of surface structures perpendicular to the x-axis. To increase the measurement accuracy, a cross-correlation strategy has been applied to detect the image shift error. The acquired image stack is then corrected at the same image detail location. The cross-correlation allows the lateral shift to be measured between successive images and help to restore the images to the same location. The first image in the stack is used as the reference image. The advantage of this technique is a minimizing of the image alignment and improving the measurement accuracy by software processing.

### 3.5.2 Resolution limit and loss in resolution

The immersion Fogale microscope has red and white light LEDs available as the light sources depending on the used technique and the surface height. The centre wavelengths of the red and white light LEDs are 640 nm and 620 nm respectively. The numerical aperture (NA) of the immersion objectives are 0.5 for the ×20 objective and 0.8 for the ×40 objective.

Theoretically, the maximum lateral resolutions (discussed in sub-section 1.3) of the immersion Fogale microscope according to the Rayleigh criterion ($r_R = 0.61\lambda/NA$) are 0.78 µm and 0.49 µm for the ×20 and ×40 immersion objective respectively with red LED and are 0.76 µm and 0.47 µm for the ×20 and ×40 immersion objective respectively with white light LED. While the experimental resolutions measured using the RS-N standard calibration of SiMETRICS are 1.2 µm and 0.8 µm respectively with red LED.

Experimental resolution

A calibrated resolution standard type RS-N from SiMETRICS GmbH, as shown in Figure 99, was used to validate the microscope performance and to test the measurement resolution. This standard has a size of 10 mm x 10 mm and consists of a series of square gratings with different pitches etched in a Si wafer to depths between 140 nm to 190 nm depending on the pitch.

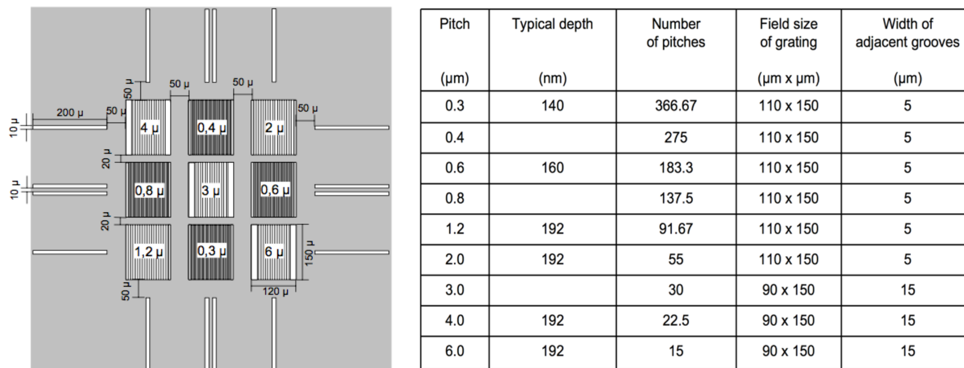


| Pitch (µm) | Typical depth (nm) | Number of pitches | Field size of grating (µm x µm) | Width of adjacent grooves (µm) |
|---|---|---|---|---|
| 0.3 | 140 | 366.67 | 110 x 150 | 5 |
| 0.4 | | 275 | 110 x 150 | 5 |
| 0.6 | 160 | 183.3 | 110 x 150 | 5 |
| 0.8 | | 137.5 | 110 x 150 | 5 |
| 1.2 | 192 | 91.67 | 110 x 150 | 5 |
| 2.0 | 192 | 55 | 110 x 150 | 5 |
| 3.0 | | 30 | 90 x 150 | 15 |
| 4.0 | 192 | 22.5 | 90 x 150 | 15 |
| 6.0 | 192 | 15 | 90 x 150 | 15 |

Figure 99. The RS-N type resolution standard consists of a set of 9 gratings with different pitch values varying from 0.3, 0.4, 0.6, 0.8, 1.2, 2.0, 3.0, 4.0 and 6.0 µm.

The PSM technique was used to measure all the gratings using the red LED. Figure 100 shows the measurements using the ×40 water immersion Linnik Fogale where the smallest periodic grating that could be seen is 0.8 µm. Hence, the experimental lateral resolution for ×40 immersion Linnik is 0.8 µm.

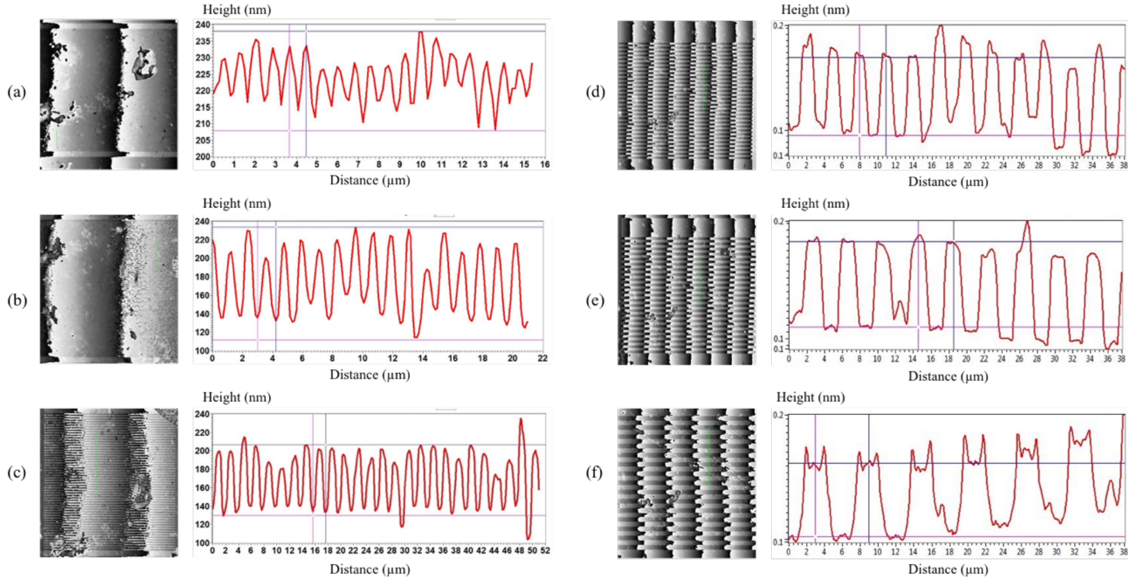


Figure 100. Measurements of the RS-N type resolution standard using the ×40 immersion Linnik objective in water with the PSM technique ($\lambda_{eff} = 505\ nm$). The grating sizes visible were (a) 0.8 µm; (b) 1.2 µm; (c) 2 µm; (d) 3 µm; (e) 4 µm; (f) 6 µm [4674b].

The reduced experimental resolution of 0.8 µm compared with the theoretical value of 0.47 µm might be caused by several reasons:

1) optical aberrations

2) the diameter of the light source being such that the light rays do not fill the entrance pupil of the objective

3) a difference in focus positions of the two objectives on the reference mirror and sample so that the angles of the incident beams and reflected beams are not the same.

# 3.6 Conclusion

This third chapter has presented the work carried out to modify the Fogale microscope for working in the immersion Linnik configuration. The main challenges of this arrangement have been overcome, namely balancing the dispersion mismatch on both arms and finding the fringes at zero OPD by motorised adjustment of the reference arms.

In the system used, the reference mirror arm is mounted horizontally, making liquid immersion tricky. In this work, we have investigated alternative solutions based on non-liquid elastic polymers placed between the end of the objective and the reference mirror using sodium polyacrylate (SPA) beads and PDMS (polydimethylsiloxane) slabs, with a refractive index very close to that of water. The results of the performance tests of the modified system have been presented and demonstrated. The new design provides a

workable system that is ready for the future study of colloidal and other samples directly in water.

Future modifications could be performed to improve even further certain aspects, such as for example using automatic fringe detection in the motorised reference arm. Another improvement would be the use of a micrometer-scale controller on the mechanical holder on the tube of reference objective for focusing.

## 3.7 Résumé du chapitre 3

Un deuxième système commercial Linnik modifié au sein de l'équipe IPP est le système OEM Fogale-Nanotech avec un interféromètre Linnik développé dans le cadre d'une collaboration pour l'étude des polluants dans le sol. Le but de ce travail de modification est de combiner la CSI avec l'ATR-FTIR pour l'analyse combinée de couches de colloïdes épaisses inhomogènes. Il est prévu de transférer et de tester le système sur la caractérisation des colloïdes (sec, humide, cellulaire avec des contaminants contenant de l'eau) à IPHC.

Un système de base incomplet, sans le mécanisme du miroir de référence a été acquis, dans le but de le modifier à ICube. Les modifications apportées au microscope Fogale ont été réalisées en plusieurs étapes en commençant par l'ajout d'un mécanisme de miroir de référence dans le cadre du projet PICS (BAS, Bulgarie) puis en changeant le Linnik Fogale d'origine pour une utilisation en immersion dans l'eau.

Pour convertir la tête de l'objectif d'interférence en une installation d'immersion Linnik, plusieurs étapes ont dû être franchies, telles que l'ajout d'objectifs à immersion et le développement d'une solution de compensation de longueur de trajet du bras de référence horizontal. En outre, certaines modifications importantes ont dû être apportées au système pour le rendre utilisable en pratique. Certaines pièces mécaniques ont dû être conçues, fabriquées et installées dans le nouveau système. Une table motorisée a été ajoutée au bras de référence pour simplifier la compensation de la longueur du trajet en facilitant la recherche des franges d'interférence.

Ce chapitre présente et montre le microscope Fogale avec ses spécifications, il présente l'ensemble des modifications apportées ainsi que la démarche utilisée. Les performances du système et les résultats de mesures sont présentées.

Les différentes étapes de modification sont présentés en commençant par l'utilisation d'un objectif Mirau, puis la modification de la configuration de Mirau en Linnik dans l'air, suivi enfin par la modification du Linnik pour des mesures en milieu liquide. Une part importante de ce travail était de trouver des solutions innovantes et viables pour la compensation du chemin optique entre le miroir et l'objectif de référence. L'utilisation d'une compensation « solide » de polymère dans le bras miroir horizontal entre l'objectif et le miroir de référence est étudié et présenté. Dans notre système, le bras de

miroir de référence est monté horizontalement, rendant l'immersion dans un liquide difficile. Dans ce travail, nous avons étudié des solutions alternatives à base de polymères élastiques non liquides placés entre le bout de l'objectif et le miroir de référence en utilisant des billes de polyacrylate de sodium (SPA) ou des éléments de PDMS (polydiméthylsiloxane) ayant des indices très proches de l'eau. Enfin, l'installation d'un moteur pas à pas a permis de modifier le chemin optique du bras de référence pour faciliter la recherche des franges d'interférences.

Les performances après chaque modification sont testées en mesurant différents types d'échantillons de référence et en les confrontant aux résultats de mesures d'autres microscopes. Pour déterminer la résolution du système final, un étalon standard du type RS-N de SiMETRICS a été employé. L'analyse de certains problèmes sont également présentés tels qu'un problème d'alignement vertical du microscope et la perte de résolution latérale.

Ce chapitre montre l'effort apporté dans la modification du microscope Fogale fonctionnant en configuration Linnik à immersion. Les défis et les difficultés du Linnik ont été surmontés en levant un certain nombre de verrous techniques tels que la compensation du chemin optique par des éléments de polymère, l'optimisation de la recherche des franges, ….

Les résultats des tests et l'étude des performances du système modifié sont présentés et démontrés. Le nouveau microscope modifié fournit un système fonctionnel qui est prêt pour l'étude future des échantillons de colloïdes aussi bien que d'autres échantillons nécessitant des mesures en immersion dans l'eau.

# CHAPTER 4

# SURPASSING THE DIFFRACTION LIMIT USING MICROSPHERE ASSISTED 3D IMMERSION MICROSCOPY

## 4.1 Introduction

Conventional optical microscopy has a theoretical resolution restricted by the diffraction limit to approximately 200 nm in the visible spectrum because of the loss of evanescent waves in the far field [109][110]. The conventional optical microscope has a limited magnification due to the effects of diffraction.

The concept of diffraction-limited resolution plays an extremely important role in microscopy. The diffraction effects degrade the image formed in the far-field. For two-point objects of equal intensity to be considered resolved, the minimum separation distance is, $r = k\lambda/n\sin\theta$, where $k = 0.473$, 0.5, and 0.61, as defined by Sparrow, Abbe, and Rayleigh, respectively, $\lambda$ is the illumination wavelength, n is the refractive index of the object-space, and $\theta$ is the half-angle of the objective's acceptance cone [111].

The development of new techniques for imaging with a sub-diffraction-limit is of growing importance in the fields of biomedical imaging and nanoscience. The advantage of the optical diffraction limit is that it can be used in metamaterial-based perfect lenses. These operate in the near-field wave situation and the far-field wave of the plane [112][113].

The techniques of detection of the optical near-fields or using strong non-linear effects are some of the new physical principle to increase the resolution beyond the diffraction limit [114][115]. The demonstration of sub-diffraction-limited imaging with a magnifying optical hyperlens based on curved metamaterial can be used for conventional optical microscope observation. In 2007 Y.Xiong [109] reported that 2D sub-diffraction-limited images can be reconstructed theoretically by a material far-field super lens (FSL) made of a silver slab and a 1D subwavelength grating. The silver slab enhances the evanescent waves while the subwavelength grating converts the enhanced evanescent waves into the propagating waves so that the high spatial frequency information can be collected in the far field, and the sub-diffraction-limited images can be consequently reconstructed.

Recently, microsphere-assisted microscopy has been introduced and has stimulated much research due to its capability to surpass the diffraction limit [116][110]. Using this imaging technique with a sub-diffraction-limited spatial resolution, itis able to resolve the features of an object smaller than $\lambda/2$ [117].

Liu et al. resolves the object beyond the diffraction limit in the near field by using nanoscale spherical lenses [118]. Furthermore, the optical mask is used for achieving the super field of super-resolution based on super-oscillatory lens discovery [119]. Wang et al. carried out magnified virtual and super-resolution imaging using fused silica micro-spheres to obtain a gold-coated anodic aluminum oxide membrane. He used a conventional optical microscope with a claimed resolution of 50 nm [120].

More recently, microspheres have been successfully applied in interference microscopy for the 3D measurement of nanostructures, combining the high axial resolution of interferometry with the improved lateral resolution of microsphere imaging. Wang et al. [121] were the very first to do this with an immersion Linnik configuration, closely followed by Kassamakov et al. with a Mirau configuration in air [122] and our team, IPP, with a Linnik in air [123] [124] using glass microspheres. IPP has also studied the imaging performance of these superresolution techniques using microsphere-assisted 2D imaging with low-coherence phase-shifting interference microscopy technique by numerical simulation [124].

The system used in IPP team is based on a modified Leitz-Linnik interferometric microscope with identical x50 magnification objectives (NA = 0.85) and a PIFOC controlled piezoelectric stage with a capacitive position sensor for Z-scanning of the fringes on the depth of the sample. Between the objective and the piezoelectric table, a glass microsphere is placed on the sample to be observed, as shown in . Images are acquired with a monochrome CMOS camera (Photonfocus MV1-D2048-96-G2) with a Giga Ethernet connection. The measurement system is controlled by a PC with an Intel® Xeon® CPU processor (2.40 GHz, 8 GB RAM) with the Windows 7 operating system (64-bit). The control and analysis software was developed internally in LabVIEW (2014 version, 64-bit, National Instruments) combined with the IMAQ Vision module (Figure 101).

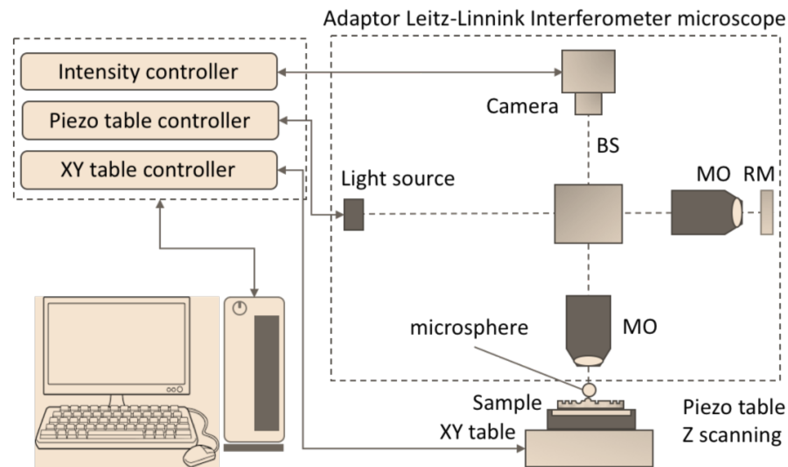


Figure 101. Schema of the nano-3D interferometric microscope of Leitz Linnik in air [125].

The present work is therefore completed with some recent experiments using the modified Fogale immersion Linnik system with microspheres for improved lateral resolution.

## 4.2 Microsphere: definition, utility

Microspheres are small spherical beads particles with diameters in the micrometer range (typically 1 µm to 1000 µm). Microspheres, sometimes referred to as micro-beadsparticle, can be manufactured from various natural and synthetic materials such as glass microspheres, polymers microspheres and ceramics microspheres. Microspheres that we use in this work are made of barium titanate.

$BaTiO_3$ microspheres, also known as Barium Titanate Glass microspheres (BTGMS) are optical glass or dielectric ceramic materials based on a large percentage of Barium Oxide (BaO) and Titanium Oxide ($TiO_2$) that have higher refractive index (1.9). They reflect back more light directly to the camera because their high index enables the retroreflective effect for high visibility in dark conditions. These high density solid glass spheres can be used for many scientific applications at a density of 4.5g/cc where high density and optical clarity is needed.

In immersion Linnik Fogale system that operates in water, it is necessary to use microspheres with a refractive index higher than that of water. BTGMS is one of the microspheres that fulfil the specification.

## 4.3 Measurements using microspheres

Some microspheres with diameter ranging from 30-90 µm are placed manually on the sample (Figure 102) using a fine mechanical tip then one microsphere place will be chosen to be used to measure the surface sample covered by the microsphere.

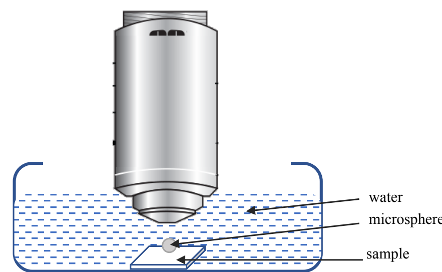


Figure 102. A microsphere-assisted interference microscopy.

The microsphere assisting combined with CSI and or PSM technique based on an immersion Linnik configuration is used for the experimental measurements. The incident beam from the white LED (for CSI technique) or from red LED (for PSM technique) is divided into two by the beam splitter to reference arm and to object arm. In reference arm, the transmitted beam passes through a ×40 or ×20 microscope objective and is then reflected by the reference mirror. While in object arm, the transmitted beam passes through a similar microscope objective and a microsphere, then the microscope objective will collect the virtual image of the sample generated by the

microsphere and beam splitter combines both the beams from object and reference arms.

Different samples are measured with the microsphere-assisted in Fogale immersion Linnik system and compared with measurements from the Zygo, AFM, and Leitz-Linnik microscopes. Some measurements using both techniques of FSA and PSM combined with microsphere-assisted are now carried out as following.

### A. CSI technique with microsphere-assisted

The experimental conditions of the immersion system used for this measurement are the same as for the previous measurements in Ch 3: the Photonfocus CMOS camera, the white light LED and immersion objectives (×20 and ×40 magnifications). The pattern of etched squares on Silicon sample is re-used to be measured in order to compare the results with and without using the microspheres. In the experiment, the sample is scanned over the depth of the pattern from 2.5 – 2.8 µm and using the FSA technique to process the captured scanned images.

- Patterned etched silicon wafer hole area-2

Interferometry scanning is carried out to measure etched Silicon on hole area-2 of the surface of etched Silicon through a 67 µm BTGMS in water. Figure 103 shows the distribution of the microspheres used on the sample surface. In this measurement, one microsphere is chosen (arrow marked), in view of its position over the small squares.

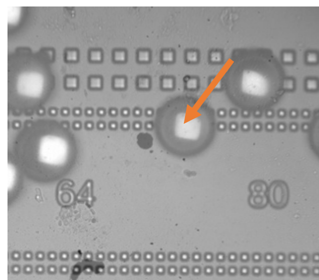


Figure 103. Position of BTGMS on the sample using ×20 immersion Linnik Fogale microscope. The diameter of the microsphere is 67 µm, [4673b].

Figure 104 shows the results of measurement using a 67 µm and a 64 µm BTGMS using ×20 immersion Linnik Fogale microscope while Table 18 shows all the measurement results compared to results in sub-section 3.4. The additional magnifications using a 67 µm and a 64 µm BTGMS are ×2.60 and ×2.45, respectively.

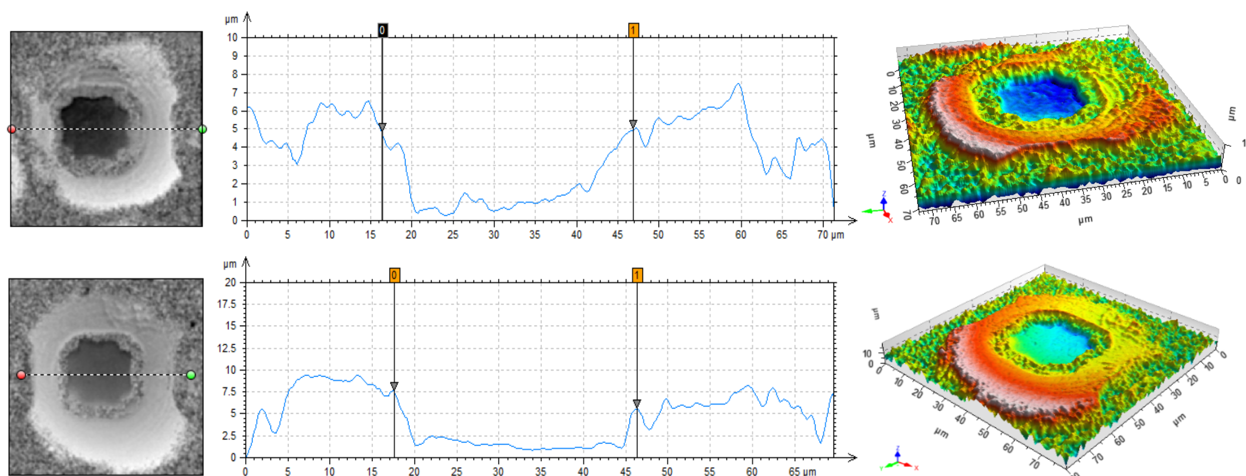

Figure 104. Etched Silicon hole area-2 measured by ×20 immersion Linnik Fogale microscope, (first row) using a 67 µm BTGMS microsphere on it (0.05 step height, 10 dynamic range, $\lambda_{eff}$ = 450 nm, [4673b]); (second row) using a 64 µm-$BaTiO_3$ microsphere on it (0.05 step height, 12 dynamic range, $\lambda_{eff}$ = 450 nm, [4667-c2]).

Table 18. Comparison of measurement results of etched-silicon, hole area-2 using Zygo, Fogale, AFM and microspheres.

| Types of microscope | Width (um) | Depth (um) | Magnification of lateral size using microsphere |
|---|---|---|---|
| ×50 Mirau Zygo | 12.6 | 2.74 | - |
| AFM | 11.518 | 2.054 | - |
| ×20 immersion Linnik Fogale | 11.7 | 2.86 | |
| 67 µm $BaTiO_3$ microsphere (×20 immersion Linnik Fogale) | 28.7<br>30.5 | 2.82 | ×2.60 |
| 64 µm $BaTiO_3$ microsphere (×20 immersion Linnik Fogale) | 28.7 | 2.54 | ×2.45 |

- Patterned etched silicon wafer hole area-3

Interferometric scanning was carried out to measure the etched Silicon on hole area-3 of the surface of the etched Silicon through the 67 µm and 61.7 µm BTGMS in water. Figure 105 shows one microsphere chosen (arrow marked) to see the sample surface.

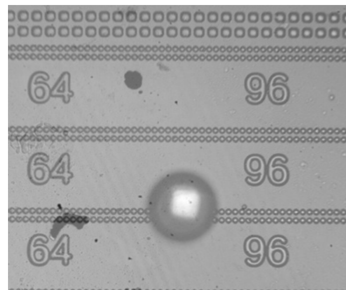


Figure 105. Position of 67 um $BaTiO_3$ on the hole area-3 of etched Silicon, using ×20 immersion Linnik Fogale microscope.

The results of measurements using a 67 µm and a 61.7 µm BTGMS with the ×20 immersion Linnik Fogale microscope are shown in Figure 106 while Table 19 shows all measurement results compared to the results in sub-section 3.4. The additional magnifications using a 67 µm and a 61.7 µm BTGMS are ×2.27 and ×1.97, respectively.

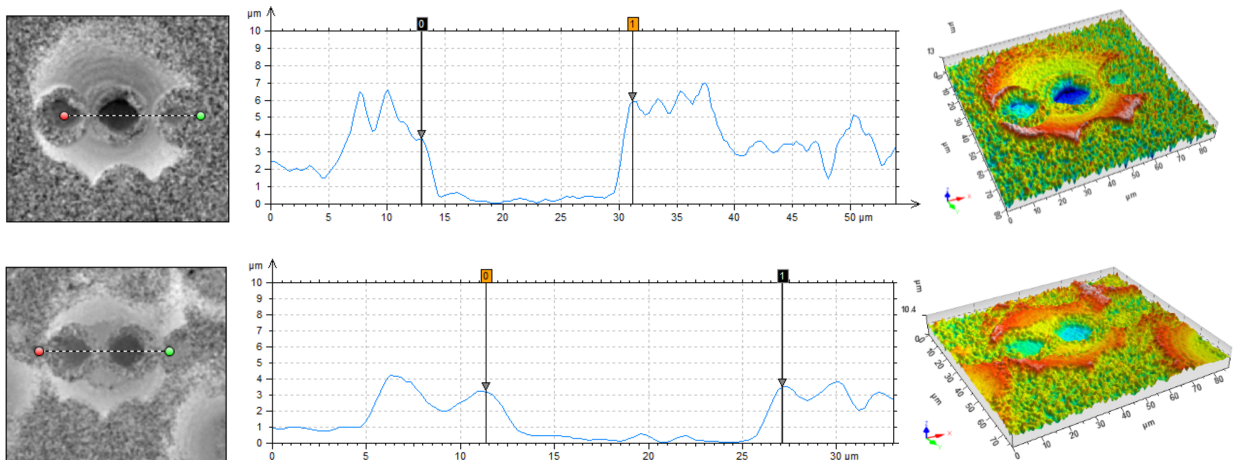


Figure 106. Etched Silicon hole area-3 measured by ×20 immersion Linnik Fogale microscope, (first row) using a 67 µm BTGMS microsphere on it (0.05 step height, 14 dynamic range, $\lambda_{eff}$ = 450 nm, [4678]); (second row) using a 61.7 µm-$BaTiO_3$ microsphere on it (0.05 step height, 10.5 dynamic range, $\lambda_{eff}$ = 450 nm, [4681]).

Table 19. Comparison measurement result of etched-silicon the hole area-3 using Zygo, Fogale, AFM and microspheres.

| Types of microscope | Width (um) | Depth (um) | Magnification of lateral size using microsphere |
|---|---|---|---|
| ×50 Mirau Zygo | 8.11 | 2.22 | - |
| AFM | 8.609 | 2.268 | - |
| ×20 immersion Linnik Fogale | 8.01 | 2.53 | |

| 67 µm $BaTiO_3$ microsphere (×20 immersion Linnik Fogale) | 18.20 | | ×2.27 |
|---|---|---|---|
| 61.7 µm $BaTiO_3$ microsphere (×20 immersion Linnik Fogale) | 15.8 | 2.2 | ×1.97 |

- Patterned etched silicon wafer (ovale patterns)

Interferometric scanning was carried out to measure the etched Silicon on the oval pattern of the sample surface through 70 µm BTGMS in water. Figure 107 shows one microsphere chosen (square marked) to see the sample surface.

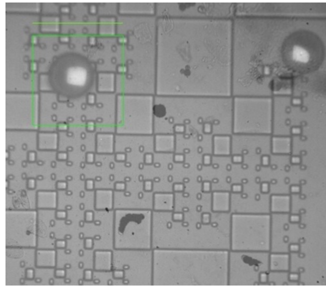

Figure 107. Position of a 70 µm BTGMS on sample in water using Fogale microscope.

Figure 108 shows the results of measurement using a 70 µm BTGMS with the ×20 immersion Linnik Fogale microscope while Table 20 shows all measurement results compared to results in sub-section 3.4. The additional magnifications using a 70 µm is ×2.98.

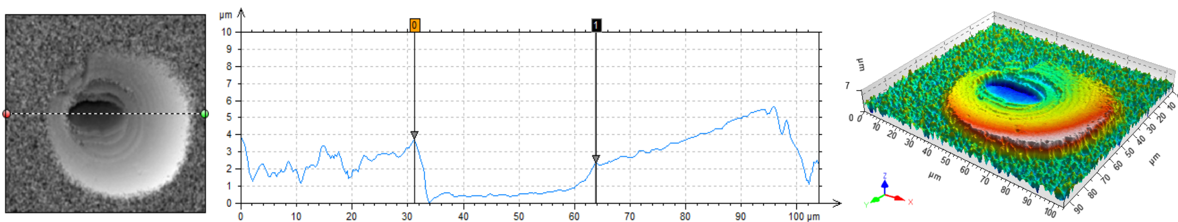


Figure 108. Etched Silicon on oval pattern measured by ×20 immersion Linnik Fogale microscope using a 7 µm BTGMS microsphere on it (0.05 step height, 15.5 dynamic range, $\lambda_{eff}$ = 450 nm, [4675b]).

Table 20. Comparison of measurement results of etched silicon sample using the Zygo, Fogale, AFM and microsphere.

| Types of microscope | Width (um) | Depth (um) | Magnification of lateral size using microsphere |
|---|---|---|---|
| ×50 Mirau Zygo | 12.3 | 2.09 | - |
| AFM | 12.335 | 2.118 | - |
| ×20 immersion Linnik Fogale | 11.0 | 2.1 | |
| 70 µm BaTiO3 microsphere (×20 immersion Linnik Fogale) | 32.8 | 2.1 | ×2.98 |

- Patterned etched silicon wafer (grating pattern)

Interferometric scanning was carried out to measure the etched Silicon oval pattern of the sample surface through 71 µm BTGMS in water. Figure 109 shows one microsphere chosen (arrow marked) to see the sample surface.

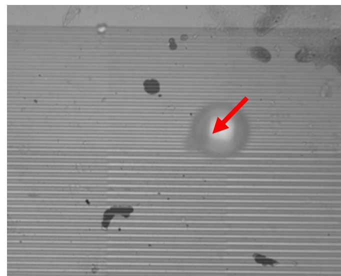

Figure 109. Position of a 71 µm BTGMS on the sample in water using the Fogale microscope.

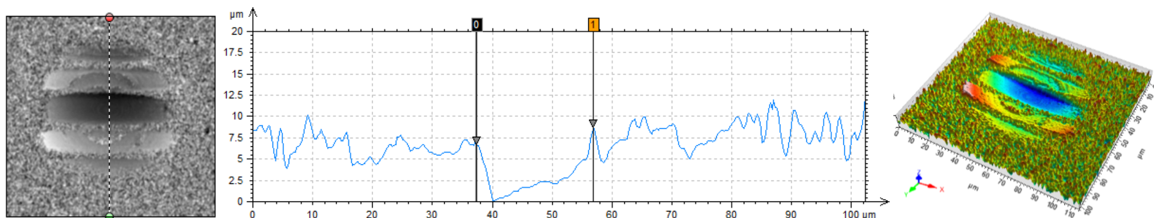


Figure 110. Etched Silicon on grating pattern measured by ×20 immersion Linnik Fogale microscope using a 71 µm BTGMS microsphere on it (0.05 step height, 18 dynamic range, $\lambda_{eff}$ = 450 nm, [4674b]).

The results of measurement using a 71 µm BTGMS using ×20 immersion Linnik Fogale microscope are shown in Figure 110 while Table 21 shows all measurement results

compared to the results in sub-section 3.4. The additional magnification using a 71 µm is ×3.01.

Table 21. Comparison of measurement result of grating sample using Zygo, Fogale, AFM and microsphere.

| Types of microscope | Width (um) | Depth (um) | Magnification of lateral size using microsphere |
|---|---|---|---|
| ×50 Mirau Zygo | 6.41 | 2.06 | - |
| AFM | 8.152 | 5.433 | - |
| ×20 immersion Linnik Fogale | 6.46 | 2.1 | |
| 71 µm BaTiO3 microsphere (×20 immersion Linnik Fogale) | 19.5 | 2.2 | ×3.01 |

**B. PSM technique with microsphere-assisted**

The experimental conditions of the immersion system used for this measurement: the Photonfocus CMOS camera, thered LED and the ×40 immersion objectives and the measured sample of the standard grating from SiMETRICS. A 5x90° steps is used in this PSM technique.

The results of measurement using a 71 µm BTGMS using ×20 immersion Linnik Fogale microscope are shown in Figure 110 while Table 21 shows all measurement results compared to the results in sub-section 3.4. The additional magnification using a 71 µm is ×3.01.

Then the results of the grating measurements using the PSM technique with averaging (no phase unwrapping) through 30-45 µm diameter BTGMS microspheres in water are shown in Figure 111 while Figure 112 shows the results of the grating measurements using the PSM technique with averaging (no phase unwrapping) through 75-90 µm diameter BTGMS microspheres. The measurement results are presented in Table 22 and

Table 23, respectively. These results show magnifications between 2.52 and 2.76 times introduced by the microspheres and the possibility of resolving the 0.3 µm pitch grating.

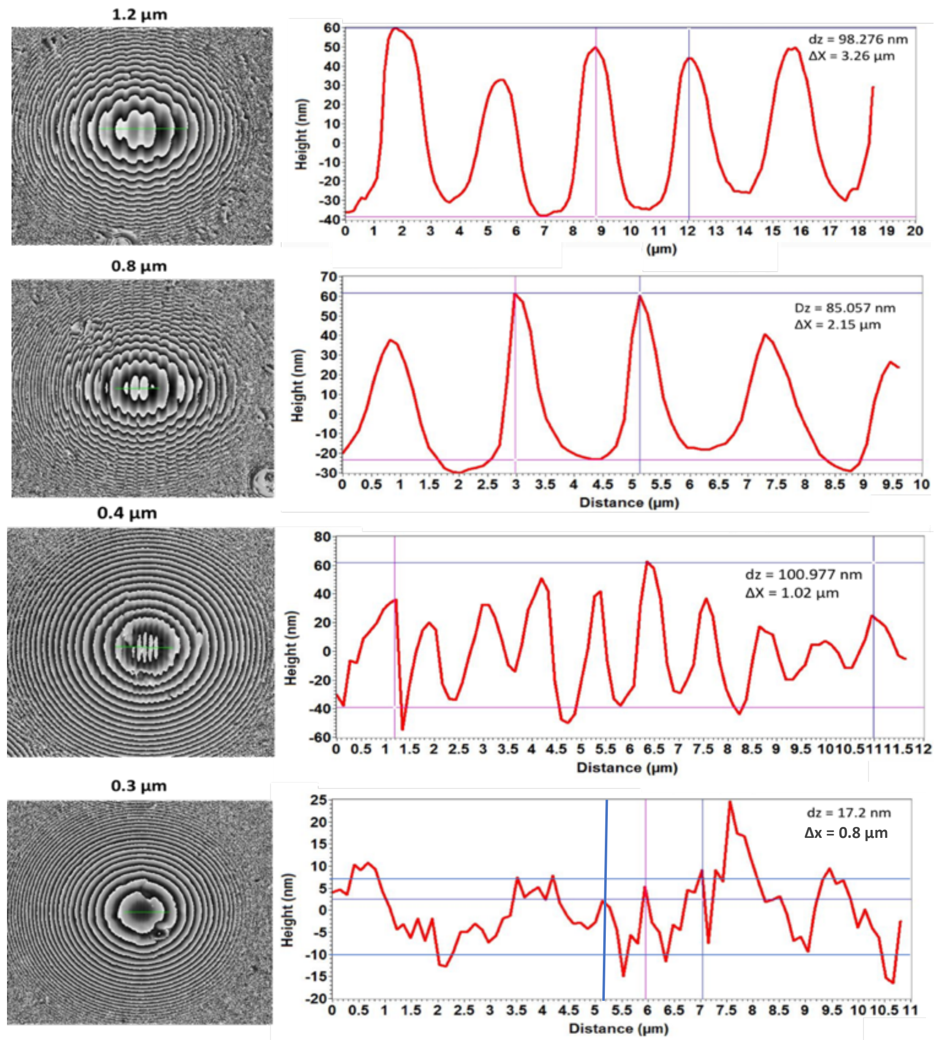


Figure 111. Standard grating SiMETRICS measured by ×40 immersion Linnik Fogale microscope, red LED, 0.056 µm step height, $\lambda_{eff} = 530$ nm in water: pitch 1.2 µm (11 dynamic range, using 43 µm BTGMS); pitch 0.8 µm (5 dynamic range, using 44 µm BTGMS); pitch 0.4 µm (6.5 dynamic range, using 45 µm BTGMS); pitch 0.3 µm (6.5 dynamic range, using 43 µm BTGMS), [4714].

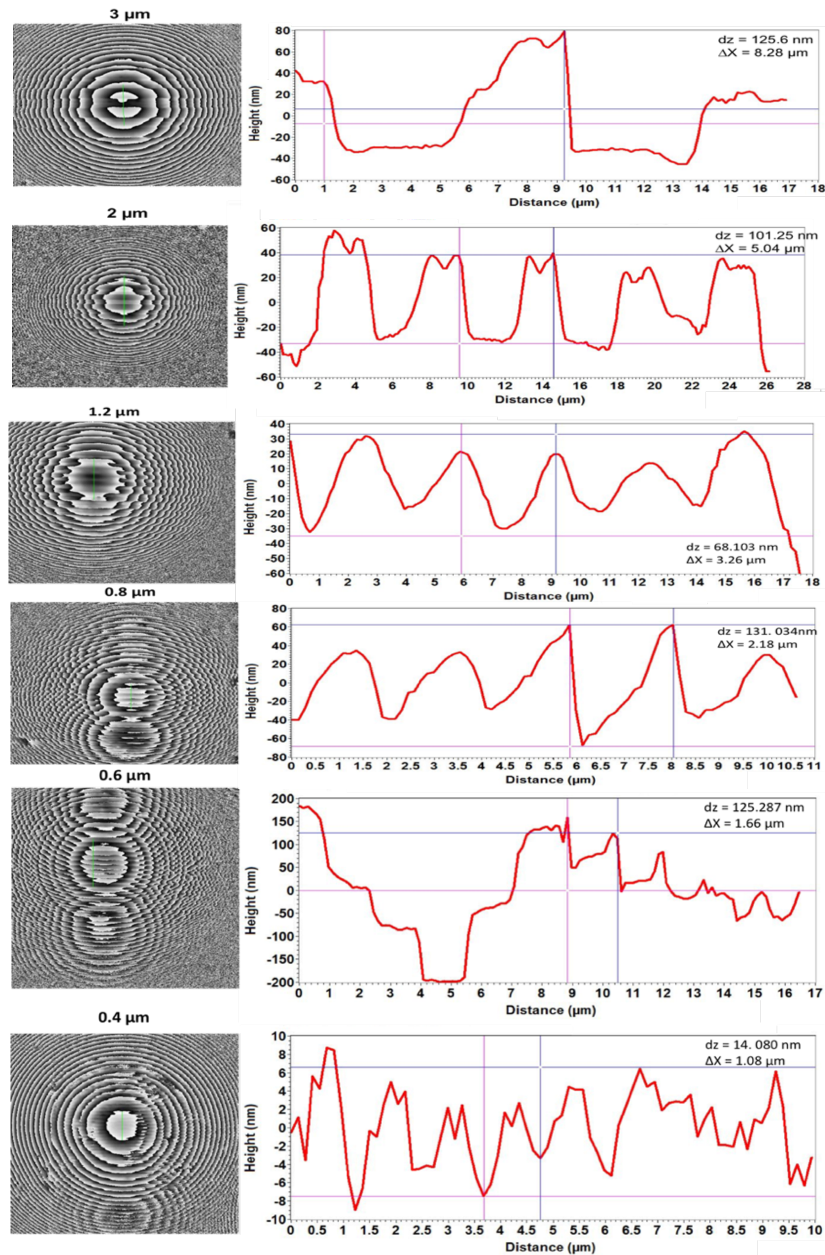


Figure 112. Standard grating SiMETRICS measured by ×40 immersion Linnik Fogale microscope, red LED, 0.090 step height, $\lambda_{eff} = 505$ nm in water: pitch 3 µm (11 dynamic range, using 80 µm BTGMS); pitch 2 µm (10 dynamic range, using 80 µm BTGMS); pitch 1.2 µm (10 dynamic range, using 82 µm BTGMS); pitch 0.8 µm (10 dynamic range, using 77 µm BTGMS); pitch 0.6 µm (10 dynamic range, using 77 µm BTGMS); pitch 0.4 µm (10 dynamic range, using 75 µm BTGMS), [4716].

Table 22. Measurement results of standard grating SiMETRICS using BTGMS in range 30-45 µm.

| Pitch grating | measured pitch grating (µm) | measured depth (nm) | ∅ BaTiO3 (µm) | M lateral |
|---|---|---|---|---|
| 1.2 | 3.26 | 98.276 | 43 | ×2.72 |
| 0.8 | 2.15 | 85.057 | 44 | ×2.67 |
| 0.4 | 1.02 | 100.977 | 45 | ×2.55 |
| 0.3 | 0.80 | 17.2 | 43 | ×2.67 |

Table 23. Measurement results of standard grating SiMETRICS using BTGMS microsphere in range 75-90 µm.

| Pitch grating | measured pitch grating (µm) | measured depth (nm) | ∅ BaTiO3 (µm) | M lateral |
|---|---|---|---|---|
| 3 | 8.28 | 125.62 | 80 | ×2.76 |
| 2 | 5.04 | 101.25 | 80 | ×2.52 |
| 1.2 | 3.26 | 68.103 | 82 | ×2.72 |
| 0.8 | 2.18 | 131.034 | 77 | ×2.752 |
| 0.6 | 1.6 | 125.287 | 77 | ×2.67 |
| 0.4 | 1.08 | 14.08 | 75 | ×2.7 |

# 4.5 Discussion

We present in this chapter some of the very first results of combining immersion CSI and or PSM assisted with $BaTiO_3$ microspheres using the new Fogale modified system. Without microspheres, the system is only capable of measuring the RS-N standard grating to the limit 0.8 µm (in subsection 3.5.2), but with a 43 µm diameter

microsphere, the system is able to measure a pitch of 0.3 μm (Table 21). The lateral measurement is not significantly affected by the diameter of microsphere. Moreover, the measurements of the height or depth of grating are not accurate. The error in this height measurement is possibly due to the difference between the OPD and the value of the real height and/or the resolution limit of the microscope objective [124]. In addition, measurement in water could lead to additional errors.

For the results of microsphere-assisted microscopy with the immersion CSI method, these dielectric microsphere lenses can measure deep etched Si structures by up to 3.01 times of additional magnification (Table 20).

# 4.6 Conclusion

A high-resolution measurement has been performed on some patterns of etched Silicon and standard grating SiMETRICS. The combinations of microsphere-assisted imaging technique with low-coherence scanning interferometry with CSI technique and with low-coherence phase-shifting microscopy have been presented. An experimental system based on an immersion Linnik configuration has demonstrated an improvement by a factor of 4.5 in the lateral resolution in water using white light LED at the effective wavelength 450 nm. Lateral resolution of 1.2 μm and 0.8 at a wavelength of 530 nm has been achieved with microscope objective of ×20 (NA=0.5) and ×40 (NA=0.8) respectively.

# 4.6 Résumé du chapitre 4

La microscopie optique conventionnelle a une résolution théorique limitée par la diffraction à environ 200 nm dans le spectre visible en raison de la perte d'ondes évanescentes dans le champ lointain. Le grossissement du microscope optique conventionnel est ainsi limité à cause de la diffraction.

Les nouvelles techniques d'imagerie en dessous de la limite de diffraction sont très importantes aujourd'hui, surtout dans les domaines du biomédical et des nanosciences.

Récemment, la microscopie optique assistée par microsphère a été développée en raison de sa capacité à dépasser la limite de diffraction. L'utilisation de cette technique d'imagerie avec une résolution spatiale en dessous de la limite de la diffraction est capable de résoudre les caractéristiques d'un objet de taille inférieure à λ / 2. Liu et al. résout l'objet au-delà de la limite de diffraction dans le champ proche en utilisant des lentilles sphériques à l'échelle nanométrique. Wang et al ont réalisé l'imagerie agrandie virtuelle et super-résolution en utilisant une microsphère de silice fondue pour obtenir une membrane d'oxyde d'aluminium anodique revêtue d'or. Il a utilisé un microscope optique classique avec une résolution citée de 50 nm.

Plus récemment, les microsphères ont été utilisée avec succés dans la microscopie interférentielle pour la mesure 3D des nanostructures, en combinant la résolution axiale élevée de l'interférométrie avec la résolution améliorée de l'imagerie par microsphères. Wang et al. étaient les premiers de réussir ces mesures, avec un Linnik à immersion [Wang et al. 2016], suivi par Kassamakov et al. avec une configuration Mirau dans l'air Les travaux exploratoire utilisant ces technique ont été mis en œuvre dans notre équipe IPP avec un Linnik dans l'air.

Dans cette dernière partie les résultats expérimentaux sont présentés en combinant des microsphères de BaTiO3 d'un diamètre allant de 30-75 um avec la CSI. Elles permettent d'augmenter le grossissement d'un facteur 3,5 avec une augmentation de la résolution latérale de 2.5 à 3 fois. Ces résultats sont très encourageant mais nécessitent cependant une étude théorique et d'analyse afin de comprendre finement l'ensemble des phénomènes subjacents.

# CONCLUSION AND PERSPECTIVES

## Conclusion

Improvements have been made to a commercial Linnik microscope in order to perform measurements in water for studying structures of transparent and non-transparent samples. One of the main goals of the present work is to study pollutants in colloidal layers immersed in liquid. The second reason to work in liquid is to increase the lateral resolution. The challenges to overcome include achieving stability in the complex Linnik design as well as the difficulty of balancing the optical distance of the two arms of the interferometer to obtain the interference fringes. The main problem is the path length compensation in the mirror arm which needs a complex mechanical design to allow a high enough number of degrees of freedom to correct alignment of the optical elements.

The first part of the work carried out over the study period has involved a bibliographic study of interference microscopy and in particular different designs of the Linnik interferometer for use in air and in water. Some bibliographic research has been carried out to find solutions to overcome the challenges and difficulties of the design and modification necessary. Then attention has been paid to adapting the Fogale Linnik microscope. This microscope has undergone several modifications, starting by changing the microscope column for one that is more stable, testing this using a Mirau objective, changing the white light LED and finally carrying out several modifications to the Linnik setup for water-immersion by making some mechanical adaptions and obtaining the correct compensation in the horizontal arm between the reference objective and mirror. Finally, a motorized translation stage has been installed in the reference arm in order to simplify the finding of the white light fringes.

The performance of the system after each modification has been tested by measuring different types of samples and the results were compared with those from other microscopes. By using standard calibration of RS-N SiMETRICS, the experimental resolutions measured are 1.2 µm for the ×20 immersion objective and 0.8 µm for the ×40 immersion objective.

In this work, we have presented a new measurement system of a water immersion Linnik using elastic polymer path length compensation for 3D profiling of materials and colloidal samples in water. The use of self-supporting SPA and PDMS slabs between the reference mirror and the objective for compensating the optical path difference provide a convenient alternative solution to that of water without the problems of leakage. The first results of the system in measuring etched silicon holes and colloid layers show better image quality for the measurements in water. In addition, a new super-resolution technique has been tested, namely using barium titanate microspheres to increase the lateral resolution. This opens the possibility of characterizing chemical

and biological phenomena in liquid at high resolution using an optical non-contacting and non-invasive technique.

**Perspectives**

- The immersion Linnik Fogale system opens the possibility of characterizing chemical and biological phenomena in liquid at high resolution using an optical non-contacting and non-invasive technique.
- The future modifications could be performed to improve even further certain aspects: using automatic fringe detection in the motorised reference arm, using a precision motorised control of the mechanical holder on the reference objective tube for focusing, etc.
- In future, carry out an experimental simulation of the optical polymer to improve the resolution by observing the aberration and other factors of resolution loss.
- The experiment of microsphere assisted in interferometry introduce the utilization of combination of local spectroscopy with CSI in liquid to measure the transparent materials, sample based solution, etc.

# BIBLIOGRAPHY


[1] J. Schmit, J. Reed, E. Novak, and J. K. Gimzewski, “Performance advances in interferometric optical profilers for imaging and testing,” *J. Opt. A Pure Appl. Opt.*, vol. 10, no. 6, pp. 1–7, 2008.

[2] A. Bosseboeuf and S. Petitgrand, “Application of microscopic interferometry techniques in the MEMS field,” in *Microsystems Engineering: Metrology and Inspection III*, 2003, vol. 5145, no. 1, pp. 1–16.

[3] P. Montgomery, F. Anstotz, and J. Montagna, “High-speed, on-line 4D microscopy using continuously scanning white light interferometry with a high-speed camera and real-time FPGA image processing,” in *Optical Measurement Systems for Industrial Inspection VII*, 2011, vol. 8082, pp. 808210–808219.

[4] P. C. Montgomery, D. Montaner, and F. Salzenstein, “Tomographic analysis of medium thickness transparent layers using white light scanning interferometry and XZ fringe image processing,” in *Proc. SPIE, 8430*, 2012, vol. 2, no. 1, pp. 1–9.

[5] R. Claveau, P. C. Montgomery, M. Flury, and D. Montaner, “Local reflectance spectra measurements of surfaces using coherence scanning interferometry,” vol. 9890, p. 98900Q, 2016.

[6] P. Montgomery, F. Anstotz, J. Montagna, D. Montaner, L. Pramatarova, and E. Pecheva, “Towards real time 3D quantitative characterisation of in situ layer growth using white light interference microscopy,” *J. Phys.*, vol. 253, 2010.

[7] A. Dubois, K. Grieve, G. Moneron, R. Lecaque, L. Vabre, and C. Boccara, “Ultrahigh-resolution full-field optical coherence tomography,” *Appl. Opt.*, vol. 43, pp. 2874–2883, 2004.

[8] R. Leach, C. Giusca, and F. Blateyron, *Optical measurement of surface topography*. Springer, 2011.

[9] J. Schmit, K. Creath, and J. C. Wyant, “Surface Profilers, Multiple Wavelength, and White Light Intereferometry,” in *Optical Shop Testing: Third Edition*, 2006.

[10] P. E. West, *Introduction to Atomic Force Microscopy Theory Practice Applications*. 2006.

[11] R. Young, J. Ward, and F. Scire, “The topographiner: An instrument for measuring surface microtopography,” *Rev. Sci. Instrum.*, vol. 43, pp. 999–1011, 1972.

[12] J. M. Bennett and J. H. Dancy, “Stylus profiling instrument for measuring statistical properties ofsmooth optical surfaces,” *Appl. Opt.*, vol. 20, no. 10, pp. 1785–1802, 1981.

[13] G. A. Al-Jumaily, S. R. Wilson, K. C. Jungling, J. R. McNeil, and J. M. Bennett, “Frequency Response Characteristics Of A Mechanical Surface Profilometer,” vol. 26, pp. 269953–269956, 1987.

[14] S. Jaturunruangsri and P. Sciences, “Evaluation of Material Surface Profiling Methods : Contact versus Non-contact A thesis submitted in partial fulfilment of the requirements of Brunel University London for the degree of Master of Philosophy by Supaporn Jaturunruangsri College of Engineerin,” Brunel University London, 2014.

[15] P. Lehmann, “Optical versus tactile geometry measurement: alternatives or counterparts,” 2003, vol. 5144, pp. 5114–5144.

[16] H. Ahmadi and M. Mollabashi, “SPIE Optical Metrology,” in *Optical exploration of micro-/nanoscale irregularities created on metallic surfaces by femtosecond laser irradiation*, 2017, vol. 44, no. 0, p. 38.

[17] T. Hattori, “Analysis of microscopic areas on wafer surfaces usingg STM/AFM,” in *Ultraclean surface processing of silicon wafers: secrets of VLSI manufacturing*, Springer, 1998, p. 223.

[18] G. Binnig and H. Rohrer, “Scanning tunneling microscopy,” *Helv. Phys. Acta*, vol. 55, 1982.

[19] M. Liu, “STM study of twisted bilayer graphene,” in *Controlled synthesis and scanning tunneling microscopy study of graphene and graphene-based heterostructures*, Beijing: Springer, 2017, pp. 36–40.

[20] Y. Bar-Cohen, W. K. Jones, and R. Cormia, “Characterization method for low tempearture materials,” in *Low temperature material and mechanisms*, pp. 68–78.

[21] B. Bhushan and O. Marti, “Scanning Probe Microscopy – Principle of Operation , Instrumentation , and Probes,” in *Nanotribology and mechanic*, Springer, 2011, pp. 37–100.

[22] G. Binnig and H. Rohrer, “Scanning Tunneling Microscopy,” *Surf. Sci.*, vol. 126, pp. 236–244, 1983.

[23] P. Markiewicz and M. C. Goh, “Atomic force microscopy probe tip visualization and improvement of images using a simple deconvolution procedure,” *Langmuir*, vol. 10, no. 1, pp. 5–7, Jan. 1994.

[24] S. Y. and H. Y. and Hiroshi Tokumoto, “Nanometer Modifications of Non-Conductive Materials Using Resist-Films by Atomic Force Microscopy,” *Jpn. J. Appl. Phys.*, vol. 34, no. 6S, p. 3396, 1995.

[25] T. R. Albrecht and C. F. Quate, “Atomic resolution imaging of a nonconductor by atomic force microscopy,” *J. Appl. Phys.*, vol. 62, no. 7, pp. 2599–2602, Oct. 1987.

[26] S. Alexander *et al.*, “An atomic-resolution atomic-force microscope implemented using an optical lever,” *J. Appl. Phys.*, vol. 65, no. 1, pp. 164–167, Jan. 1989.

[27] J. P. Cleveland, B. Anczykowski, a. E. Schmid, and V. B. Elings, “Energy dissipation in tapping-mode atomic force microscopy,” *Appl. Phys. Lett.*, vol. 72, no. 20, p. 2613, 1998.

[28] Q. Zhong, D. Inniss, K. Kjoller, and V. B. Elings, “Fractured polymer/silica fiber

surface studied by tapping mode atomic force microscopy," *Surf. Sci. Lett.*, vol. 290, no. 1–2, pp. L688–L692, Jun. 1993.

[29] T. Uchihashi, N. Kodera, and T. Ando, "High-Speed Atomic Force Microscopy," 2015.

[30] F. J. Giessibl, S. Hembacher, H. Bielefeldt, and J. Mannhart, "Subatomic Features on the Observed by Atomic Force Microscopy," *Science (80-. ).*, vol. 289, no. July, pp. 422–425, 2000.

[31] D. Rugar, R. Budakian, H. J. Mamin, and B. Chui, "Single spin detection by magnetic resonance force microscopy," *Lett. Nat.*, vol. 430, pp. 329–332, 2004.

[32] Y. Sugimoto *et al.*, "Chemical identification of individual surface atoms by atomic force microscopy," *Lett. Nat.*, vol. 446, pp. 64–67, 2007.

[33] A. M. Baró, "Force Spectroscopy," in *Atomic Force Microscopy in Liquid*, Wiley-VCH Verlag GmbH & Co. KGaA, 2012, pp. 65–86.

[34] B. Larijani, C. A. Rosser, and R. Woscholski, *Chemical biology: techniques and applications*. Wiley, 2006.

[35] O. Marti, B. Drake, and P. K. Hansma, "Atomic force microscopy of liquid-covered surfaces: atomic resolution images," *Appl. Phys. Lett.*, vol. 51, no. 484, 1987.

[36] M. Guthold, M. Bezanilla, D. A. Erie, B. Jenkins, H. G. Hansma, and C. Bustamante, "Following the assembly of RNA polymerase-DNA complexes in aqueous solutions with the scanning force microscope," *Natl.Acad.Sci.USA*, pp. 12927–12930, 1994.

[37] C. A. J. Putman, K. Van Der Wetf, B. G. De Grooth, N. F. Van Hulst, and J. Greve, "Tapping mode atomic force microscopy in liquid," *Appl. Phys. Lett.*, vol. 64, no. 18, pp. 2453–2456, 1994.

[38] T. Fukuma, "True atomic resolution in liquid by frequency-modulation atomic force microscopy," *Appl. Phys. Lett.*, vol. 87, no. 3, 2005.

[39] T. Ando *et al.*, "High-Speed Atomic Force Microscopy for Studying the Dynamic Behavior of Protein Molecules at Work," *Jpn. J. Appl. Phys.*, vol. 45, no. 3S, p. 1897, 2006.

[40] T. Ando, N. Kodera, D. Maruyama, E. Takai, K. Saito, and A. Toda, "A High-Speed Atomic Force Microscope for Studying Biological Macromolecules in Action," *Jpn. J. Appl. Phys.*, vol. 41, no. 7S, p. 4851, 2002.

[41] N. A. Workshop, "Liquid Scanning with an Atomic Force Microscope," *AFM workshop newsletter*, 2014.

[42] P. J. Besl, "Active optical range imaging sensors," in *Machine vision and applications*, vol. 1, 1989, pp. 127–152.

[43] G. Berkovic and E. Shafir, "Optical methods for distance and displacement measurements," *Adv. Opt. Photonics*, vol. 4, no. 4, p. 441, 2012.

[44] R. G. Dorsch, G. Häusler, and J. M. Herrmann, "Laser triangulation: fundamental

uncertainty in distance measurement," *Appl. Opt.*, vol. 33, no. 7, pp. 1306–1314, 1994.

[45] S. Inoué and R. Oldenbourg, "Ch 17 Microscopes," in *Optical Instruments*, 1986, pp. 1–52.

[46] T. Corle and G. Kino, *Confocal scanning optical microscopy and related imaging systems*. Academic Press, 1999.

[47] P. J. de Groot and J. F. Biegen, "Interference microscope objectives for wide-field areal surface topography measurements," *Opt. Eng.*, vol. 55, no. 7, p. 074110, 2016.

[48] M. E. Motamedi and J. Schwider, "Micro-Optic component, testing, and applications," in *MOEMS: Micro-opto-electro-mechanical systems*, M. E. Motamedi, Ed. Bellingham: SPIE Press, 2005, pp. 230–240.

[49] O. V. Lyulko, G. Randers-Pehrson, and D. J. Brenner, "Immersion Mirau interferometry for label-free live cell imaging in an epi-illumination geometry," in *Proc. SPIE*, 2010, p. 756825.

[50] O. Haeberlé, A. Sentenac, and H. Giovannini, "An introduction to diffractive tomographic microscopy."

[51] P. J. Caber, "Interferometric profiler for rough surfaces," *Appl. Opt.*, vol. 32, no. 19, p. 3438, 1993.

[52] J. Petzing, J. M. Coupland, and R. K. Leach, *The measurement of rough surface topography using coherance scanning interferometry*, no. 116. National Physical Laboratory, 2010.

[53] G. Häusler and S. Ettl, "Limitations of Optical 3D Sensors," in *Optical Measurement of Surface Topography*, Berlin: Springer, 2011.

[54] M. Pluta, *Advanced Light Microscopy*, vol. 2. Warsawa: Elsevier and PWN-Polish Scientific Publishers, 1989.

[55] W. Kaplonek and C. Lukianowicz, "Coherence Correlation Interferometry in Surface Topography Measurements," in *Recent Interferometry Applications in Topography and Astronomy*, I. Padron, Ed. Rijeka: InTech, 2012, pp. 1–27.

[56] K. G. Larkin, "Efficient nonlinear algorithm for envelope detection in white light interferometry," *J. Opt. Soc. Am. A*, vol. 13, no. 4, 1996.

[57] P. C. Montgomery and J. P. Fillard, "Peak fringe scanning microscopy (PFSM): sub-micron 3D measurement of semiconductor components," in *Interferometry: Techniques and Analysis*, vol. 1755, no. 1992, pp. 12–23.

[58] Benatmane Abderrazzaq, "Développement de la microscopie interférométrique pour une meilleure analyse morphologique des couches minces e t épaisses des matériaux semiconducteurs et optiques," 2002.

[59] P. C. Montgomery, F. Salzenstein, D. Montaner, B. Serio, and P. Pfeiffer, "Implementation of a fringe visibility based algorithm in coherence scanning interferometry for surface roughness measurement," *SPIE*, 2013.

[60] P. de Groot, “Derivation of algorithms for phase-shifting interferometry using the concept of a data-sampling window,” *Appl. Opt.*, vol. 34, no. 22, p. 4723, 1995.

[61] H. P. Stahl, “Review of phase measuring interferometry,” in *Optical testing and Metrology III: recent advances in industrial optical inspection*, 1990.

[62] J. P. Fillard, “Near Field optics and nanoscopy,” in *Word Scientific*, 1996, pp. 197–214.

[63] W. Xu, “Modélisation et fabrication de microinterféromètres Mirau accordables intégrés 3D Modeling and fabrication of tunable 3D integrated Mirau micro-interferometers Composition du jury,” Université Paris-Sud, 2014.

[64] J. C. Wyant, “Computerized interferometric measurement of surface microstructure,” in *Proceedings of the International Conference on Optical Fabrication and Testing*, 1995, vol. 2576, pp. 122–130.

[65] M. Servin, J. L. Marroquin, and F. J. Cuevas, “Demodulation of a single interferogram by use of a two-dimensional regularized phase-tracking technique,” *Appl. Opt.*, vol. 36, no. 19, p. 4540, 1997.

[66] P. Montgomery *et al.*, “Characterization of III-V materials by optical interferometry,” *Phys.III*, vol. 3, pp. 1791–1802, 1993.

[67] P. Sandoz, “Wavelet transform as a processing tool in white-light interferometry,” *Opt. Lett.*, vol. 22, no. 14, p. 1065, 1997.

[68] Taylor Hobson, *Exploring Surface Texture: A fundamental guide to the measurement of surface finish*, 7th ed. Taylor Hobson, 2011.

[69] A. Dubois, “Full-field optical coherence microscopy with optimized ultrahigh spatial resolution,” *Opt. Lett.*, vol. 40, no. 22, pp. 5347–5350, 2015.

[70] C. Cremer and B. R. Masters, “Resolution enhancement techniques in microscopy,” *Eur. Phys. J. H*, vol. 38, no. 3, pp. 281–344, 2013.

[71] C. L. Giusca, R. K. Leach, M. Fabich, and T. Gutauskas, “Calibration of the areal metrological characteristics of scanning confocal microscopes,” *Precis. Eng. Manuf.*, vol. X, no. X, pp. 1–6, 2011.

[72] A. J. Den Dekker and A. Van Den Bos, “Resolution : a survey,” *J.Opt Soc*, vol. 14, no. 3, pp. 547–557, 1997.

[73] L. O. O. Kittang, “Development and testing of a Linnik Interference Microscope for Sub-surface Inspection of Silicon during moving Indentation,” 2012.

[74] L. Novotny and B. Hecht, *Priciples of nano-optics*. Cambridge: Cambridge university press, 2006.

[75] Editorial, “Beyond the diffraction limit,” vol. 3, no. July, p. 2009, 2009.

[76] M. A. X. Born and E. Wolf, “Interference and diffraction with partially coherent light,” in *Principles of Optics*, 7th ed., London: Cambridge university press, pp. 554–578.

[77] X. Colonna De Lega and P. de Groot, “Lateral resolution and instrument transfer

function as criteria for selecting surface metrology instruments," in *Imaging and Applied Optics Technical Digest*, 2012, no. June, pp. 1–3.

[78] S. Bradbury, *An introduction to the optical microscope*. Oxford university Press, 1989.

[79] F. Gao, R. K. Leach, and J. . Coupland, "Surface measurement errors using commercial scanning white light interferometers," *Meas. Sci. Technol.*, vol. 19, no. 1, p. 15303, 2008.

[80] S. Boedecker, W. Bauer, R. Krüger-Sehm, P. H. Lehmann, and C. Rembe, "Comparability and uncertainty of shape measurements with white-light interferometers," 2010, vol. 7718, no., p. 77180J–7718–12.

[81] S. Hell and E. H. K. Stelzer, "Properties of a 4Pi confocal fluorescence microscope," *J. Opt. Soc. Am. A*, vol. 9, no. 12, p. 2159, 1992.

[82] S. Lindek, C. Cremer, and E. H. K. Stelzer, "Confocal theta fluorescence microscopy using two-photon absorption and annular aperatures," *Appl. Opt.*, vol. 35, no. 1, pp. 126–130, 1996.

[83] M. Schrader, S. W. Hell, and H. T. M. van der Voort, "Potential of confocal microscopes to resolve in the 50–100 nm range," *Appl. Phys. Lett.*, vol. 69, 1996.

[84] A. Dubois, L. Vabre, A.-C. Boccara, and E. Beaurepaire, "High-resolution full-field optical coherence tomography with a Linnik microsphere," *Appl. Opt.*, vol. 41, pp. 805–811, 2002.

[85] J. Niehues, P. Lehmann, and W. Xie, "Low coherent Linnik interferometer optimized for use in Nano Measuring Machines," in *56th IWK, International Scientific Colloquium*, 2013.

[86] A. Dubois, "Full-Field Optical Coherence Microscopy," in *Selected Topics in Optical Coherence Tomography, INTECH*, 2012, pp. 3–20.

[87] L. Byeong-il *et al.*, "Feasibility of Full-field Optical Coherence Microscopy in Ultra-structural Imaging of Human Colon Tissues," *J. Korean Phys. Soc.*, vol. 57, no. 1, p. 79, 2010.

[88] J. Larry Pezzaniti and R. A. Chipman, "Angular dependence of polarizing beam-splitter cubes.," *Appl. Opt.*, vol. 33, no. 10, pp. 1916–1929, 1994.

[89] W. Y. Oh, B. E. Bouma, N. Iftimia, S. H. Yun, R. Yelin, and G. J. Tearney, "Ultrahigh-resolution full-field optical coherence microscopy using InGaAs camera," *Opt. Express*, vol. 14, no. 2, pp. 13–19, 2006.

[90] Y. Chen, S. W. Huang, C. Zhou, B. Potsaid, and J. G. Fujimoto, "Improved Detection Sensitivity of Line-Scanning Optical Coherence Microscopy," *IEEE J Sel Top Quantum Electron*, vol. 18, no. 3, pp. 1094–1099, 2012.

[91] E. Pecheva, P. Montgomery, D. Montaner, and L. Pramatarova, "White Light Scanning Interferometry Adapted for Large-Area Optical Analysis of Thick and Rough Hydroxyapatite Layers," *Langmuir*, pp. 3912–3918, 2007.

[92] A. Leong-hoï *et al.*, "Detection of defects in a transparent polymer with high

resolution tomography using white light scanning interferometry and noise reduction," in *Videometrics, range imaging, and applications XIII*, 2015, vol. 9528.

[93] E. Halter *et al.*, "Characterization of inhomogeneous colloidal layers using adapted coherence probe microscopy," *Appl. Surf. Sci.*, 2010.

[94] P. C. Montgomery, "PICS 4848: Optical imaging techniques for analysing thick hydroxyapatite/nanodiamond composite layers for the study of biomineralisation," Strasbourg, 2011.

[95] J. J. Thomas and H. M. Jennings, "A colloidal interpretation of chemical aging of the C-S-H gel and its effects on the properties of cement paste," *Cem. Concr. Res.*, vol. 36, no. 1, pp. 30–38, 2006.

[96] E. Neiss *et al.*, "Multi-level diffractive optical elements produced by excimer laser ablation of sol-gel," *Opt. Express*, vol. 16, no. 18, pp. 14044–56, 2008.

[97] V. Kachkanov, K. P. O'Donnell, S. Pereira, and R. W. Martin, "Localization of excitation in InGaN epilayers," *Philos. Mag.*, vol. 87, no. 13, pp. 1999–2017, May 2007.

[98] J. Ogien and A. Dubois, "High-resolution full-field optical coherence microscopy using a broadband light-emitting diode," *Opt. Express*, vol. 24, no. 9, p. 9922, 2016.

[99] B. Povazay *et al.*, "Submicrometer axial resolution optical coherence tomography," *Opt. Lett.*, vol. 27, no. 20, pp. 1800–1802, 2002.

[100] V. Heikkinen, I. Kassamakov, T. Paulin, A. Nolvi, A. Lassila, and E. Haeggström, "Improved interferogram for stroboscopic scanning white light interferometry performed at 2.72 MHz," 2016.

[101] J. Ogien, "Développement de systèmes de microscopir par cohérence optique pour l'imagerie de la peau," Université Paris-Saclay, 2017.

[102] S. Pimputkar, J. S. Speck, S. P. Denbaars, and S. Nakamura, "Prospects for LED lighting," *Nat. photonics www.nature.com/naturephotonics*, vol. 3, 2009.

[103] E. F. Schubert and J. K. Kim, "Solid-state light sources getting smart," *Science (80-. ).*, vol. 308, no. 5726, pp. 1274–1278, 2005.

[104] M. Auf Der Maur, K. Lorenz, and A. Di Carlo, "Band gap engineering approaches to increase InGaN/GaN LED efficiency," *Opt. Quantum Electron.*, vol. 44, no. 3–5, pp. 83–88, 2012.

[105] Y. Jiang *et al.*, "Realization of high-luminous-efficiency InGaN light-emitting diodes in the 'green gap' range," *Sci. Rep.*, vol. 5, no. February, pp. 1–7, 2015.

[106] S. Ross, "Microscopy: Correcting for Spherical Aberration with a Correction Collar," *iBiology.org*, 2013. [Online]. Available: https://www.youtube.com/watch?v=UDJDwKupKHA.

[107] L. Medina-Torres, F. Calderas, G. Sanchez-Olivares, and D. M. Nuñez-Ramirez, "Rheology of sodium polyacrylate as an emulsifier employed in cosmetic

emulsions," *Ind. Eng. Chem. Res.*, vol. 53, no. 47, pp. 18346–18351, 2014.

[108] M. Guellil, P. C. Montgomery, P. Pfeiffer, and B. Serio, "Comparison of areal measurements of the same zone of etched Si and hydroxyapatite layers on etched Si using different profiling techniques," in *Optical micro and nanometrology V*, 2014, vol. 9132, pp. 913204-913204–9.

[109] Y. Xiong, Z. Liu, and X. Zhang, "Far-field superlens imaging at visible wavelengths," *Nano Lett.*, vol. 7, no. 11, pp. 1–2, 2007.

[110] S. Lee, L. Li, Z. Wang, W. Guo, Y. Yan, and T. Wang, "Immersed transparent microsphere magnifying sub-diffraction-limited objects," *Appl. Opt.*, vol. 52, no. 30, p. 7265, 2013.

[111] K. W. Allen *et al.*, "Overcoming the diffraction limit of imaging nanoplasmonic arrays by microspheres and microfibers," *Opt. Express*, vol. 23, no. 19, p. 24484, 2015.

[112] J. B. Pendry, "Negative refraction makes a perfect lens, Phys," *Rev. Lett.*, vol. 85, no. 18, pp. 3966–3969, 2000.

[113] Z. Liu, N. Fang, T. J. Yen, and X. Zhang, "Rapid growth of evanescent wave by a silver superlens," *Appl. Phys. Lett.*, vol. 83, no. 25, pp. 5184–5186, 2003.

[114] S. W. Hell, "Nanoscopy with focused light," *Ann. Phys.*, vol. 527, no. 7–8, pp. 423–445, 2015.

[115] V. N. Astratov *et al.*, "Fundamental limits of super-resolution microscopy by dielectric microspheres and microfibers," in *Nanoscale imaging, Sensing, and Actuation for Biomedical Applications XIII*, 2015.

[116] H. S. S. Lai, F. Wang, Y. Li, B. Jia, L. Liu, and W. J. Li, "Super-resolution real imaging in microsphere-assisted microscopy," *PLoS One*, vol. 11, no. 10, pp. 1–17, 2016.

[117] L. Yao, Y. H. Ye, H. Ma, L. Cao, and J. Hou, "Role of the immersion medium in the microscale spherical lens imaging," *Opt. Commun.*, vol. 335, pp. 23–27, 2015.

[118] Z. Liu, H. Lee, Y. Xiong, and X. Zhang, "Far-Field Optical Hyperlens Magnifying," *Science*, vol. 315, p. 1686, 2012.

[119] E. T. F. Rogers *et al.*, "A super-oscillatory lens optical microscope for subwavelength imaging," *Nat. Mater.*, vol. 11, no. 5, pp. 432–435, 2012.

[120] Z. Wang *et al.*, "Optical virtual imaging at 50 nm lateral resolution with a white-light nanoscope," *Nat. Commun.*, vol. 2, no. 1, pp. 216–218, 2011.

[121] F. Wang *et al.*, "Three-dimensional super-resolution morphology by near-field assisted white-light interferometry," *Sci. Rep.*, vol. 6, no. March, pp. 1–10, 2016.

[122] I. Kassamakov, S. Lecler, A. Nolvi, A. Leong-Hoï, P. Montgomery, and E. Hæggström, "3D Super-Resolution Optical Profiling Using Microsphere Enhanced Mirau Interferometry," *Sci. Rep.*, vol. 7, no. 1, pp. 1–7, 2017.

[123] P. C. Montgomery, S. Lecler, A. Leong-hoï, and P. Pfeiffer, "3D nano surface

profilometry by combining the photonic nanojet with interferometry," *J. Phys.*, vol. 794, 2017.

[124] S. Perrin *et al.*, "Microsphere-assisted phase-shifting profilometry," vol. 56, no. 25, 2017.

[125] Audrey LEONG-HOI, "Étude des techniques de super-résolution latérale en nanoscopie et développement d'un système interférométrique nano-3D," 2016.

# LIST OF PUBLICATIONS AND COMMUNICATIONS

**International refereed journals**

H. Mukhtar, P. Montgomery, G Gianto, K Susanto, "Rock surface roughness measurement using CSI technique and analysis of surface characterization by qualitative and quantitative results," IOP Conf. series: Earth and environmental science 29, 012028, 2016.

**International conferences**

H. Mukhtar, P. Montgomery, F. Anstotz, R. Barillon & A. Rubin, "Immersion white light scanning interferometry using elastic polymer path length compensation", SPIE Photonics Europe, Strasbourg 22-26 April 2018, Proc. SPIE 10678, 2018 (poster).

H. Mukhtar, R. Claveau, P. Montgomery, F. Anstotz, "Performance comparison of air and immersion Linnik objectives in coherence scanning interferometry", Proceedings of 9th International Conference on Nanophotonics (ICNP 2016), Taipei, Taiwan, 21-25th March 2016 (oral).

H. Mukhtar, P. Montgomery, G Gianto, K Susanto, "Rock surface roughness measurement using CSI technique and analysis of surface characterization by qualitative and quantitative results," Padjadjaran Earth Dialogue: International Symposium on Geophysical Issues, Jatinangor, Indonesian, 8-10 June, 2015 (poster).

**Other conferences**

H. Mukhtar, F. Anstotz, R. Barillon, et P.C. Montgomery, "Profilométrie optique haute résolution en immersion par interférométrie", 13$^{e}$ Journées «Imagerie optique non conventionnelle», GDR ISIS et GDR ONDES, mars 2018 (poster).

H. Mukhtar, F. Anstotz, P.C. Montgomery, "Measurement of roughness surface of immersion Linnik CSI for using in research and industry applications in Indonesia," Journée des doctorants d'Indonésie en France, l'Ambassade d'Indonésie, Paris (France), May 2016 (oral).

H. Mukhtar, P. Pfeiffer, P. Twardowski, C. Hairaye, R. Claveau, A. Leong-Hoï, M. Gora, S. Lecler, J. Zelgowsky & P.C. Montgomery, "Photonics innovations for healthcare applications," 7$^{e}$ journée d'ITS/ 2$^{e}$ journée d'innovations, Montpellier, 2015 (poster).

**H. Mukhtar**, P. Montgomery, G Gianto, K Susanto, "Rock surface roughness measurement using CSI technique and analysis of surface characterization by

qualitative and quantitative results," Padjadjaran Earth Dialogue: International Symposium on Geophysical Issues (PEDISGI), Indonesia, June, 2015 (poster).

**H. Mukhtar**, P. Montgomery, F. Anstotz, "Development of immersion CSI for biomaterial and biomedical applications," Poster day doctoral school ED-MSII, Strasbourg, October 2015 (poster).

## SUPPLEMENTARY WORK

Mandatory doctoral student training has been followed:

Scientific training courses followed.

40-50 hours total of Master Modules that are linked to the PhD (***has been completed***)

| No | Course | Lecturer | Total of hours |
|---|---|---|---|
| 1 | Colloids | Pascal Hebraud | 12h00 |
| 2 | Image acquisition | Christophe Collet | 10h30 |
| 3 | Biophotonique | Stefan Haacke | 14h00 |
| 4 | Composants optiques diffractifs | Patrice Twardowski | 08h45 |
| **Total** | | | **45h15** |

6 seminars per year (***has been completed for 2 years***)

| No | Date | Title of seminar |
|---|---|---|
| 1 | 19/11/2014 | LabView: NI Presentation |
| 2 | 21/11/2014 | Nanodiamond- from synthesis to apllications (IPP seminar) |
| 3 | 02/12/2014 | Design and control of robotic device for surgery |
| 4 | 27/01/2014 | Reproducible research in computer science |
| 5 | 17/02/2015 | Les modulateurs spatiaux de lumière dans l'optique du vivant |
| 6 | 02/04/2015 | Conception des systemes micro-electronique |
| 7 | 19/06/2015 | Icube en lumière |
| 8 | 01/10/2015 | Bioengineering: Challenges & opportunities |
| 9 | 12/10/2015 | Presentation du CNRS (Yves Remond) |
| 10 | 16/10/2015 | Modelisation expressive; modéles centres- utilisation pour la creation 3D |
| 11 | 09/12/2015 | La mechanique des fluides à seul (Philippe Coussot) |
| 12 | 25/01/2016 | Scanning WLI (Ivan Kassamakov) (IPP seminar) |
| 13 | 28/04/2016 | Influence de la geometrie à la petite échelle sur le comportement mechanique du béton |
| 14 | 13/06/2016 | Biophotonics ans the future of personal health care |
| 15 | 15/06/2015 | Study of biocompatible and biological materials: can they be stimulated by external factors? |

### Professional training courses

22.5 hours scientific English course during the 2$^{nd}$ year (*has been completed*).

20 – 25 hours training modules (47hrs total has been done in session 2014/2015)

| No | Domain | Sub-Domain | Title | Duration |
|---|---|---|---|---|
| 1 | Knowledge of workplace and personal career plan | Knowledge of the university and its environment | CUE- 2014 Back to School Meeting for the first year Ph.D. | 02h00 |
| 2 | Knowledge of workplace and personal career plan | Europe | Europe- Visit Parliament of Europe (in english) | 01h30 |
| 3 | Tools | Language for foreigner student | Language- english course | 16h00 |
| 4 | Tools | Language for foreigner student | Language- France course for beginner | 18h00 |
| 5 | Tools | Information and communications technology | TIC - tools, collaborative work platforms, example Moodle | 03h30 |
| 6 | Tools | Other tools | AO - Introduction to bibliometrics with Web of Science | 03h00 |
| 7 | Tools | Other tools | AO - Introduction to Zotero | 03h00 |
| | **Total** | | | **47h00** |

# ANNEXES

Annex 1. Data sheet of the light source of initial Fogale, Lumileds LXHL-MW1D white LED, 5500K, round

LXHL-MW1D | Lumileds 5500K White LED, Round Screw Mount package | Lumileds Lighting

## Luxeon® Star (Hexagon)

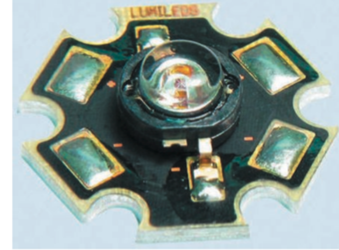


High-output solid-state light source on a hexagon PCB.

Available in 1W, 3W and 5W rating
Available with Batwing, Lambertian & Side-emitting radiation patterns
Lifetime in excess of 10 years (continuous use)

## Note

A suitable heatsink is required for best performance.

## Caution

Not suitable for re-flow soldering.

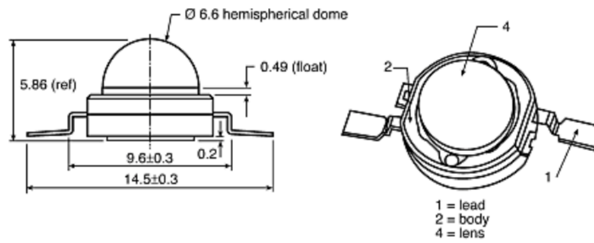


## LumiDrives LED Modules

| Attribute | Value |
|---|---|
| LED Colours | White |
| Mounting Type | Screw Mount |
| Number of LEDs | 1 |
| Forward Voltage | 3.99 V |
| Number of Pins | 2 |
| Viewing Angle | 140 ° |
| Luminous Flux | 45 lm |
| Lens Shape | Round |
| Dimensions | 19.9 x 19 x 7.5mm |
| Colour Temperature | 5500K |
| LED Material | InGaN |

Lambertian Radiation Pattern (without optics)

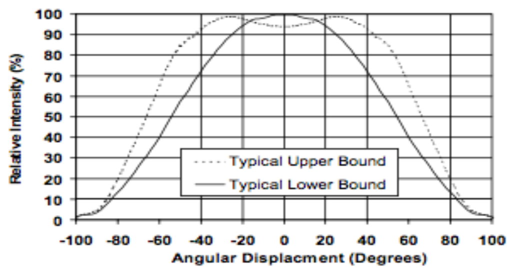


**Figure 7b.**
**Typical Representative Spatial Radiation Pattern for Luxeon Star White Green, Cyan, Blue and Royal Blue.**

## Wavelength Characteristics, $T_J$ = 25°C

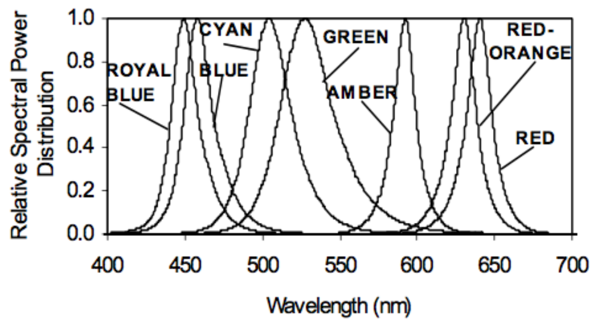


**Figure 1a.**
**Relative Intensity vs. Wavelength.**

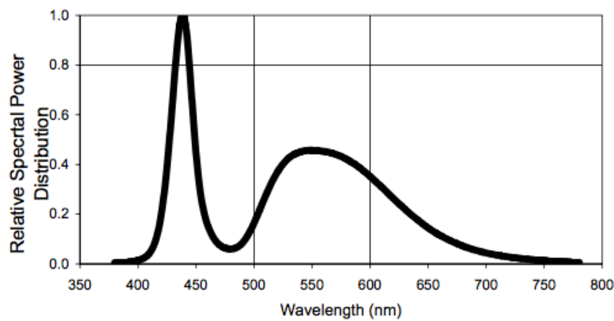


**Figure 1b.**
**White Color Spectrum of Typical 5500K Part, Integrated Measurement.**

Annex 2. Data sheet of cube beam splitter of Fogale microscope

# Broadband Non-Polarizing Beamsplitter Cube, 25.4 mm, 400-700 nm

MODEL: **10BC17MB.1**

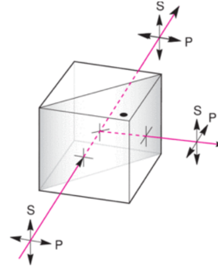


*NOTE: To avoid damage, beam must enter the prism with the dot marked on the side.*

## Description

The 10BC17MB.1 Broadband Non-polarizing Hybrid Cube Beamsplitter has moderate absorption but minimal polarization sensitivity. The broad spectral flatness of this beamsplitter makes it ideal for use with multiple lasers or tunable lasers. Incoming beams are both transmitted and reflected 45%, with the s and p-polarized components matched to within 10% of each other. Hybrid beamsplitters are less sensitive to changes in angle of incidence, resulting in an optic that is chromatically neutral for both convergent and divergent beams. This beamsplitter consists of a pair of precision right-angle prisms carefully cemented together forming a 1 inch (25.4 mm) cube to minimize wavefront distortion. The hypotenuse of one of the prisms is coated with a metal-dielectric hybrid beamsplitter coating optimized over a broad wavelength range. The four faces are antireflection coated with a broadband multilayer dielectric coating to minimize surface reflection losses over the 400-700 nm wavelength range, providing R<0.5% per surface. Due to the metallic nature of the hybrid coating, these beamsplitters are not intended for use with higher power lasers.

## Technical Specs

| Specification | Value |
|---|---|
| **Antireflection Coating** | 400-700 nm |
| **Size** | 25.4 x 25.4 x 25.4 mm |
| **Material** | Grade A N-BK7 |
| **Coating Type** | Multilayer broadband dielectric |
| **Coating Code** | MB.1 |
| **Surface Quality** | 40-20 scratch-dig |
| **Surface Flatness** | ≤λ/4 at 632.8 nm |
| **Durability** | MIL-C-675C |
| **Angle of Incidence** | 0°±5° |
| **Clear Aperture** | >80% of central dimension |
| **Damage Threshold** | 100 W/cm$^2$ CW, 0.1 J/cm$^2$ with 10 nsec pulses, typical |

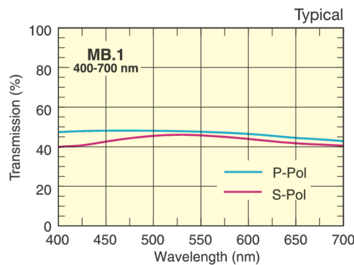


| Specification | Value |
|---|---|
| **Size Tolerance** | ±0.254 mm |
| **Shape** | Cube |
| **Efficiency** | $R_{s,p}$ , $T_{s,p}$= 45 ±5% average, 35% ≤ $R_{s,p}$ , $T_{s,p}$ ≤ 55% |
| **Cleaning** | See How to Clean Optics |
| **Orientation** | To avoid damage, beam should enter prism marked with a dot |
| **Polarization** | S- and P-polarization components matched to within 10%, $\|T_s - T_p\|$ ≤10%, $\|R_s - R_p\|$ ≤10% |
| **Reflected Beam Deviation** | 90° ±5 arc min |
| **Operating Temperature Range** | -50 to 90°C |
| **Transmission** | $T_{s,p}$ = 45 ±5% average, 35% ≤$T_{s,p}$ ≤ 55% |
| **Transmitted Beam Deviation** | ≤5 arc min |

## Annex 3. Specification of immersion objectives from Leica.

| Order No | Objective Name | FWD (mm) | Immersion | Coverglass | Correction Collar | Color Correction VIS | High Transmission VIS |
|---|---|---|---|---|---|---|---|
| 15506224 | HCX PL Fluotar 5x/0.15 | 13.70 | Dry | ♦ | – | ○ | ●● |
| 15506505 | HCX PL Fluotar 10x/0.30 | 11.00 | Dry | ♦ | – | ○ | ●● |
| 15506507 | HCX PL Fluotar 10x/0.30 PH1 | 11.00 | Dry | ♦ | – | ○ | ●● |
| 15506142 | HCX APO L 10x/0.30 W U-V-I | 3.60 | Water | ♦ | – | ● | ●● |
| 15506285 | HCX PL APO 10x/0.40 CS | 2.20 | Dry | 0.17 | – | ●● | ● |
| 15506293 | HCX PL APO 10x/0.40 IMM CS | 0.36 | IMM | ♦ | – | ●● | ● |
| 15506503 | HC PL Fluotar 20x/0.50 | 1.15 | Dry | 0.17 | – | ○ | ●● |
| 15506506 | HC PL Fluotar 20x/0.50 PH2 | 1.15 | Dry | 0.17 | – | ○ | ●● |
| 15506147 | HCX APO L 20x/0.50 W U-V-I | 3.50 | Water | ♦ | – | ● | ●● |
| 15506517 | HC PL APO 20x/0.75 CS2 | 0.62 | Dry | 0.17 | – | ●● | ●● |
| 15506343 | HC PL APO 20x/0.75 IMM CORR CS2 | 0.68 | IMM | ♦ | CORR | ●● | ●● |
| 15506344 | HC PL IRAPO 20x/0.75 W | 0.67 | Water | ♦ | – | ○ | ●● |
| 15507701 | HCX APO L 20x/1.00 W | 2.00 | Water | 0 | – | ● | ●● |
| 15507702 | HCX APO L 20x/0.95 IMM | 1.95 | $n_e$=1.563 | 0 | – | ● | ●● |
| 15506374 | HC FLUOTAR L 25x/0.95 W VISIR | 2.50 | Water | 0 | – | ○ | ●● |
| 15506375 | HC FLUOTAR L 25x/0.95 W 0.17 VISIR | 2.40 | Water | 0.17 | – | ○ | ●● |
| 15507704 | HC IRAPO L 25x/1.0 W motCORR | 2.60 | Water | ♦ | motCORR | – | ●● |
| 15507703 | HC FLUOTAR L 25x/1.0 IMM motCORR VISIR | 6.00 | $n_e$=1.457 | ♦ | motCORR | ○ | ●● |
| 15506295 | HCX PL APO 40x/0.85 CORR CS | 0.21 | Dry | 0.11–0.23 | w | ●● | ○ |
| 15506155 | HCX APO L 40x/0.80 W U-V-I | 3.30 | Water | 0 | – | ○ | ● |

| Order No | Objective Name | Color Correction UV / 405 nm on TCS SP8 | High Transmission UV | Color Correction >800 nm | High Transmission IR | Recommended for FCS | Compatible with | | | |
|---|---|---|---|---|---|---|---|---|---|---|
| | | | | | | | Electro-physiology | Adaptive Focus Control | Water Immersion Micro Dispenser | Phase Contrast |
| 15506224 | HCX PL Fluotar 5x/0.15 | – | ●● | – | ○ | | | | | |
| 15506505 | HCX PL Fluotar 10x/0.30 | – | ●● | – | – | | | yes | | |
| 15506507 | HCX PL Fluotar 10x/0.30 PH1 | – | ●● | – | – | | | yes | | yes |
| 15506142 | HCX APO L 10x/0.30 W U-V-I | – | ●● | ○ | ● | | yes | | | |
| 15506285 | HCX PL APO 10x/0.40 CS | – | ● | – | ○ | | | yes | | |
| 15506293 | HCX PL APO 10x/0.40 IMM CS | – | ○ | – | – | | | | | |
| 15506503 | HC PL Fluotar 20x/0.50 | – | ● | – | – | | | yes | | |
| 15506506 | HC PL Fluotar 20x/0.50 PH2 | – | ● | – | – | | | yes | | yes |
| 15506147 | HCX APO L 20x/0.50 W U-V-I | – | ● | ○ | ● | | yes | | | |
| 15506517 | HC PL APO 20x/0.75 CS2 | ● | ● | – | ○ | | | yes | | |
| 15506343 | HC PL APO 20x/0.75 IMM CORR CS2 | ●● | ● | ○ | ● | | | yes | yes | |
| 15506344 | HC PL IRAPO 20x/0.75 W | – | – | ●● | ●● | | | | | |
| 15507701 | HCX APO L 20x/1.00 W | – | ● | – | ● | | yes | | | |
| 15507702 | HCX APO L 20x/0.95 IMM | – | ● | – | ● | | | | | |
| 15506374 | HC FLUOTAR L 25x/0.95 W VISIR | – | ● | ● | ●● | | yes | | | |
| 15506375 | HC FLUOTAR L 25x/0.95 W 0.17 VISIR | – | ● | ● | ●● | | | yes | yes | |
| 15507704 | HC IRAPO L 25x/1.0 W motCORR | – | – | ●● | ●● | | yes | | | |
| 15507703 | HC FLUOTAR L 25x/1.0 IMM motCORR VISIR | – | – | ● | ●● | | | | | |
| 15506295 | HCX PL APO 40x/0.85 CORR CS | – | ○ | – | – | | | yes | | |
| 15506155 | HCX APO L 40x/0.80 W U-V-I | – | ○ | ○ | ○ | | yes | | | |

♦ For use with and without coverglass
– Not available

●● Superior performance, highly recommended
● Excellent performance
○ Good performance

* STED WHITE objective especially designed for use with STED and STED 3X. Axial color shift of objective <100 nm in VIS

Annex 4. Design of the adapted tube for objective in reference arm.

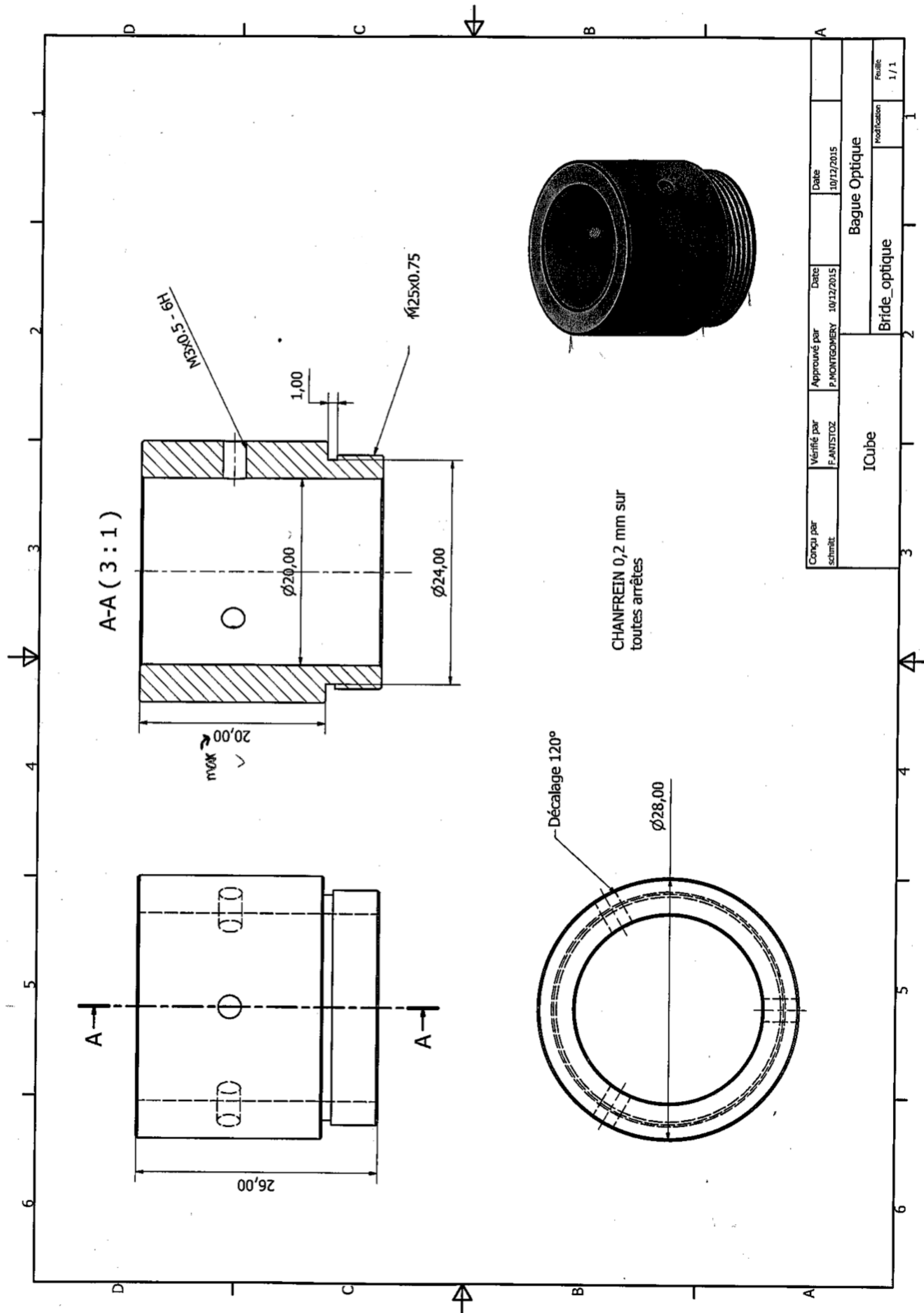

Annex 5. Data sheet of white light LED (lime LED color)

**Lime (567nm) LUXEON Rebel ES LED on a SinkPAD-II 20mm Star Base - 313 lm @ 700mA**

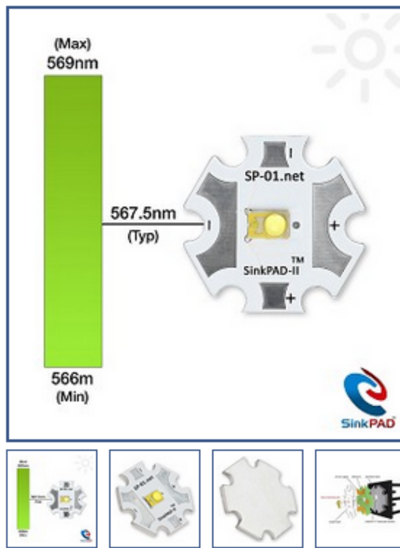


The SP-01-L1 LED assembly features a single LXML-PX02-0000 Lime LUXEON Rebel ES LED soldered to a **SinkPAD-II**™ 20mm Star base.

The SinkPAD-II™ uses second generation technology to minimize thermal resistance by eliminating the dielectric layer so that the LED thermal pad is soldered directly to the aluminium base. This ensures the lowest possible LED junction temperature, resulting in increased LED life, lumens output and overall reliability.

## SPECIFICATIONS

| | |
|---|---|
| LED Color | **Lime** |
| Lumens @ 350mA (1) | **167 lm** |
| Lumens @ 700mA (1) | **313 lm** |
| Efficacy @ 350mA (1) | **174 lm/W** |
| Efficacy @ 700mA (1) | **160 lm/W** |
| Typical Wavelength (2) | **567 nm** |
| Wavelength Range (2) | **566 to 569 nm** |
| Beam Angle (3) | **125°** |
| Recommended Operating Current (4) | **700 mA** |
| Maximum Rated Drive Current | **1000 mA** |
| Typical Forward Voltage (5) | **2.75 Vf** |
| Maximum Forward Voltage (5,7) | **3 Vf** |
| Thermal Resistance (2,6) | **6.7 C°/W** |
| Max Recommended Junction Temp | **150 °C** |
| Operating Temperature Range | **-40 to 135 °C** |
| Dimensions L x W x H | **20 x 20 x 3.7 mm** |

1. Values for LEDs from flux bin G.
2. Values based on 350mA and a Thermal Pad temperature of 25 °C.
3. Viewing angle is the off axis angle from lamp centerline where the luminous intensity is ½ of the peak value.
4. This is the maximum operating current that we recommend for this LED. Higher drive currents may be possible, but will require careful design of a suitable cooling system.

Annex 6. The procedure of Abbe-refractometer

**1 Optical System:**

This optical system of the instrument is composed of the two parts: a telescope system and a projection reading system (Fig 4).

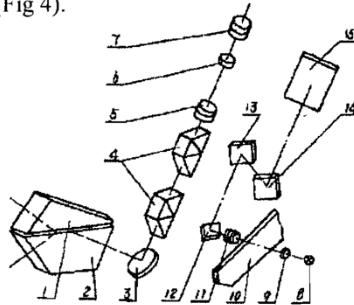

Fig. 4

(1) Light-entry prism; (2) Refracting prisms; (3) Swing reflecting mirror; (4) Achromatic dispersion prism group; (5) Objective; (6) Field lens; (7) Eyepiece; **(8) High intensity LED lamp** (9) Condenser; (10) Glass scale plate; (11) Projection objective group; (12) Reflecting mirror ①; (13) Reflecting mirror ②; (14) Reflecting mirror ③; (15) Projection screen

Procedures:

Place the measured sample on prism holder.

Adjusting the focus, see from bottom ocular.

Adjusting the line in the midle of cross.

See the refractive index (nD)

Measuring the dispersion value:

The basic operation method is just as same as that in measuring the refractive index. However, when rotating the handle (17), the dark-and-light borderline in the field of eyepiece should be adjusted to the position of colorless; at this moment the scale indicating value Z should be recorded from the dispersion scale circle (16) and then taken down the refractive index $n_d$. According to the refractive index $n_d$, find out values A and B from the same line in the dispersion table. If the refractive index $n_d$ to be 1.353, the values A and B can be obtained by the difference between the refractive indices 1.350 and 1.360 by using interpolation.

Again according to value Z, the corresponding value $\sigma$ can be found out in the dispersion table of instrument. If value Z has some decimals, value $\sigma$ can be obtained by its difference through interpolation. When value Z is more than 30, value $\sigma$ is obtained as the negative, when value Z is smaller than 30, the value $\sigma$ is obtained as the positive. With the help of the following formula, the average dispersion can be obtained according to values A, B and $\sigma$.

$$n_F - n_C = A + B\ \sigma$$

Annex 7. Data sheet of motorized MFA-PP

## Design Details

| | |
|---|---|
| Base Material | Stainless Steel |
| Bearings | Double row linear ball bearings |
| Drive Mechanism | Backlash compensated leadscrew |
| Drive Screw Pitch | 0.5 mm |
| Reduction Gear | MFA-CC: 1:14<br>MFA-PP: 1:43 |
| Feedback | MFA-CC: Motor mounted rotary encoder; 2,048 cts/rev<br>MFA-PP: None |
| Limit Switches | Optical switches |
| Origin | Uses motor side limit for homing, typically <5 mm repeatability |
| Cable Length | MFA-PP, MFA-PPD & MFA-CC: 3 m<br>MFA-CCV6: 1.5 m |

| | MFA-PP and MFA-PPD | MFA-CC |
|---|---|---|
| Travel Range [in. (mm)] | 1 (25) | |
| Minimum Incremental Motion (μm) | 0.1 | 0.1 |
| Uni-directional Repeatability, Typical (Guaranteed) (μm) | 0.12 (±0.25) | ±0.08 (±0.15) |
| Bi-directional Repeatability, Typical (Guaranteed) [(1)] [(2)] (μm) | ±0.2 (±0.75) | ±0.15 (±0.75) |
| Accuracy, Typical (Guaranteed) [(1)] (μm) | ±0.9 (±3.0) | ±0.7 (±3.0) |
| Maximum Speed (mm/s) | 0.3 (MFA-PP)<br>1.0 (MFA-PPD) | 2.5 |
| Pitch, Typical (Guaranteed) [(1)] (μrad) [(3)] | ±25 (±100) | |
| Yaw, Typical (Guaranteed) [(1)] (μrad) [(3)] | ±30 (±50) | |
| MTBF | 10,000 h at a 1 kg load with a 20% duty cycle | |

1) *Shown are peak to peak, guaranteed specifications or ±half the value as sometimes shown. For the definition of typical specifications which are about 2X better than the guaranteed values, visit www.newport.com for the Motion Control Metrology Primer.*

2) *After backlash compensation.*

3) *To obtain arcsec units, divide μrad value by 4.8.*

## Load Characteristics and Stiffness

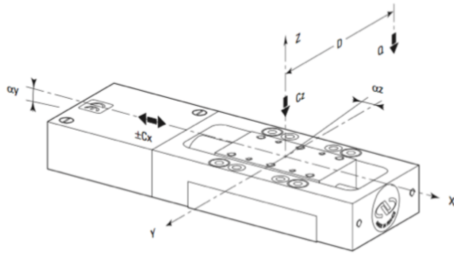


| | |
|---|---|
| Cz, Normal centered load capacity (N) | 50 |
| -Cx, +Cx, Axial load capacity (N) | 10 |
| Kαx, Compliance in roll (µrad/Nm) | 60 |
| Kαy, Compliance in pitch (µrad/Nm) | 10 |
| Q, Off-center load (N)<br>Where D = Cantilever distance (mm) | Q ≤Cz ÷ (1 + D/20) |

### Stepper Drive Version

Stepper-motor-driven stages are offered in one half-step drive version: MFA-PP & MFA-PPD.

### Micro-Step Drive

This is the drive for stepper or pulse-driven motors, transmitted by the electronic unit, which entails a theoretical movement of the motor by one fraction of a full-step. For these translation stages, the micro-step is equivalent to 1/64 of the full-step.

### Stepper Motor Performance Specifications

| | Resolution [1] (µm) | Speed (mm/s) | Motor |
|---|---|---|---|
| MFA-PP | 0.00757 | 0.3 | UE16PP |
| MFA-PPD | | 1 | |

[1] *Micro-step driving.*

Université de Strasbourg

# Husneni MUKHTAR

## Development of compensated immersion 3D optical profiler based on interferometry

msii ÉCOLE DOCTORALE

Résumé en française

La CSI (Coherence Scanning Interferometry) ou la WLSI (White Light Scanning Interferometry) est une technique d'imagerie optique bien établie pour mesurer la rugosité de surface et la forme des surfaces microscopiques [1]. Les avantages sont la sensibilité axiale nanométrique, un large champ de vision (des centaines de µm à plusieurs mm) et la vitesse de mesure (quelques secondes à quelques minutes).

La technique est basée sur l'interférométrie optique avec une configuration de Linnik très difficile à ajuster mais elle présente plusieurs avantages: des objectifs d'ouverture numérique plus élevés pour améliorer la résolution spatiale; longue distance de travail, car il n'y a aucun besoin de l'un des composants devant l'objectif; une configuration de mode de lumière polarisée; franges contrastées en raison de la possibilité de modifier les voies optiques et les intensités des deux bras indépendamment. Alors que l'utilisation d'un objectif d'immersion dans l'eau présente les avantages suivants: éviter les problèmes liés à l'ajustement entre la formation des franges et le plan de formation de l'image; et pour minimiser la différence de dispersion entre les bras de l'interféromètre.

Afin de pouvoir mesurer en mode eau et d'obtenir des échantillons à haute résolution latérale de types chimiques et biologiques, plusieurs défis doivent être surmontés tels que l'équilibrage de l'OPD sur les deux bras; trouver et ajuster les bonnes franges de contraste; trouver et adapter une compensation adéquate de l'eau dans le bras de référence horizontal pour faire fonctionner un système dans l'eau.

Mot-clés: CSI, WLSI, Linnik, interférométrie, immersion compensée, polymère élastique, SPA, PDMS.

Résumé en anglais

Coherence Scanning Interferometry (CSI) or White Light Scanning Interferometry (WLSI) is a well-established optical imaging technique for measuring the surface roughness and the shape of microscopic surfaces. The advantages are the nanometric axial sensitivity, a wide field of view (hundreds of µm to several mm) and the measurement speed (a few seconds to a few minutes).

The technique is based on optical interferometry with a Linnik configuration which very difficult to adjust but it offers several advantages: higher numerical aperture objectives to improve spatial resolution; long working distance, because there is no need for any of the components in front of the lens; a polarized light mode configuration; contrasting fringes because of the possibility of modifying the optical pathways and the intensities of the two arms independently. While the use of a water-immersion objective gives the following advantages: to avoid the problems related to the adjustment between the formation of the fringes and the plane of formation of the image; and to minimize the difference in dispersion between the arms of the interferometer.

In order to be able to measure in water mode and to obtain high lateral resolution samples of chemical and biological types, several challenges must be overcome such as balancing the OPD on both arms; finding and adjusting the good contrast fringes; finding and adapting a suitable water compensation of water in horizontal reference arm to operate a system in water.

Keywords: CSI, WLSI, Linnik, interferometry, compensated immersion, elastic polymer, SPA, PDMS.